CRABI

Crud **R**emoval **A**utonomous **B**rushing **I**nstrument

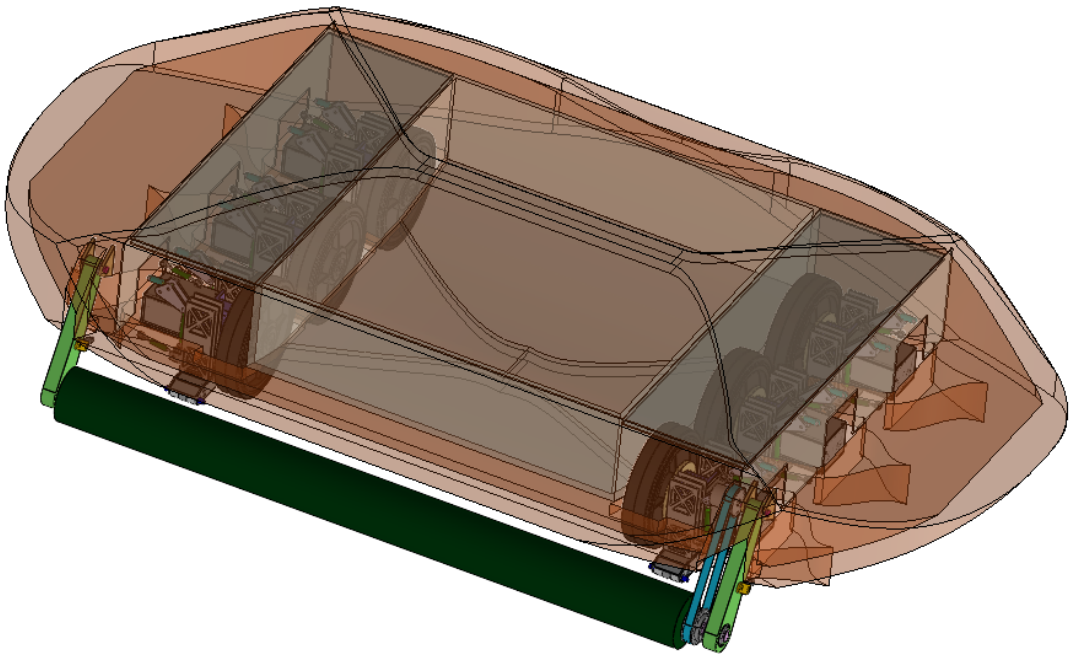

Course Instructors:
Douglas Hart, Alfonso (AJ) Perez, Maaya Prasad

Communication Instructors:
Juergen Schoenstein, Michael Trice

2.013/2.733 Fall 2022 Team:
Levi Gershon, Juliana Green, Diane Li, Pierre Lonni
2.014/2.734 Spring 2023 Team:
Levi Gershon, Pierre Lonni, Gazi Sakib, Andrew Lin, Sophie Longawa, Trinity Stallins, Keeghan Patrick, Henry Sobieszczyk

Table of Contents

1. Project Overview

1.1 Executive Summary

Biofouling - organic crud that grows on most objects immersed in water - accumulates on ships at sea, increasing drag, and thus fuel costs. Currently, biofouling costs the US shipping industry alone $36 billion dollars per year in excess fuel consumption [1]. Moreover, fuel burned by container ships accounts for 3% of global CO2 emissions, and so biofouling reduction has the potential to reduce global emissions by ~0.3% [2]. This project is focused on designing a mechanical system to remove biofouling from Panamax-sized container ships on a bi-weekly basis to boost fuel efficiency.

During the 2022-2023 academic year, the team developed an autonomous system to clean ships while in transit. The system - a magnetically-attached crawler - uses tires for ease of motion as well as drag resistance, and a cylindrical rotating brush to clean. The entire system is battery operated and encased in a hydrodynamic shell intended to minimize drag regardless of the incoming water direction. The system cleans transverse sections of the hull, moving down the side of the ship, across the bottom of the hull, and back up the opposing side before popping above the waterline, turning around, and cleaning the adjacent section in a similar manner. The crawler navigation is to be autonomous with absolute location sent via radio triangulation each time it surfaces for re-calibration.

The focus of the program thus far was on sub-system level designs and fabrications in order to de-risk the critical system risks, namely the abilities to clean and attach to the hull. This was done through analysis and testing at a sub-system level, focusing specifically on the systems for cleaning, attachment, propulsion, and the hydrodynamic shell covering the crawler. Cleaning tests were performed on biofouled samples to determine cleaning pattern and brush design, and motor enclosures were submerged in water to test their seals. Magnetic Halbach arrays were tested to measure adhesion pressure, tire testing was conducted to verify the frictional coefficient necessary for drag resistance, and multiple hydropackage designs were tested to evaluate their viability. Detailed design work was conducted on the cleaning, attachment & propulsion, and chassis subsystems, and prototypes of each system were fabricated from thousands of individual components. Limitations of the current design include minimal work on the navigation, sensing and power systems. Additionally, no suitable design of the hydropackage has been selected, as none of the models tested met the functional requirements of the crawler. In terms of operational constraints, the crawler is not able to traverse or otherwise navigate bilge keels, and as a result, ships with these features should be avoided altogether. The crawler is additionally not able to clean over sacrificial anodes, and should not be used to clean the propeller or bulbous bow, however the bulk length of ships with these features may be cleaned according to the driving plan described above.

1.2 Introduction

The issue of biofouling arises naturally when bacteria and other organisms in the ocean gradually adhere to surfaces submerged for extended periods of time. Biofouling builds up on bridge posts, docks, and buoys among other immersed objects [5]. Biofouling accumulation on ships is of particular interest because the additional drag can significantly increase fuel usage. While biofouling buildup occurs at different rates depending on environmental conditions and surface parameters [6,7], engineers have yet to design a perfect coating that prevents biofouling adhesion entirely. Currently, biofouling costs the US shipping industry alone $36 million dollars per year in fuel losses [1]. Fuel burned by cargo vessels accounts for 3% of global CO2 emissions, and so biofouling reduction has the potential to reduce global emissions by ~0.3% [2].

Existing solutions are primarily targeted at in-port cleaning, such as dry-docking or hiring a team of divers. While drydocking allows for all required maintenance on the ship to be done at once, it is costly both in terms of money and idle time. In-port cleaning, meanwhile, must additionally be able to handle large amounts of biofouling accumulated during transit, often over the course of multiple trips. In-port cleaning services must abide by varying degrees of restrictions on in-water cleaning, debris collection, and debris treatment. Alternatively, biofouling may be removed in transit. These solutions require the ship to stop for long periods in the middle of the ocean or sustain cleaning at ship velocities upwards of 10 m/s [3]. There are a few in-transit solutions currently under development, some of which are already commercially available. One example is Shipshave which provides semi-autonomous in-transit cleaning [4]. This project is focused on designing a mechanical system to remove biofouling from Panamax-sized container ships on a bi-weekly basis while in-transit to boost fuel efficiency.

1.3 Biofouling-Induced Drag

1.3.1 Types of Biofouling

Biofouling begins with soft fouling – slime, then grass. This provides a basis for hard fouling – tubeworms and barnacles. In more advanced stages, known as composite fouling, bivalves, corals, anemones, and other organisms may also take hold and grow. The Naval Ships' Technical Manual (NSTM) ranks fouling patterns on a fouling rating (FR) scale of 0-100 in order of increasing organism variety and severity. Growth patterns can be further described by percentage of coverage [8].

1.3.2 Determining Soft Biofouling Cleaning Frequency

NSTM notes that the final stage of soft fouling (FR-30) can "not be easily wiped off by hand" [8]. As summarized in **Figure 1**, the adhesion strength of hard fouling, given as shear force over area of attachment, is around 4 orders of magnitude greater than that of soft fouling.

Notably, the adhesion force of hard fouling rivals the adhesion force of paint to the hull of the ship [9]. This leads to the system-level design decision to ***clean off soft biofouling before hard fouling attaches***.

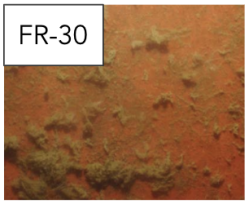

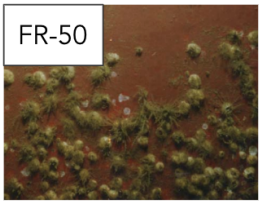

	Soft Fouling Adhesion Strength (kPa)	Hard Fouling Adhesion Strength (kPa)
Silicone Substrate	0.050 - 0.275	100 - 500
Epoxy Substrate	~ 1.65 (estimated)	500 - 2250

Figure 1. Comparison of soft and hard biofouling adhesion strengths [9]

The growth rate of biofouling dictates the frequency of cleaning. For soft fouling, bacteria attach within a half hour of wetting and slime can be felt by hand within an hour [8]. Hard fouling rates are highly dependent on environmental conditions. In general, fouling rate increases with increasing idle time, higher temperature, and higher salinity. Additional factors such as paint condition, local currents, nutrients, and biodiversity will also impact fouling rate [6,7].

Anecdotally, small barnacles begin to grow on leisure boats in as little as a week of idle time in Florida during the summer [10,11]. A Swedish company for hull cleaning products (also for leisure boats) estimates 2-4 weeks for barnacles to harden beyond brush removal [12]. The hull crawler is proposed to follow a cleaning frequency of ***once every two weeks.*** For a solution that does not require a full two weeks to traverse the hull, the system would only be deployed once every two weeks and would have periods of inactivity between cleaning cycles.

1.3.3 Existing Biofouling Mitigations

Currently, the industry standard for addressing biofouling is to coat ships with anti-fouling paints. Even so, biofouling accumulates on top of anti-fouling paint. In-water hull cleaning is typically performed by divers every 4-5 months while ships are stopped in port [13]. Additionally, Panamax-size container ships are power washed in dry dock twice every five years [14]. Because of the huge potential cost savings, a number of other autonomous or semi-autonomous devices have been developed to remove biofouling. The HullWiper is an autonomous vehicle designed to cling to the hull of a ship and clean it using pressurized seawater. The primary selling point of the HullWiper is its novel cleaning system, and the vehicle

can only be deployed while a ship is stationary in port. Similarly, the HullSkater from Jotun is another crawler that can be deployed as needed to clean the hull. HullSkater is intended to be carried on board the ship at all times, but it still requires the ship drop anchor before it can be deployed. Finally, Shipshave offers a semi-autonomous system for the in transit cleaning of hulls. The ITCH system involves a robot attached by winch to the deck of the ship, and is capable of cleaning while the parent ship is in motion [4]. However, the system has only been tested at speeds of 9-18 knots, meaning that large containerships would have to reduce speed during operation. Each of these products may allow for more flexible cleaning, but will still cause delays that will cost shipping companies time and money. By designing for frequent cleaning of ships at full speed, the value proposition of CRABI is to reduce money and time spent on removing biofouling and to reduce the average fouling quantity, saving fuel.

1.4 Concept of Operation

1.4.1 Strategy

CRABI is designed to operate as a mobile, crew-operated solution to biofouling in commercial shipping that can be deployed regularly to remove soft biofouling during transit without requiring the ship to reduce speed. Other cleaning methods involving external cleaning stations or modifications to the ship's hull were rejected due to the potential time and cost associated with setup and installation. Instead, the crawler would be carried on board the ship along with a team of operators and deployed every two weeks to scrub the hull before soft fouling has the opportunity to harden. Cleaning will be accomplished by a rotating brush fitted to the front of the crawler and pressed into the hull to scrub it clean as the craft makes its traversal. CRABI is intended for use on ships traveling at speed up to 20 knots, so the system must be able to resist significant drag forces during use. To maintain contact with the hull and resist drag, a magnetic attachment system has been designed to provide a constant downforce during operation. Additionally, the crawler will be covered in a hydrodynamic shell to reduce drag as much as possible. No suitable method has been found for communicating with the craft while it is underwater, so radio beacons will be placed around the deck of the ship and used to locate CRABI whenever it breaks the surface of the water. An onboard battery system will provide power to the brush and to six wheel assemblies that will provide propulsion across the hull. In order to reduce both the complexity of the design and the potential of damaging the parent ship, the crawler’s operation will be restricted to the areas of the hull without obstacles like bilge keels and away from vulnerable and valuable components like the propeller. These restrictions would still allow the device to clean the majority of the hull and provide significant cost savings to the customer.

1.4.2 Driving Path

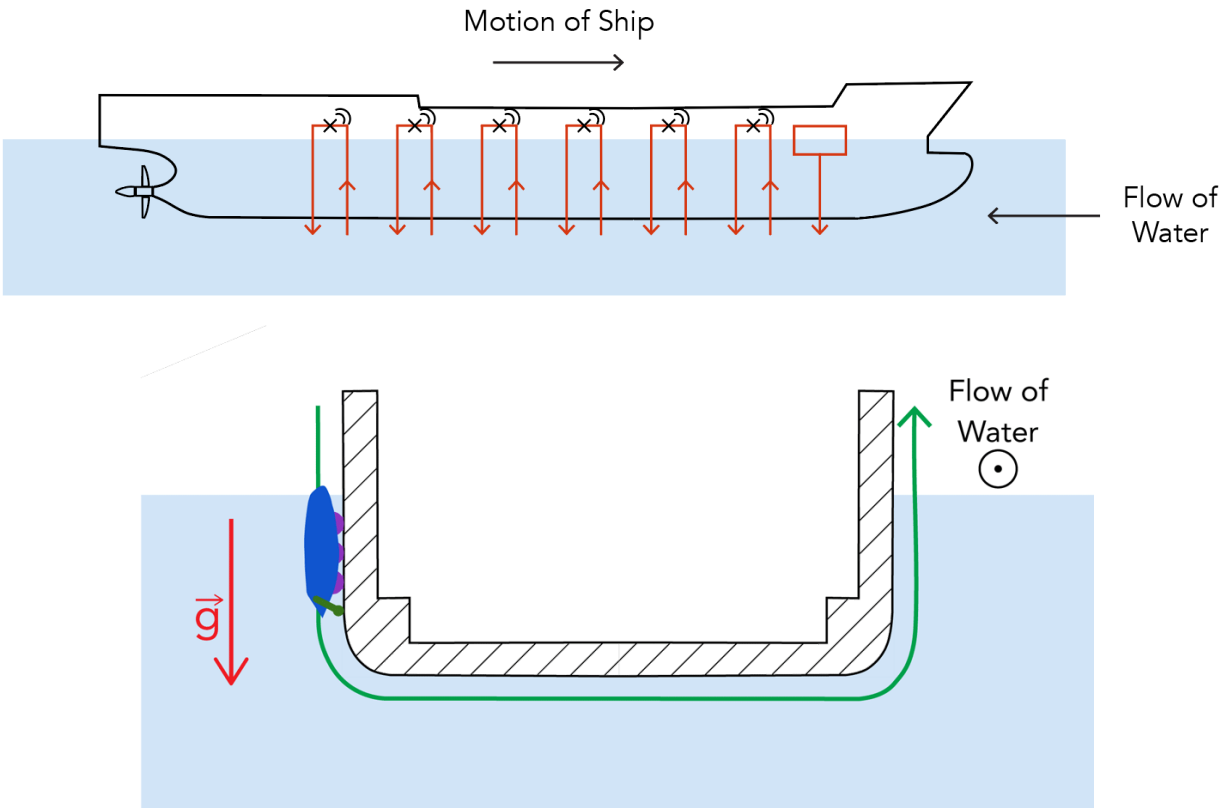

Figure 2. Proposed driving path for the hull crawler, orthogonal views. **(top)** Crawler path along the length of the hull. **(bottom)** Crawler path along a single transverse section of the hull.

The proposed driving path of the crawler is to sweep back and forth under the hull, turning above the water line, as schematized in **Figure 2**. Turning above the water line both avoids the need to drive against the flow of water and allows for frequent absolute location mapping and communication with the deck after each underwater pass. This driving path is limited to ships without bilge keels.

1.5 System Design Requirements

The aim of this project was to determine and then validate a minimum viable product for a hull cleaning crawler. Accordingly, the requirements developed reflect not every edge case, but rather an approximate breadth of the more common ones. Foremost, the crawler must be able to clean fouling from the hull at the frequency specified above (biweekly). It must be able to do so while operating in a seawater environment at high water velocity and navigating irregularities in hull topography. The fouling removal must be sufficient so as to successfully decrease the

average total drag on the parent vessel, and it must abide by regulatory requirements. **Table 1** contains quantitative estimates of all these requirements, as well as an order of magnitude estimate of the cost saved by the crawler each month, and thus the upper bound for its monthly cost. The following sections will discuss operating conditions in further detail (**Section 1.5.1**), provide a preliminary cost evaluation (**Section 1.5.2**), and an overview of cleaning regulations (**Section 1.5.3**).

Table 1. Summary of global system design requirements.

System Requirement	Evaluation (est)	Sources
Operational Environment *Saltwater*	Hydrostatic Pressure: 1 - 2.6 atm Temperature: 4° - 30°C	[15–19]
Customer Vessel Speed *Taken for container ships*	Slow-steaming: 18-20 knots Max speed: 24 knots	[3]
Customer Vessel Hull Topography *Surfaces to be navigated by cleaner*	Sea Chest: 3m x 3m Min Radius of Bow: 1.3m	[20,21]
Max Operational Cost *Equal to saved fuel costs*	$46,000 / month	[22–24]
Cleaning Rate *To achieve average 5% fuel economy increase*	Full hull every 2 weeks	[9,12,25]
0.1% Total Drag Increase Limit *Cleaning device must not increase net drag in transit*	CDA = 0.09 m²	[26–28]
Regulatory Compliance *Debris collection in harbor*	No debris collection needed in international waters	[29–34]

1.5.1 Operating Conditions

The hull crawler needs to be adapted to oceanic conditions that include salinity, temperature, and pressure. With seawater, corrosion is a large concern. Materials should be selected with care to avoid serious structural damage, from various mechanisms such as galvanic corrosion or stress-corrosion cracking. On major trade routes, surface water temperatures are expected to range from 4°C to 30°C [15,16,19]. Design performance, from battery efficiency to material stiffness, should keep this temperature variation in mind. Additionally, the hydrostatic pressure is expected to vary from 1 barr to 2.6 barr for the designed operating depths of 0m

(surface) to 16.5m (ship's bottom) [17]. This pressure variation will influence aspects of the design such as the hydrodynamics and waterproofing.

Furthermore, CRABI's aim is to clean the ship's hull during transit. This results in two main operating conditions that will drive design: the ship speed or waterflow speed and topography of the surface that needs to be cleaned. For container ships, travel speed varies from 18 to 20 knots during slow-steaming and can reach up to 24 knots at max speed [3]. The crawler must withstand the drag forces of these travel speeds to remain attached to the parent vessel in transit. Regarding hull topography, shown in **Figure 3**, container ship hulls have an estimated radius of curvature as low as 1.3m and surface protrusions such as sea chest grates and sacrificial anodes [20,21]. The hull crawler should be designed to either drive over these variations in hull topography or navigate around them. Note: the current crawler design does not accommodate ships with bilge keels.

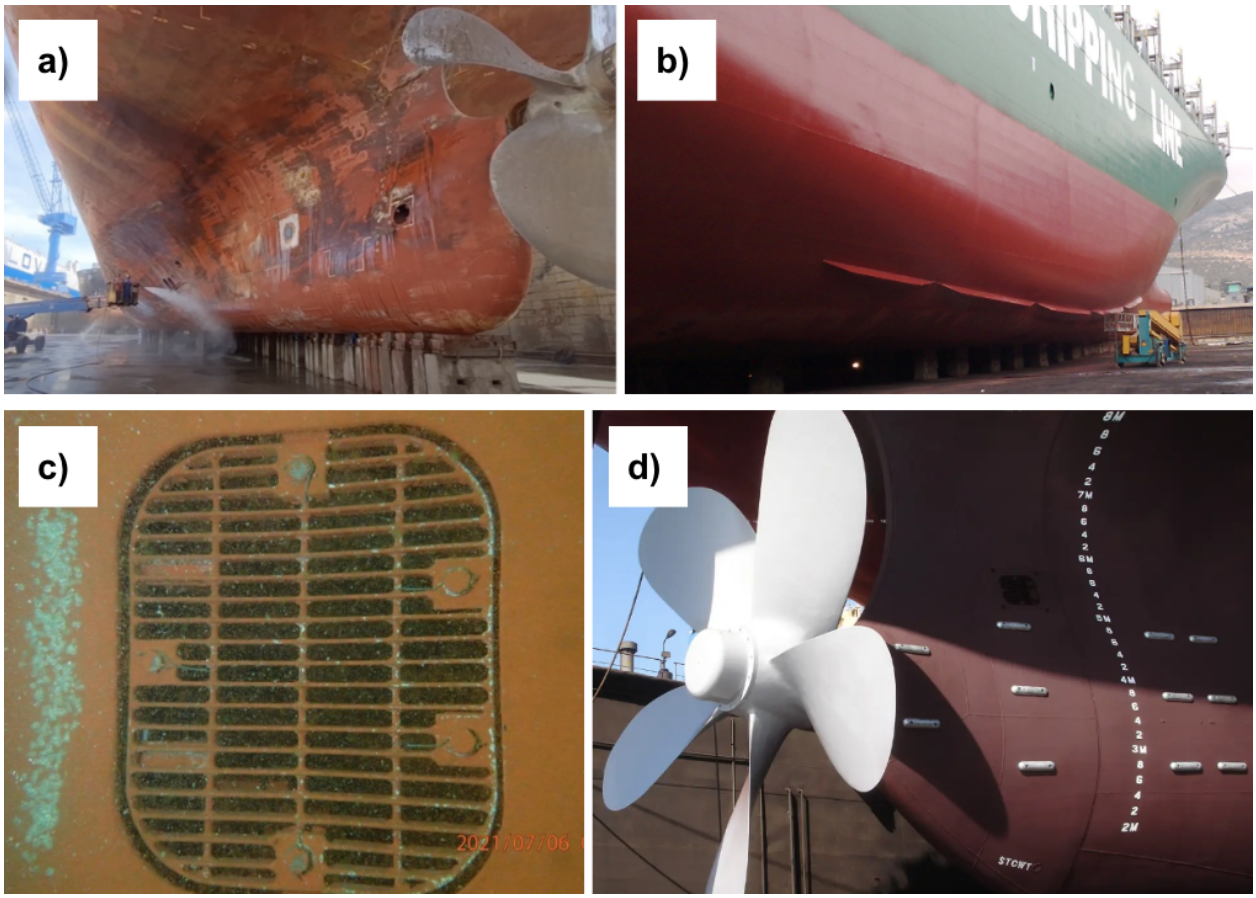

Figure 3. Variations in hull topography: a) hull without bilge keel; b) hull with bilge keel; c) sea chest grate; d) sacrificial anodes.

1.5.2 Design Constraints

Major design constraints are the maximum cost, cleaning rate, and allowable increase in the ship's drag.

In order to be cost-effective, the lifetime cost of the crawler should be less than the additional fuel costs of drag due to biofouling. From **Figure 4**, it is determined that a Panamax vessel (4,500 TEUs) will have a fuel consumption of approximately 75 tons per day [3]. With a fuel cost of $600/ton and 66.3% container ship utilization rate, monthly fuel cost for a container ship is $925,000 [22,24]. Estimating that biofouling accounts for 5% of this consumption, a biofouling-related fuel cost of **$46,000** per month, per ship is obtained [25]. This places an upper bound on the system cost to maintain its value proposition of less than $46,000 per month, averaged over the lifetime of the system.

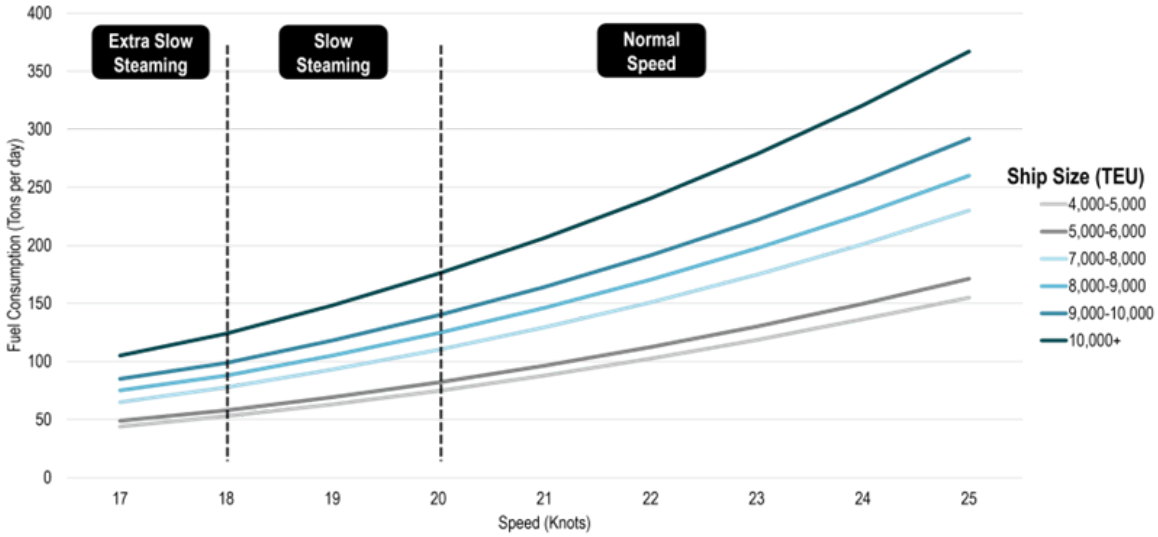

Figure 4. Fuel consumption by container ship size, measured in number of twenty-foot equivalent units cargo capacity, and speed [3].

As described in **Section 1.3.2**, in order to clean soft fouling before hard fouling attaches, the full hull should be cleaned once every 2 weeks. Finally, in order to realize the fuel savings from hull cleaning, the added drag of the hull crawler should be less than the added drag of biofouling. A limit of 0.1% total drag increase is set, which translates to an average coefficient of drag times frontal area (CDA) of 0.09 m².

1.5.3 Regulatory Compliance

Regulations for ship cleaning and cleanliness vary significantly by location. Beyond 24 miles from the shoreline, international waters are under the purview of the International Maritime Organization (IMO). Regulations here often follow more lenient codes of conduct including best practices recommendations for cleaning schedules and preventative anti-fouling solutions, with no requirement for debris collection or treatment. In ports and near to shore,

regulations are set by national governments and range from more general recommendations to specific limits on the size of debris particles, such as in the case of New Zealand and Australia [31,32].

Considering the regulatory landscape described above and the wide variation in national requirements, the team decided to proceed with cleaning in international waters which allows for the de-scoping of any debris collection or treatment systems. In-transit cleaning also fulfills a cleaning need that is unmet by in-port solutions, namely divers and dry docking. The decision to perform in-transit cleaning also informs other design requirements (e.g. water speed, temperature, non-manual operation, and minimum of 24 miles offshore).

Table 2. Snapshot of regulatory requirements for cleaning and debris collection [29–34]

	International	**US**	**Most stringent nations (NZ, AU)**
Cleaning requirements	Suggest regular cleanings	Require regular cleanings and best practices documentation	Require clean hull upon entry
In-water cleaning	Encouraged to minimize fouling build-up	Prohibited for hulls with toxic coatings	Prohibited
Debris collection	None required	Coating chemicals may not be detectable in cleaning plume	Recommended for particles over 50µm diameter

1.6 Design Overview

Based on the mission plan selected in **Section 1.4**, the architecture drives major design choices in the subsystems of the crawler, some of which are highlighted below.

The **cleaning subsystem (Section 2),** while accomplishable via many technologies, from heating to UV radiation or water jet cleaning, has been refined into a mechanical cleaning arrangement with cylindrical brushes as the most energy efficient solution, and then a brush and semi-kinematic suspension system designed.

For the **attachment and propulsion subsystem (Section 3)**, the design is driven by the requirement to create downforce to stick to the ship and friction to avoid slippage under the drag force of the water flow. This downforce will in part be achieved by the hydropackage that will manage the flow in order to make the crawler stick to the ship's surface. The remainder of the

needed downforce will be obtained by using Halbach arrays, an arrangement of permanent magnets that will provide magnetic adhesion force towards the steel hull of the ship. Finally, this subsystem will use tires to react against the drag force of water and drive the crawler forward, and a novel suspension architecture to conform to the hull.

The **chassis (Section 4)** constitutes an aluminum frame to hold the disparate system components together and provide mounting points for the needed subsystems and components. It is created via a tab-and-slot sheet methodology, enabling tight system level tolerances from the precision of laser cut sheet metal while also minimizing cost. Minimal welding is used currently for timeline reasons, but long term costs will be reduced by replacing bolts with welds and rivets.

The **hydropackage subsystem (Section 5)** will be a symmetric shape solution, as asymmetry would result in the need of two brushes to always keep the same orientation in a round trip. The main task for this subsystem is to shape the shell in order to maximize downforce and minimize the drag coefficient. An initial biomimetic design, akin to a crab shell which is able to produce downforce from flow in all directions, was pursued. Unfortunately, both that concept and two subsequent revisions tested in this program failed to meet their functional requirements; learnings from that process, however, have suggested a path forward with mechanically configured hydrofoils. While not yet designed, testing done thus far will shape the design of the new system, and the core shell design will follow directly from this program's work.

Finally, the **electronics subsystem (Section 6)** controls and powers the prototype crawler, using a wall-mounted tethered power supply for testing, seven off the shelf DC inverters, and a hobby grade radio receiver/transmitter pair for control. Some circuitry had to be included for analog/digital conversions, and is discussed in that section. Digital vehicle control and telemetry were de-scoped in favor of analog simplicity, as these fall within the remit of previously developed and well-understood robotic technologies.

1.6.1 Overall Sizing

The overall size of CRABI was guided by the following tradeoffs:

- **Minimization of drag**: As the side area directly impacts the crawler drag from the parent vessel's motion, reducing the overall size directly reduces the drag.
- **Battery size and weight**: If the crawler is larger, the power needed to operate it is higher, the torque needed to climb the size of the ship is higher, and the battery therefore itself needs to be larger and heavier.
- **Needed ground clearance**: If the crawler has a longer wheelbase, the ground clearance it needs to go over curves will increase. As it is desirable to minimize the ground clearance for optimum ground effect force, a shorter wheelbase is desirable.

- **Minimizing the cleaning duration**: Increasing the brush width directly increases the area cleaned per transverse path under the ship, and thus directly reduces the cycle time of a complete cleaning.

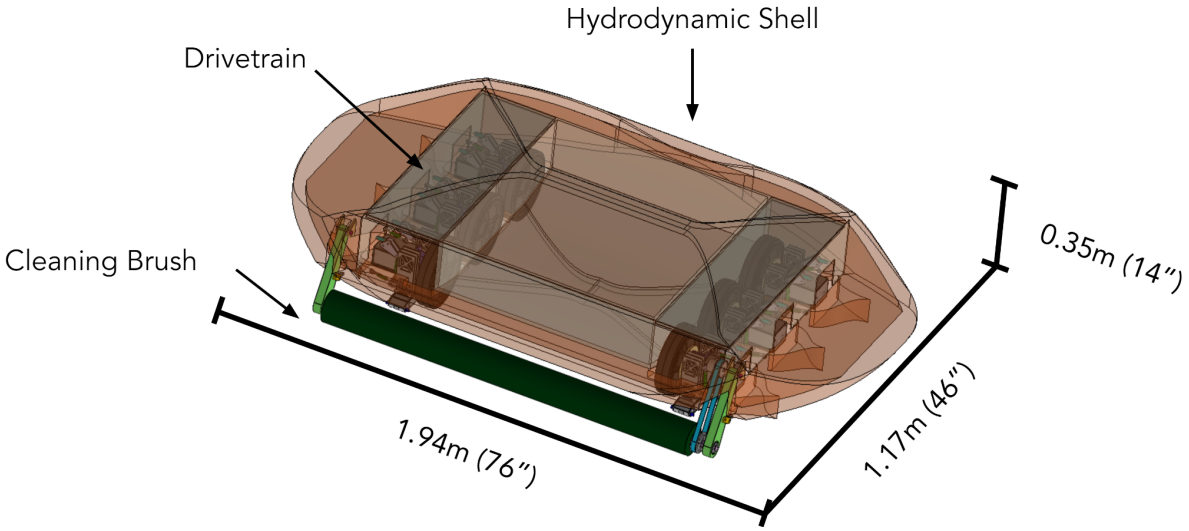

Figure 5. Isometric view of the crawler, with external dimensions labeled. Note the significant extent of the hydropackage beyond the inner volume of the subsystems enclosed.

Taken together, these considerations drive an aspect ratio that is wider than it is long, as seen in **Figure 5**. The limiting factor on length was the need to have a 3x2 wheelbase, as the crawler might lose pitch control driving over a bump (since the downforce originates near each wheel, with the magnetic ski) with only a 2x2 wheel configuration. Targeting a single shift for cleaning, to minimize disruption to ship operations, a speed of 0.8 m/s with a cleaning width of 40" (1m) was chosen. In turn, the wheelbase length must be 20" (0.51m) to permit driving around the curvature of the hull with 8" (20cm) diameter wheels. This then requires 2" (5cm) of ground clearance due to the curvature of the hull. Note that the overall dimensions, indicated in **Figure 5**, are rather much larger than these values due to the hydropackage shell.

1.6.2 Core Subsystems

Six sprung wheel assemblies are used for the powertrain, made identical to save engineering time, and each capable of the full suspension travel. The cleaning mechanism is mounted to the front of the crawler, with independently sprung left and ride sides, and with the same travel range as the wheels. Finally, and in stark contrast to the streamlining of traditional automobiles, the primary streamlining is not against flow in the direction of the crawler's travel, but rather against flow perpendicular to it, namely that from the motion of the ship being cleaned. This can be seen in the shape of the hydrodynamic shell.

Using these global crawler parameters, individual subsystems were then designed and integrated, as described in the following sections. First, **Section 2** will discuss the cleaning mechanism of the crawler, as its raison d'etre. **Section 3** considers the propulsion and attachment needed to keep the brush in contact with the hull, followed by the chassis in **Section 4** to hold components together, and the hydropackage in **Section 5** which moderates the forces on the crawler. **Section 6** then discusses the electronics configuration used for the prototyping, and finally, **Section 7** discusses future work and provides guidance for the furtherance of this project.

1.7 Program Objectives and Accomplishments

In order to de-risk the CRABI concept, the design of a prototype crawler was pursued, and testing done to validate key technological concepts. Thus, rather than aiming for systems integration of a complete submerged prototype, the program objective was set at optimizing the risk buy-down to engineering time ratio, and thus is focused on sub-system level validation. Systems not considered high-risk - such as the battery, navigation, and docking elements - were not pursued in detail, while those with novel characteristics, namely the cleaning implement itself, the magnetic drivetrain, and the hydrodynamics package were tested rigorously.

1.7.1 Cleaning Risk Buy-Down

The cleaning system aimed to avoid vessel biofouling via removing soft organisms such as algae before larger organisms can attach and harden, to be done with the use of a rotating polypropylene brush. Over the course of the program, the brush assembly, including the brush itself, a drive mechanism, and the suspension to keep it in contact with the vessel will be designed. Simultaneously, eight steel panels were placed into the Charles River and the Boston Harbor for a six-week incubation period. The natural biofouling thus formed was used to test the efficacy of the brush assembly, as well as for shear analysis of the biofouling film to improve program environmental understanding.

1.7.2 Drivetrain Risk Buy-Down

To ensure that the crawler remains in contact with the hull for cleaning, the drivetrain must magnetically glue CRABI to the hull of the vessel, and provide forward propulsion to the crawler. Sufficient downforce to ensure attachment and resist drag via friction must be present, requiring careful use of magnets and flexible suspension. These form the dual primary risks of the drivetrain: will it provide enough down force, and will it be flexible enough to conform to a ship’s hull. Accordingly, a full scale prototype of the wheel assembly, suspension architecture, and magnetic attachment modules were constructed and tested.

Additionally, the rotating seal interface on the motor mount is a meaningful risk to crawler function, and thus sub-assembly seal and corrosion testing on the motor enclosure will be conducted.

1.7.3 Hydropackage Risk Buy-Down

The hydropackage shell is designed to encompass CRABI's internal systems, with the objectives of reducing drag from the flow of water induced by the motion of the parent vessel and avoiding lift due to the same flow. To meet these objectives the team simulated multiple design concepts in ANSYS Fluent CFD (Computational Fluid Dynamics) software to search for a design that minimizes both drag and lift of CRABI. Scaled 3D printed models of two designs were tested in a tow tank at 2 knots. Force sensors were used to observe the drag and lift force readings while the test was being conducted, and the results were used to validate the CFD results.. Results from the CFD simulation accurately predicted the results of the scaled model test, so it can be assumed that the CFD simulation of the full sized crawler will also be accurate. Because neither model was found to function as required, design iteration has continued and new concepts have been generated, but not yet tested.

2. Cleaning Subsystem

In order to meet the cleaning requirement of the system as outlined in **Section 1.5**, the team incorporated a mechanical cleaning brush with rigid support arms attaching to the crawler's chassis. This section covers requirements specific to this sub-system in **Section 2.1**, an overview of the design components and cleaning plan in **Section 2.2**, brush architecture in **Section 2.3**, details on brush testing in **Section 2.4**, the brush design and parameters in **Section 2.5**, motor selection in **Section 2.6**, and finally some details on the mounting and suspension system in **Section 2.7**.

2.1 Functional Requirements

The primary purpose of the cleaning system is to remove biofouling, focusing on cleaning off soft organisms in the stage prior to barnacle formation as described in **Section 1.3**. In order to clean properly, the suspension must provide a minimum normal force on the hull as well as accommodate for any hull terrain irregularities.

Table 3. Cleaning subsystem functional requirements

Functional Requirement	Target Value	Source	Verification
Removes soft biofouling	Estimated at 2kPa shear	Adhesion strength of soft biofouling [9]	Testing
Provides sufficient normal force	76 N	Testing	Suspension analysis

Maneuvers bumps	13 mm tall bumps	Weld line height	Suspension analysis
Navigates hull curvature	1.3 m radius	Bulbous bow tightest radius [20]	Suspension analysis
Operates in ocean environment	N/A	N/A	Material selection

2.2 Prototype Design

2.2.1 Overview

Figure 6. Isometric view of the CAD model of cleaning suspension and brush.

The cleaning subsystem is made up of a rotating, open wound brush powered by a motor (ref. BL23E33-02) from Lin Engineering, the same that are used for the drive motors. The motor is mounted on the chassis and rotational power is conveyed via a timing belt to the cleaning shaft. Parallel to the belt, the brush's suspension consists of two arms mounted to the chassis with a linear spring to bias the brush toward the hull, producing the necessary normal force for cleaning. The brush parameters were primarily determined through initial testing and conceptual downselection through first order analysis as described below.

Initial cleaning strategies covered a large range of possibilities from direct heating to UV, oxygen deprivation, and mechanical solutions. Proposals were evaluated based on cleaning effectiveness, specific energy requirements, and complexity, among other metrics. The Pugh Chart in **Appendix 11.4.1** shows an overview of the methods considered as well as their expected performances. Mechanical cleaning, specifically brushing, was selected for its high effectiveness with a low energy requirement and low complexity.

2.2.2 Brush

Within the category of a mechanical brush cleaner, a few different brush architectures were considered. Below in **Table 4**, stationary slab cleaning, linear scrubbing, two-dimensional rotary, and rotational cylinder cleaning are compared based on effectiveness, simplicity, and risk of biofoul buildup on the brush itself (captured by the metrics: 'cleanability of brush' and 'distributed edge cleaning'). These results point toward rotary cylindrical cleaning as the most promising brush architecture.

Table 4. Brush Architecture Pugh Chart

	Cleanability of Brush	**Distributed cleaning edge**	**Effectiveness**	**Design Simplicity**	**Scalability**
Stationary Slab	Low: brush is never exposed to water flow	Low: front edge always leads	Low: not considered by prior 2.013	High: no separate cleaning motor	Low: length scales linearly with increasing passes
Side-to-side slab	Low: brush is never exposed to water flow	Medium: brush perimeter is always leading edge	N/A: not previously tested	Low: linear motion more difficult than rotary	High: increase scrub velocity
Rotary circle(s)	Low: brush is never exposed to water flow	Medium: brush perimeter is always leading edge	Mid: effective, but leaves dirty strip between multiple discs	Mid: rotary, potentially several motors	High: increase rotational velocity for more passes
Rotary cylinder	High: brush rotation exposes all sides to water	High: all parts of the brush share equally in pushing debris	High: prior 2.013 testing	Mid: rotary motion, likely one motor	High: increase rotational velocity for more passes

To remove load on the cleaning suspension in maintaining brush contact with the hull, particularly when the crawler is cleaning under the ship, it is important to design a brush with neutral or positive buoyancy as seen in **Figure 7**.

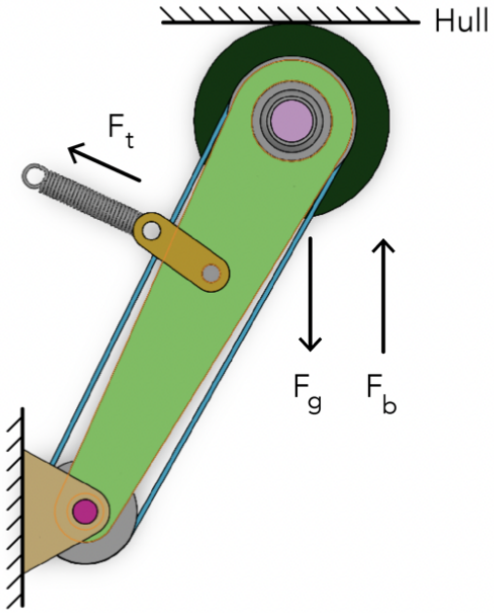

Figure 7. Diagram of the cleaning sub-system when the crawler cleans the underside of the hull. If the gravitational load is not balanced by the buoyant force of the brush, it will add torque requirement to the cleaning suspension over the 76 N of required normal force. Instead, designing a positively buoyant brush relieves some of the torque requirement on the suspension.

To attain at least neutral buoyancy, the team selected a custom open wound brush from Precision Brush, which cleans as a rotary cylinder, but significantly reduces the weight compared to a close wound or full cylindrical brush. This layout of the bristles forces biofouling outward from the center of the brush as it sweeps and allows the flow of water to better clean the bristles with each rotation. Polypropylene was chosen for the bristle material because it remains stiff when wet and does not react with chemicals that may be in the water. Using black polypropylene ensures that the brush is UV resistant which is useful in the harsh marine environment. The open wound brush is welded to a hollow stainless steel tube to provide a structural outer core. Inside the stainless steel outer is a low-density polyethylene foam inner core which lowers the density of the assembly and ensures at least neutral buoyancy. A cross sectional view of each layer of the brush assembly can be found in Figure 8.a and an illustration of the open wound pattern can be found in Figure 8.b.

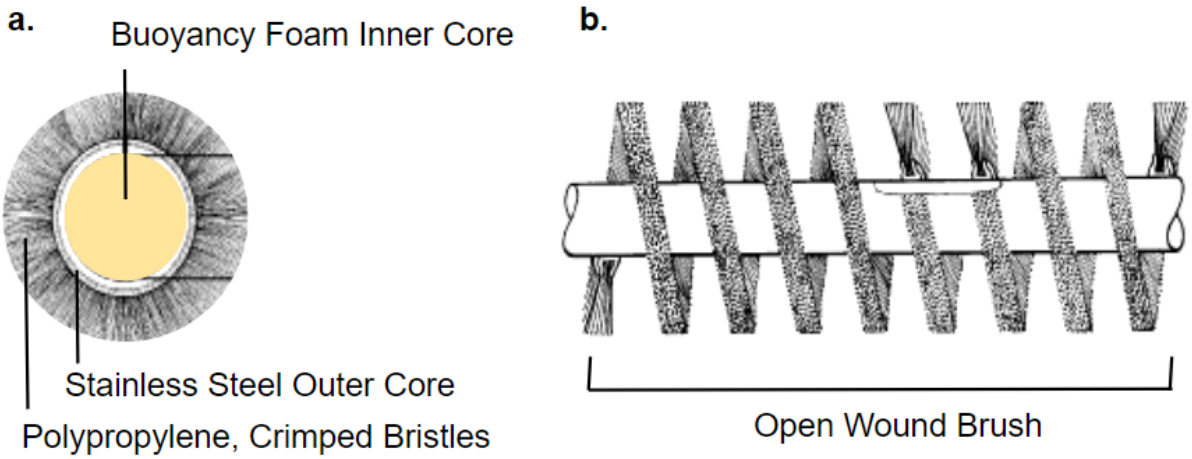

Figure 8: **a**, Cross-sectional view of the brush assembly. Low-density buoyancy foam inner core pictured in yellow, stainless steel outer core as white rings with polypropylene, crimped bristles on the outside. **b**, Side view of the brush. Bristles form an open wound pattern to minimize weight and maximize water flow cleaning potential. The white tube pictured in the center is the outer core.

The wound part of the brush has a 10 cm (4") outer diameter, 5.08 cm (2") inner diameter, 101.6 cm (40") length, and 7.9 mm (5/16") stainless steel channel, with 10 cm (4") lead between loops, for holding the 0.076 cm (0.030") bristles. The stainless steel outer core has a 5.08 cm (2") outer diameter and 0.165 cm (0.065") thickness. The polyethylene inner core has a 5.08 cm (2") diameter [35].

The weight calculations assumed a cylindrical brush to provide a safe estimation of the weight of the assembled brush. The brush was projected to weigh 6.124 kg (13.5 lbs), as shown in **Table 5**, which results in a density of 739 kg/m^3. The density of seawater is 1026 kg/m^3, so the projections resulted in a positively buoyant brush.

Table 5. Estimated Brush Density by Component

Material	Volume [cm^3]	Mass [kg]	Density [kg/m^3]
Polypropylene (bristles)	6,214	4.97	800
Steel (outer core)	132	1.06	8,000
Foam (inner core)	1,939	0.093	48
Combined	8,285	6.124	739

Euler beam bending calculations were performed to verify structural integrity of the chosen design under a uniform distributed load. The results showed that the thin core undergoes only 1.1 mm of deflection at the brush midpoint and does not yield, as per the equation below, where the bending moment of inertia for the tube was taken as $I = \frac{\pi(OD^4 - ID^4)}{64}$.

$$v_{def} = \frac{5wL^4}{384EI} \quad (1)$$

2.2.3 Mounting Suspension

Figure 9 shows a side view and cross section view of the cleaning assembly. An extension spring is used to maintain normal force from the brush towards the hull. A timing belt and pulleys are used to transmit power between the cleaning motor and brush. Joints in the support arm are designed to accommodate bumps and hull curvature.

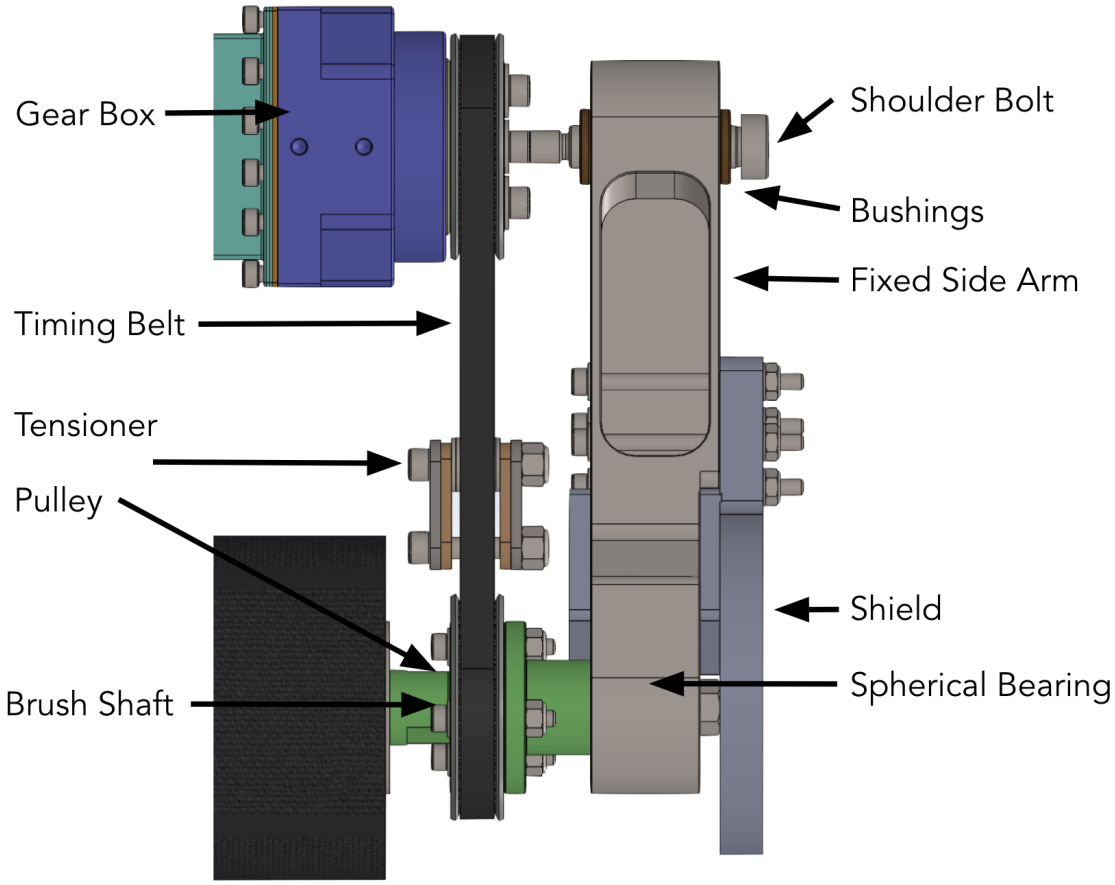

Figure 9. Front view of the cleaning subsystem. The support arm includes a pin joint at the top where it attaches to the chassis and a ball joint where it attaches to the brush shaft. A timing belt and pulleys are used to transmit power from the cleaning motor to the brush.

The design requires the cleaning subsystem to be light (less than 10 kg.), while withstanding drag forces from water flow, as shown in figure 9. With a rectangular cross section, at a target weight of 0.5 kg per arm, the arm does not have a moment of inertia large enough to meet the bending displacement design requirement. The drag force on the arm was calculated using the parallel surface area of the arm, density of seawater, velocity of a panamax-size ship (10 m/s), and a drag coefficient of 1.3, resulting in **266 N of drag**.

$$F_D = 0.5 \cdot p \cdot v^2 \cdot C_D \cdot A \quad (2)$$

At the target weight, an I-beam cross section has a greater bending resistance to distributed loads, resulting in a substantially larger moment of inertia per mass (278,000 mm^4) as compared to a rectangular cross section (35,000 mm^4), resulting in a **total arm stiffness of 293 N/mm**.

$$S = 3 \cdot E_{SS316} \cdot I_{Ibeam} \div L^4_{arm} \quad (3)$$

Rotational power needs to be transmitted from the cleaning motor to the cylindrical brush at the end of the support arm. The cleaning motor is designed to be fixed to the chassis instead of moving with the support arm to avoid adding weight to the support arm. A 10mm pitch high torque drive (HTD) timing belt and matching pulleys are used to transmit torque from the motor to the brush shaft. The two S5M high torque timing belt pulleys from Misumi (part HTPS32S5M100-A-HUK) are rated to provide over 30 Nm of torque at 200 RPM and thus have a large margin of safety compared to the torque requirement of 1.14 Nm [37].

The distance between the shoulder and wrist was not calibrated to the teeth/belt circumference ratio of the pulleys. To compensate, a pulley tensioning mechanism was incorporated into the design (figure 10). A stainless steel bearing applies proper pressure to keep the belt tensioned and aligned. The applied pressure can be adjusted by regulating the position of the bearing along a curved path, which is welded onto the chassis. A known error with the pulley tensioning mechanism is interference from the motion of the arm as the brush travels over irregularities (bumps, weld lines, curvature) on the ships hull. The rotational arm travel creates mechanical miscalibration, which at best makes the tensioner ineffective, and at worst interferes with the torque transfer along the pulley belt. Accommodating for weight and machinability, the solution would be to attach the tensioning mechanism to the arm, so it travels with the pulley and maintains a constant distance from the timing belt.

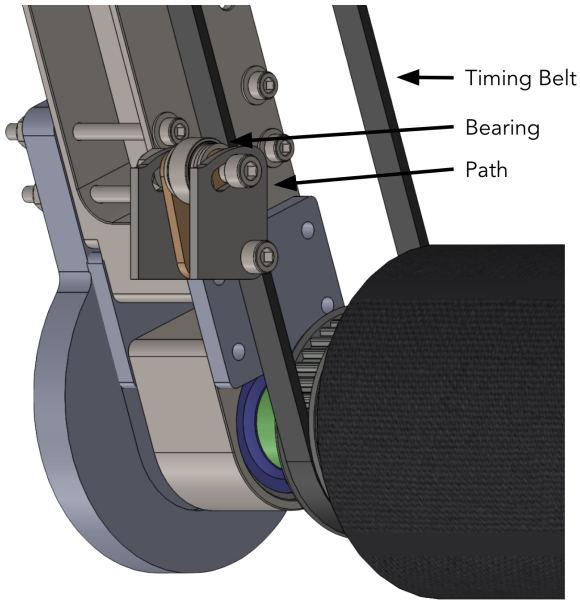

Figure 10. Pulley tensioning mechanism

As shown in **Figure 9**, the support arm houses a pin joint at the top and a ball joint at the lower connection to the brush. The pin joint accommodates bumps in the hull that require both arms to move up and down together. Meanwhile, the ball joint affords an extra degree of freedom that allows the two support arms to move independently of one another. This extra degree of freedom is useful for maintaining contact with the surface of the hull in areas that have curvature along multiple directions.

The pin joint is designed as a shaft through two bushings (also known as sleeve bearings). An open concern of the pin joint is that there will be a side load distributed along the support arm due to the drag from the flow of water along the hull (and therefore perpendicular to the crawmer's movement). The bushings and shoulder bolts were sized with respect to bending displacements due to drag force. The deformation of the shoulder mountings was calculated using Hertzian contact mechanics, approximating the bushings and shoulder bolts as cylinders in contact with parallel plains. The stiffnesses are governed by a contact force of the below equation, proportional to length of cylinders L and indentation depth d.

$$F = \pi \div 4 \cdot E \cdot L \cdot d \tag{4}$$

Bronze bushings sourced from McMaster (ref. 2934T11) have a stiffness of 580,000 N/mm with respect to the pin contact, and 290,000 N/mm with respect to the housing contact, resulting in an effective radial stiffness of 194,000 N/mm and a **bushing displacement of 0.017 mm**.

With a relatively complex shoulder and wrist mounting system, overconstraint was an open cause for concern. Accounting for the substantial drag load the cleaning subsystem is under, mechanical binding is both likely and severely impacts function. Without mitigation for overconstraint, the cleaning subsystem has -1 degrees of freedom (table 5), which requires a reduction strategy.

$$Desired\,DOF\ -\ Constraints\ =\ (18-4)-5=\ -1$$

Constraint	DOFs
Fixed Shoulder Bushing	4
Free Shoulder Bushing	4
Fixed Shoulder Axial	1
Free Shoulder Axial	1
Fixed Spherical Bearing	2
Free Spherical Bearing	2
Fixed Wrist Axial	1

Table 6. Constraints and associated degrees of freedom restricted in the shoulder, arm, and wrist configurations.

To re-introduce one degree of freedom back into the system, a double blade flexure (figure 9) was added. In order for the flexure to be effective, the stiffness of the flexure must be at least one order of magnitude smaller than the stiffness of the arm and the bushing. Stainless steel sheet metal of 0.036” thickness results in a **flexure bending stiffness of 0.013 kN/mm**, which is significantly smaller than the total stiffness of the arm and the bushing (1.6 kN/mm). However, a flexure this compliant has a negative margin of safety. To mitigate this, a 3D printed shield (figure 9) was introduced to decouple the drag force on the arm and flexure. The shield has the added benefit of absorbing the drag force on the brush (558 N).

The brush core, once a singular body, was broken up into four subcomponents to allow for easy brush replacement (figure 8). The core now consists of the central shaft caps to which the bristles will be mounted on, and two shafts which have threaded ends that screw onto the central shaft and locating features for the arm mounting hardware.

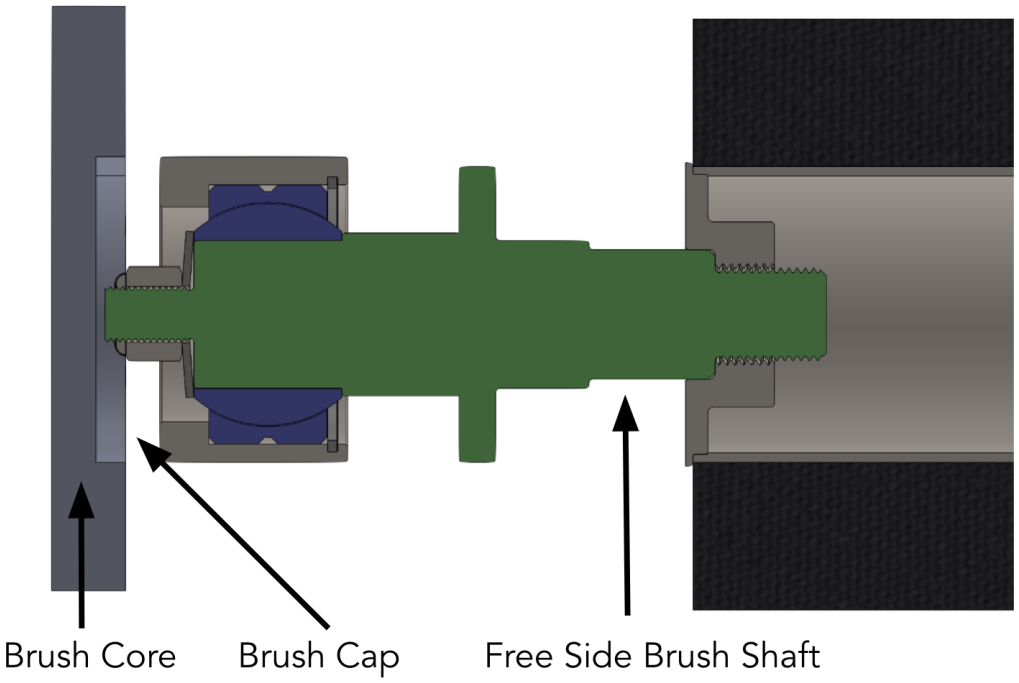

Figure 11. Brush core, fixed side.

2.2.4 Drive Selection

The cleaning brush will use a brushless motor (ref. BL23E33-02) from Lin Engineering for efficiency and cost benefits. The chosen gearbox is the EG23-G20-D8 (from StepperOnline), similar to what is used for the wheel assembly. For the cleaning sub-system, the motor only needs approximately 20 W of power.

The torque requirement may be found by multiplying the frictional force by the brush radius. The normal force determined from testing to remove most biomass was 24N from the circular brush used. Scaling this up to maintain equivalent pressure for the cylindrical brush assuming a 2.5 cm (1") width of contact between the brush and hull across the 101.6 cm (40") length, this translates to 76 N of normal force. As mentioned previously, the cylindrical brush radius is 10 cm (4"): the hull coefficient of friction was assumed to be 0.3, resulting in **1.14 Nm of torque**.

$$\tau = F_f \cdot R_{brush} = \mu \cdot F_N \cdot R_{brush} \quad (5)$$

The speed requirement was found by taking the crawler's linear speed, $v = 0.8\,m/s$, together with the assumption that one pass of the circular brush (average of 5.1 cm (2") linear contact length, $L_{contact,f} = 5.1\,cm$) is sufficient to remove soft biofouling. Under linear motion only, the cylindrical brush provides a 2.5 cm (1") linear contact length of scrubbing (

$L_{contact,i} = 2.5\,cm$), so rotation must account for the remaining $L_{contact,f} - L_{contact,i} = 2.5\,cm$ per initial contact length. This translates to 3.1 rev / sec, or **188 RPM** as calculated from the equation below.

$$Rotational\ Speed\ (RPM) = (L_{contact,f} - L_{contact,i}) \cdot \frac{1}{L_{contact,i}} \cdot \frac{1}{\pi D_{brush}} \cdot v \qquad (6)$$

2.3.1 Overview

Prototype fabrication was accomplished by outsourcing to external vendors. The brush core and flexures were machined at MIT, taking advantage of maker spaces accessible to students. Assembly confirmed the success of kinematic design. The tolerances on the bearing block oversized the inner diameter, and material had to be removed to prevent binding on the spherical bearings.

2.3.2 Sourcing

The majority of the machinable components were sourced from Fictiv, for a total of $3,453, which allows for one complete subassembly with spares. The stainless steel sheet metal for the free side flexure (0.036” thick) and the fixed side flexure (0.25” thick) was purchased from Xometry supplies in 12x12” plates. The hollow stainless steel cylinder stock for the brush outer core was also purchased from Xometry supplies. The open wound brush was purchased from Precision Brush. Ordering one brush would have cost $250. An additional brush only increased the total cost by $70, so two brushes were purchased. The foam inner core was purchased from Foam Factory Inc..

2.3.3 Learnings

The introduction of the flexure created an asymmetry between the two arms, as it designates a fixed side arm (effectively a rigid body) and a free side arm (effectively two rigid bodies, separated by a thin wall geometry). The fixed and free brush shafts are also asymmetrical, as the fixed side brush shaft requires extra length to accommodate the pulley. With CNC machining, quantity greatly affects the cost per part. This is because start-up costs are relatively high and, when quantities are small, they represent a big percentage of the cost. With large quantities, however, the per-unit costs decrease. To take advantage of economies of scale, the fixed side arm was replaced with a duplicate of the free side arm, with a thicker sheet metal replacing the flexure to provide appropriate stiffness and bending resistance. In future iterations of the design, it is recommended to make the fixed and free side brush shafts symmetrical. Extending the length of the free side brush shaft (figure 11) has the added benefit of increasing the spacing between the arms, which simplifies the locations of the welds to the chassis.

The brush core (figure 11) was not designed with DFM and cost reduction in mind. The quote from Fictiv was too expensive, and the quoted timeline was too long for such little machining. The decision to machine the brush core in house was made to reduce lead times and compensate for the high cost of the brush shaft (figure 11) and arms (figure 9). Instead of a machined lip, further iterations of the shaft should be redesigned to press fit directly into the stock. If the tolerances on the cylindrical stock are too loose, laser cutting the ends of the tube could be explored.

2.4 Brush Testing

Testing efforts were focused on understanding the growth rate of biofouling and assessing the biofouling response to shear force. Discerning the impact of rotational speed on the biofouling removal capabilities of the cleaning assembly was descoped.

In order to understand the growth rate of natural biofouling, steel sheets were submersed in bodies of water around Boston to grow algae. Six 24x48 " steel sheets were placed at the Drydock Green Space at Black Falcon Terminal, the Charlestown Marina, and the MIT Sailing Pavilion. Steel was chosen to emulate the ships hulls intended for CRABI to attach to. The plates were secured with rope to floating docks to hang just below the water surface. A qualitative assessment of biofouling growth was documented periodically until there was adequate biofouling coverage for testing purposes. After a month of growth, as seen in Figure 12, the biofouling in both saltwater and freshwater was significant enough to be used for future testing.

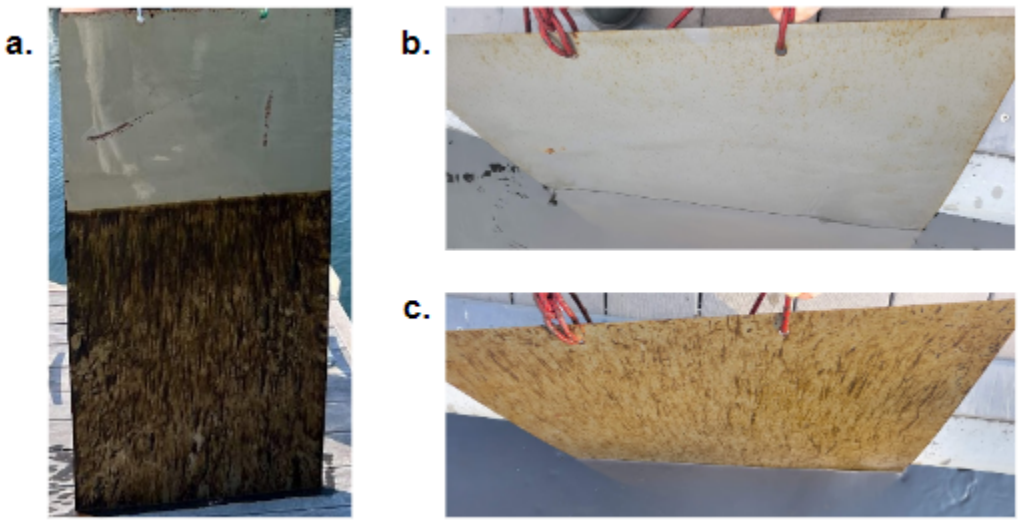

Figure 12: Biofouling growth documentation- **a**, after one month of growth in saltwater, there is a thick layer of algae. **b**, after two weeks of growth in

freshwater. A light layer of fouling can be seen near the edges of the plate. c, after one month in freshwater, the biofilm covers the plate.

The biofouling response to shear and normal forces was tested using samples from the Charlestown Marina. The sample was placed on a force plate to capture the normal force. A circular brush with a center shaft was placed on the sample. The center shaft allowed for weight plates to be added to the brush to vary the normal force. A dual-range force sensor measured the shear force that was applied to the brush. Pictures were taken before and after each run.

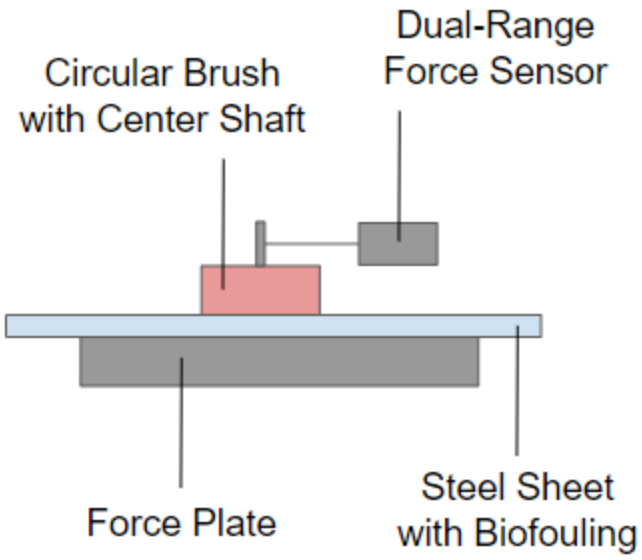

Figure 13. Side view of the cleaning test setup with circular brush. Weights were added to provide varying amounts of normal force.

The shear and normal forces needed to remove biofouling from the steel sheets were both significantly lower than expected. Figure 14 shows a before and after picture of one testing run with a circular brush taking a straight path over half the width of the sample. It was found that a shear stress of 0.67 Nm and a normal force of 24 N were needed to remove a significant portion of the biofouling. The limitations of this test include that the brush was moved relatively slowly compared to the intended speed of the brush when the crawler is attached to the hull. There was also no water flow over the testing area or the brush, so the conditions were different than the intended application. A smaller scale analysis with a texture analyzer could be useful for understanding the bristle level interaction with the biofouling.

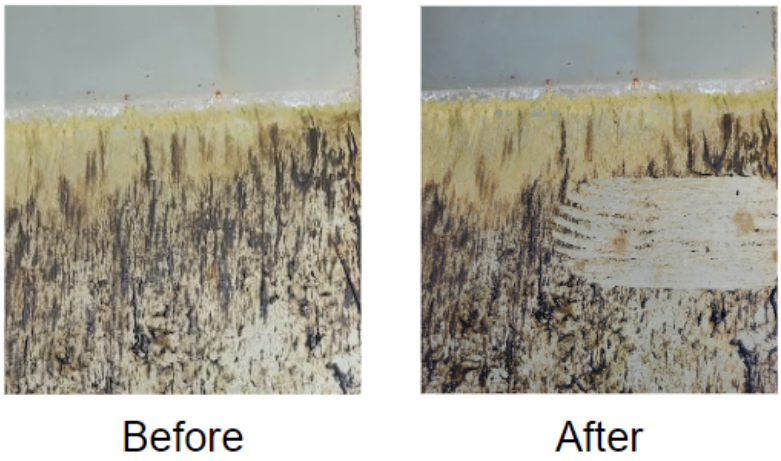

Figure 14. Before and after picture of biofouling after test. This plate was submerged at the Charlestown Marina for 6 weeks.

3. Attachment & Propulsion Subsystem

To ensure that the crawler remains in contact with the hull for cleaning, the attachment and propulsion systems magnetically glue CRABI to the hull of the vessel, as well as provide forward propulsion to the crawler. The primary design difficulty with the subsystem is the need for downforce in the absence of gravitational adhesion - or even with a gravitational force oriented so as to cause detachment. This downforce is needed to create high lateral friction, but must also simultaneously permit efficient forward motion. Magnetic skis, mounted to sprung wheel assemblies, are used to provide this downforce. Based on the requirements developed in **Section 3.1**, **Section 3.2** discusses the design arrived upon, including the magnetic skis, the wheels, suspension, and the motors. Then, **Section 3.3** provides an overview of the results and fabrication process for the constructed prototype, as well as the learnings therefrom towards future designs.

3.1 Functional Requirements

Together with the vehicle global parameters, the adhesion and propulsion requirements for the powertrain were refined into numerical criteria of thrust and resisted drag. With the crawler speed set at 0.8 m/s, the thrust and power of the drivetrain could be computed, and combined with a preliminary mass estimate for CRABI, sizing of the drivetrain components became possible, per the requirements articulated in **Table 7**.

Table 7. Attachment & Propulsion System Requirements

Functional Requirement	Target Value	Source	Verification
Crawler Speed	0.8 m/s	Design criteria balancing	Motor sizing
Resist Drag Force	4,230 N	Design criteria balancing	CFD
Resist Brush Friction	22.5 N	Brush testing	N/A
Power Budget *Steady state*	180 W	Design criteria balancing	Motor sizing
Total Mass	140 kg	Design criteria balancing	CAD mass estimate
Mass Allocation	70 kg	Design criteria balancing	CAD mass estimate
Terrain Step Height	8” (5.0cm)	Weld line	Suspension travel
Terrain Minimum Curvature	1.3m	Bulbous bow minimum radius	Suspension travel, ground clearance

3.2 Prototype Design

3.2.1 Overview

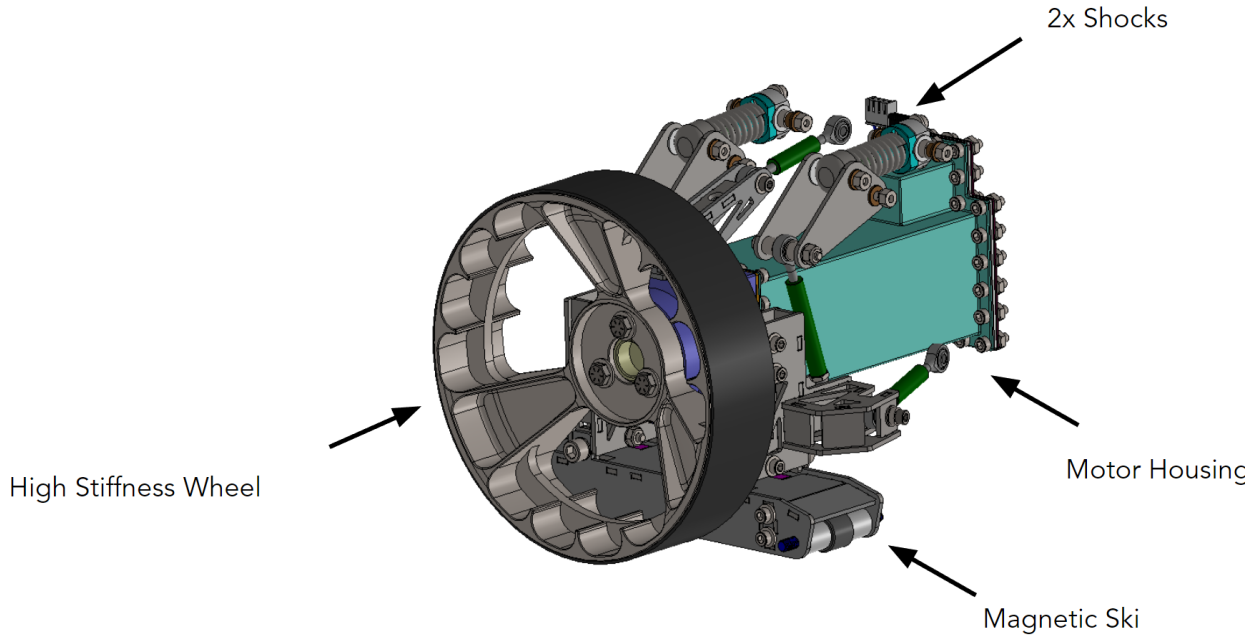

Figure 15. Isometric view of the subsystem's architecture, including the magnetic skis, the suspension, the motor housing, and the drive wheel.

The attachment and propulsion functional requirements drove the implementation of **magnetic skis**, capable of producing a magnetic adhesion pressure while hovering above the hull surface, providing high friction to lateral motion while also permitting efficient forward motion. **Six wheels** are then used as in a more traditional automobile, each with a magnetic ski attached, and with a motor mounted coaxially within each wheel assembly. While four wheels would suffice for propulsion, the need to maintain pitch stability when the front wheels drive over a bump - and thus loose magnetic adhesion - drove the wheel count up to six. Finally, the six wheel assemblies are sprung to the crawler body to provide terrain flexibility. As seen in **Figure 15**, an **inverted suspension** architecture is used, capable of withstanding the high lateral loads expected while also avoiding camber change during suspension travel. The skis and motor are rigidly connected via the upright, which connects to the suspension ball joints.

3.2.2 Halbach Ski Attachment

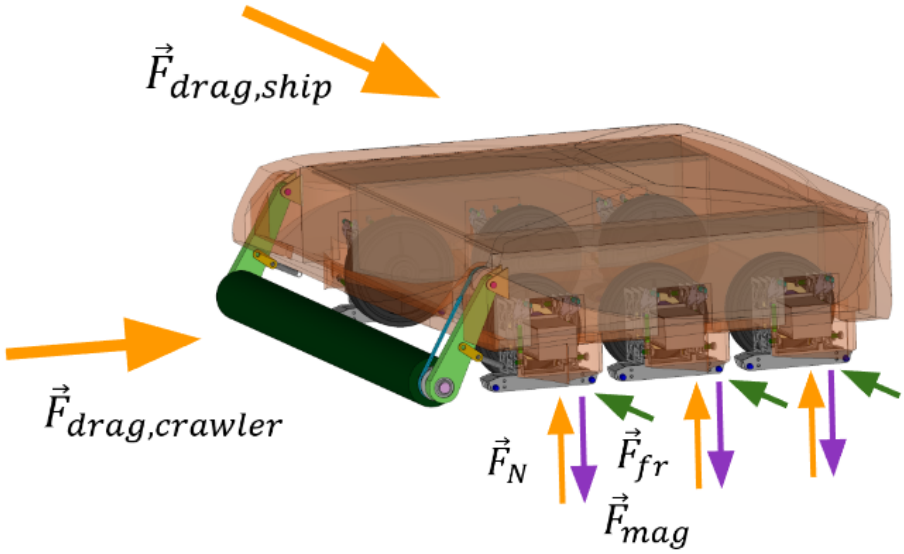

Figure 16. Diagram of the primary forces on the crawler, with external forces shown in orange, including the drag due to the motion of the ship, $F_{drag,ship} = 3,700\ N$, the drag due to the motion of the crawler, $F_{drag,crawler} = 44\ N$, and the normal force due to the hull, $F_N = 10,500\ N$. Shown in purple is the magnetic adhesion force, $F_{mag} = 10,500\ N$, together with the frictional force at the wheels, $F_{fr} = 3,700\ N$, shown in green.

The crawler needs to remain attached to the hull of the ship while the ship is in transit. As seen in **Figure 16**, it must react to a significant **drag force** of 4.6 kN from the motion of the parent vessel. The frictional force required is determined from the coefficient of friction and normal force, and must be equal in magnitude to the drag.

$$F_{mag}\mu \geq F_{drag,ship} \tag{7}$$

The high normal force needed to create that friction is achieved by magnetic adhesion force. **Halbach skis** — Halbach arrays mounted on ramped skis offset 5mm from the hull — were selected over magnetic tracks for their greater tolerance to gapping. Magnetic tracks were considered but eliminated due to both their maintenance complexity and their rapid loss of adhesion pressure over as little as a 1mm gap. In contrast to the typical inverse square drop-off of magnetic attachment force with gap size, Halbach arrays show exponential decay of attachment force proportional to the array size [38].

Indeed, this gap flexibility not only avoids undesirable friction with the hull, but also provides tolerance to hull irregularities and non-magnetic material, such as the very fouling this crawler must eliminate. The Halbach skis thus allow for a magnetic attachment architecture that provides sufficient downforce even while maintaining a nominal gap distance from the hull.

The skis used are shown in **Figure 17**, as a cross-sectional view. Steel rollers - needle bearings - are used on either end, offset 1mm below the magnet surface, to ensure that even when driving over bumps, the magnets do not drag along the hull surface. The ski itself is assembled via sheet metal construction, held together with bolts, and the magnets are attached to the steel via a marine epoxy, yet to be selected. 12 neodymium magnets, of grade N52, are used to provide the needed attachment force, including a factor of safety of $FoS = 1.33$. This is targeted to ensure that even if any two wheels lose adhesion, sufficient attachment force remains, as well as to provide a buffer to uncertainty. Due to the expense of the magnets, a low margin of safety beyond this factor of safety is used. This value is highly dependent on both the exact values of μ and F_{mag}, and thus testing was conducted to validate both parameters.

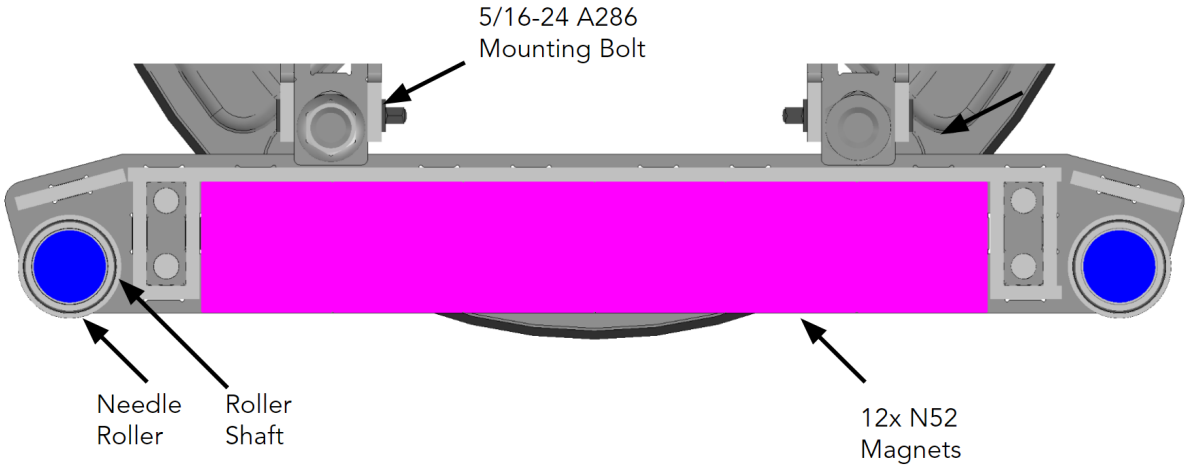

Figure 17. Orthogonal view of one of the Halbach skis. The steel rollers are indicated within the view, as are the cubic magnets, shown in purple, and the shafts on which the steel rollers rest. Note that the shafts have male threads on either end, and together with the bolt holes near them, provide the clamping force to pin the ski assembly together. The holes for the 5/16-24 bolts are slotted to permit adjustment of the gap thickness of the skis, and A286 bolts are used to generate sufficient clamping force to resist the ski load in friction.

Simple inclination tests were sufficient to determine the rubber coefficient of friction; in order to confirm that sufficient downforce will be present to utilize it, sub-scale magnetic attachment testing was performed on an Instron to verify the predicted force at varying gap size. As shown in **Figure 18**, a 5x2 Halbach array of 5cm (½") cubic permanent magnets was

mounted to an Instron. The permanent magnets had through holes for ease of assembly and testing of different array configurations. The Instron then measured the changing attachment force between the magnet array and a bar of A36 steel while pulling the array upwards, away from the bar.

Figure 18. Magnetic attachment test setup: 5x2 Halbach array mounted in an Instron.

As can be observed in the "Plain Array" plot in **Figure 19**, the measured relationship between attachment pressure and gap size is exponential, which matches the theoretical relationship for Halbach arrays. The measured pressure at zero gap was 350 kPa – this was only around half of the theoretical pressure of 600 kPa for an idealized infinite Halbach array. The discrepancy between theoretical adhesion pressure and measured adhesion pressure may be caused by the non-uniform magnetic field from the holes in the magnets, or due to flux leakage along the sides of the array, as the analysis assumed an array of infinite size.

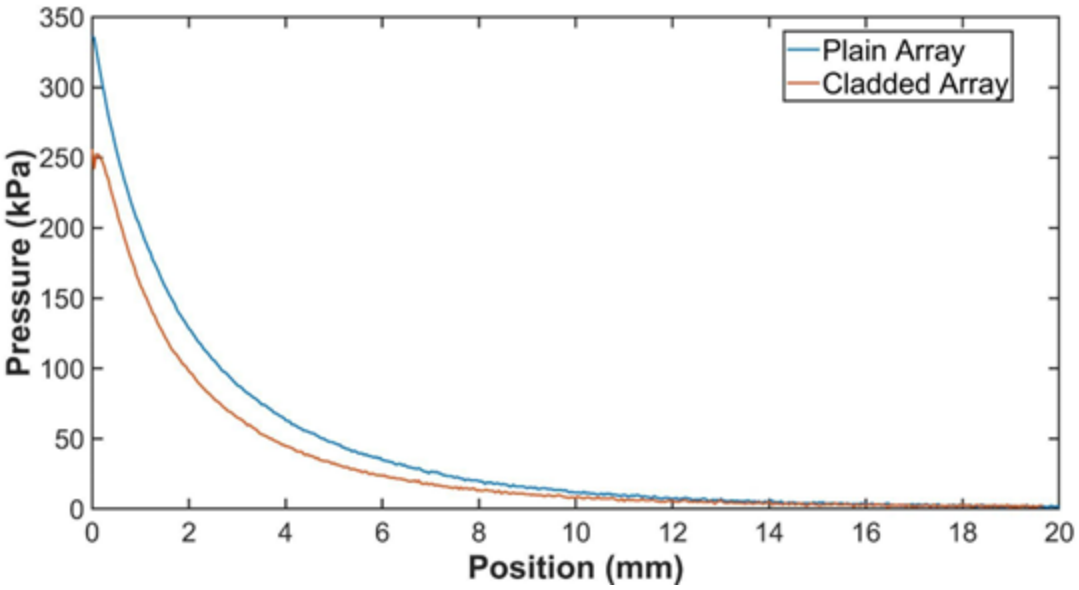

Figure 19 Plot of magnetic adhesion pressure at increasing gap size, for both the exposed and the cladded array tests. For the sub-scale test conducted, the equivalent gap to the full-scale value occurs at 2.5mm, and the plots show substantial force remaining at this value. Unfortunately, it can also be seen that the cladding decreases the total force available.

3.2.3 Wheels & Tires

Unfortunately, the sensitivity of the magnetic skis to the gap thickness in **Figure 19,** when coupled with a finite stiffness of the wheel and tire, can result in a self-reinforcing cycle driving the ski closer to the hull. Since the magnetic force would then increase, so would the deformation of the wheel, and thus the ski would get yet closer to the hull – a negative stiffness to displacement towards the hull, and thus an unstable one. The design of a stiff wheel was thus undertaken, and testing of rubber tires for maximum stiffness conducted.

While initially, a thin sheet of rubber is quite compliant – see the stiffness curve of **Figure 20** prior to the knee – it then becomes stiff past a small amount of initial deformation, behaving rather unlike a metallic material in the high stress regime. A thin rubber sheet covering the wheels can thus be used as the tire without losing significant stiffness.

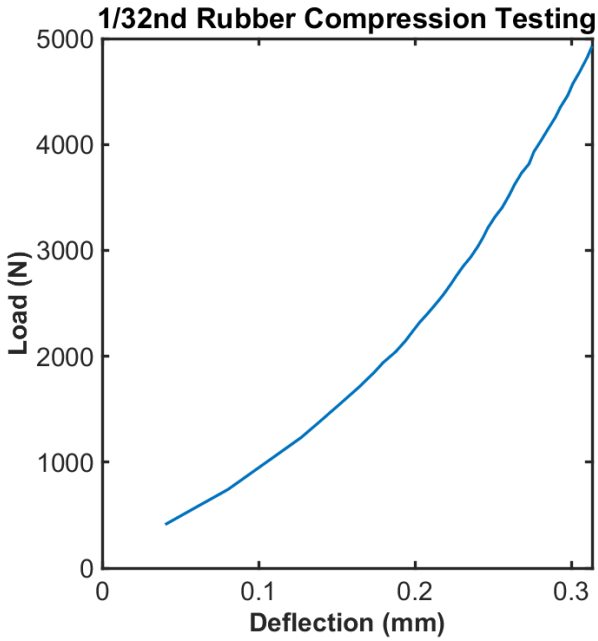

Figure 20. Rubber applied load vs deflection for a 1/16" sheet from testing, intended to be used as a thin tire to provide traction. Note the knee around 0.4mm deflection as the slope increases significantly. In contrast to metallic plasticity, the rubber gians stiffness at high strain, allowing for its use here.

Next, a stiff but lightweight aluminum 7075-T6 wheel was designed, shown in **Figure 21**, and then analyzed via the Finite Element Method. Results of a stiffness simulation are shown in **Figure 22**. Key features of the wheel design include the ribbing to prevent crumpling of the wheel rim, thus utilizing the full tire width for load distribution, and a central support under the rim for local hoop stiffness. Additionally, the raised lip around the inner diameter of the wheel center provides additional bending stiffness in the spokes for very low mass cost. Combined, even under the maximum expected magnetic pressure the total wheel and tire deflection is under 1mm, creating sufficient stability to counteract the negative magnetic stiffness. The total weight of the wheel center is only 816g, despite being 8" (20cm) in diameter.

Figure 21: Isometric view of the wheel design. The tire is affixed to the wheel via first sewing a flat sheet into a hoop, using stainless steel lockwire for thread, and then pressing it over the wheel center. A knurled surface over the outer diameter of the wheel center ensures good retention of the tire.

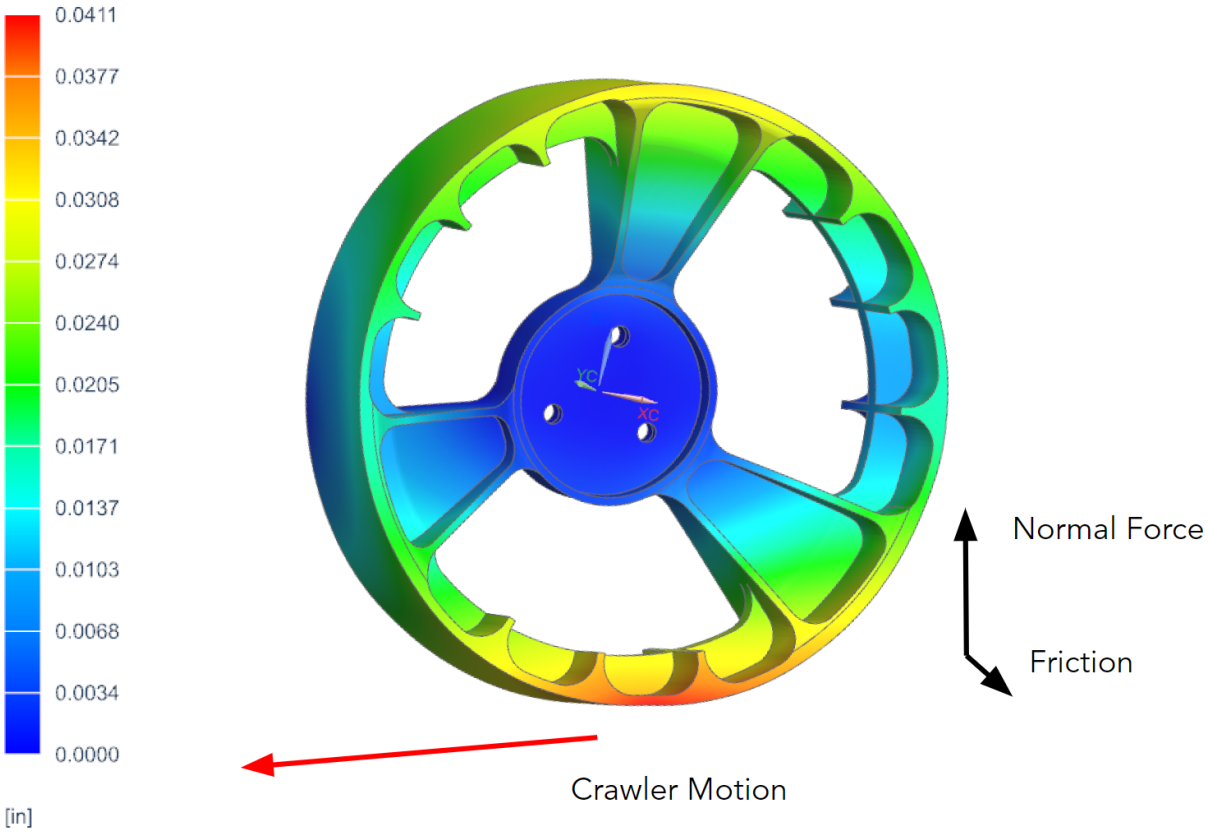

Figure 22: Finite Element Method displacement results of the wheel design under the normal loading on the wheel due to downforce created by the magnetic skis. The deformation is highest at the contact patch.

The usage of 7075-T6 for the wheel, in contrast to either a weaker (and cheaper) aluminum alloy or to a more corrosion resistant steel was determined via two key considerations. Foremost, the higher yield strength of 7075 was needed due to the stresses experienced, as revealed by the simulation shown in **Figure 23**. Indeed, this stress exceeds the strength of untempered 304 stainless steel, and thus would require the use of a hardened steel alloy. While the aluminum wheel will then create a galvanic couple against the stainless steel wheel hub, the wheel forms the anode of that couple, and will thus be the element losing material. This corrosion mechanism is further discussed in **Section 4.2.3**, but is not of significant concern for a prototype since the wheels can be readily replaced for a longer-lifetime crawler, unlike the integrated hubs.

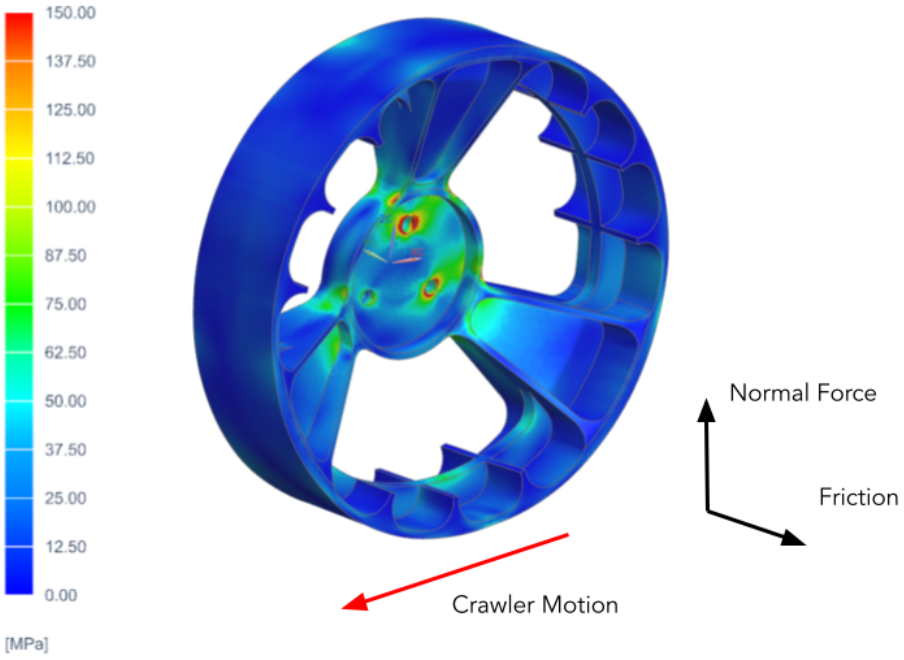

Figure 23: Finite Element Method stress results of the wheel design under the normal loading on the wheel due to downforce created by the magnetic skis. The highest Von Mises stress experienced occurs at the edge of the spokes connecting to the center, reaching a level of 161 MPa. Note that the stress seen under the bolt head is an artifact of the simulation and should be ignored.

A final design element is the bolts used to mount it to the wheel hub. While a small boss on the hub provides the primary locating features, three lug bolts are used to react the moment created by the friction on the wheel, and are thus heavily loaded. Detailed analysis of these bolts was conducted via the methods set force by NASA in a technical memorandum, and the use of ¼-28 A286 superalloy bolts found to be necessary to meet the load capability required while also maintaining good corrosion resistance.

3.2.4 Suspension

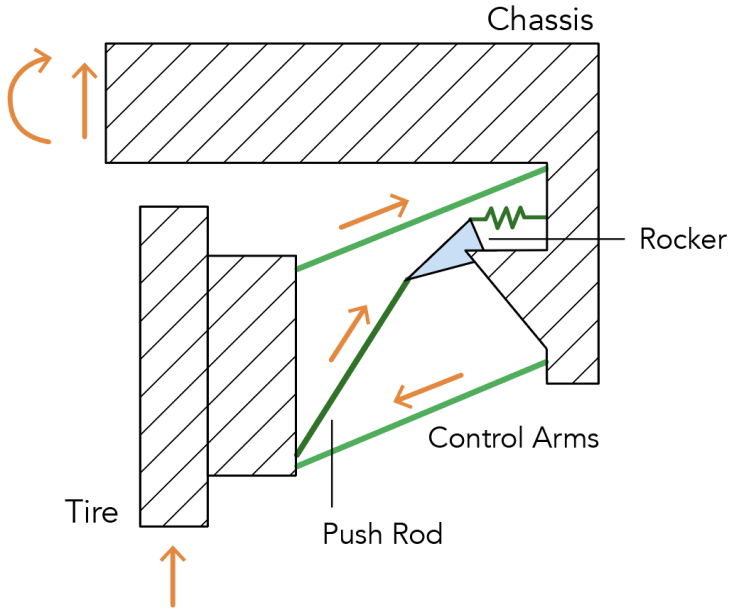

Figure 24. Orthogonal view of the suspension setup, connecting the wheel upright to the frame via the two control arms and the pushrods. The loads and reaction forces are shown via orange arrows. The pushrod is of fixed length, and a rocker is used to connect the pushrod to a compressible shock at a 3:1 motion ratio. Note the force couple created by the reaction forces in the upper and lower control arms, resulting in a net restoring moment about the roll axis.

In order to ensure that the skis and wheels remain in contact with the hull to provide downforce and traction, a suspension system was designed. Unlike traditional automotive suspension, the primary downforce for the crawler is provided not by the weight of the crawler, but instead by the magnetic skis attached to each wheel. Accordingly, although substantial suspension travel is needed for terrain flexibility — 5cm (2") — a stability problem is posed due to the roll moment created by the wheel normal force, tending to roll the crawler away from the hull. To counteract this, a doubled wishbone architecture is used, but inverted, placing the frame mounts outboard of the wheel rather than inboard. This architecture is summarized in **Figure 24**.

First, the pushrods provide an adjustable stiffness to vertical deflection, with relatively little horizontal swing. **Figure 24** provides a cartoon representation of this arrangement, including the reaction forces. The rockers, shown in blue in **Figure 24**, are used to create a mechanical advantage between the pushrods and the shocks, resulting in a 3:1 motion ratio between the pushrod and shock travel. This shorter shock travel is required due to the difficulties of creating a long travel telescoping pushrod, since the suspension must actuate by 2" (5.0cm), especially with regards to eccentric buckling and binding. The control arms, meanwhile, swing

rigidly, and together with the upright and frame constitute a four-bar linkage. Finally, the shocks absorb the vertical motion, providing finite stiffness as well as damping.

Figure 25 shows a cross section of the shocks. While an off the shelf solution would have been ideal, none were available at the scale needed and designed for a seawater environment. Indeed, due to the scale involved – the inner diameter of the shock housing is less than 0.200" – miniaturization and design for manufacturing were key, as well as avoiding binding. Press fits are used on the bushings to minimize tolerance stack ups where possible, with those bushings then providing low friction linear sliding contact. They in turn compress fluid within the shock housing, which is allowed to vent at a controlled rate through dedicated vent holes in the end.

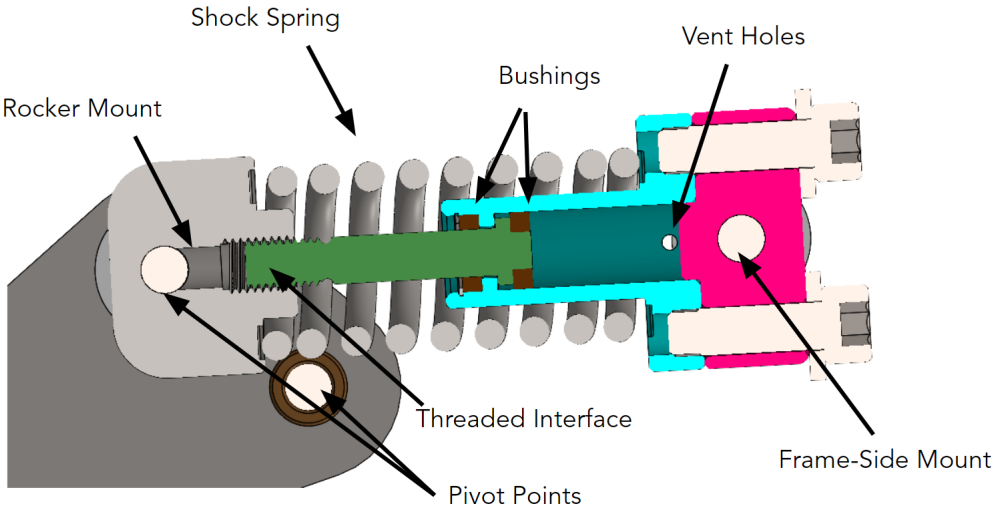

Figure 25. Cross section of the shock design, showing both the rocker side mount and the frame-side mount. Connecting these is the shock rod, with a threaded interface to enable length adjustments, which slides within the shock housing, shown in blue. In parallel is the shock spring, which together provide both motion resistance to bumps and damping to prevent resonant motion of the crawler. A vent hole is included within the shock to allow for the water to escape, as it is an incompressible working fluid.

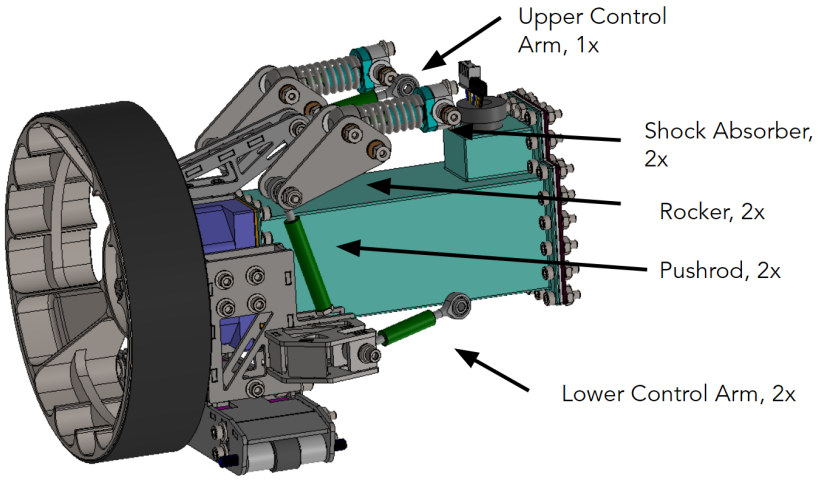

Figure 26. Isometric view of the wheel assembly with the various suspension elements labeled.

In order to package around the motor and gearbox housing, the pushrod was split into two parallel members. Likewise, the lower control arm was split in two, as seen in **Figure 26**. The latter change has the additional benefit of providing a reaction to control the wheel assembly steering axis (sometimes called the toe angle), while minimizing over-constraint. The highest load expected is a compressive force of 3.0 kN in the upper control arm, a definite buckling risk. However, when analyzed under the Johnson Buckling Criteria, the upper control arm has a high margin of safety, as shown in **Equation 8**, based on the Johnson Critical Stress shown in equation 9 [39].

$$MoS_{buckling} = 1.41 = \frac{\sigma_{Johnson}}{FoS \cdot \sigma_c} - 1 \quad (8)$$

$$\sigma_{Johnson} = \sigma_{ty} - \frac{A}{IE_{316}}\left(\frac{L\sigma_{ty}}{2\pi}\right)^2 \quad (9)$$

Each of the suspension rods is connected to the frame and vehicle upright via spherical rod ends, again to avoid over-constraint, and thus forming ten ball joints per wheel assembly. The rods themselves are assembled from 0.375” (9.5mm) diameter stainless steel tubes, directly tapped, with one end having a left-handed thread and the other a right-handed thread. Together with a set of jam nuts, this permits the length of the suspension rods to be easily tuned. The rod ends are in turn linked to the motor and ski via the upright, which constitutes both the machined bearing housing, and the sheet metal assemblies around it. These assemblies are built upon tab and slot construction, avoiding error-inducing bends, and thus maintaining tight assembly-level position tolerances thanks to the small profile errors of planar-cut sheet metal parts.

3.2.5 Motor Selection and Enclosure

The motor performance requirements were estimated from the crawler frontal drag and tire rolling resistance, as in **Equation 10**. Note, a coarse assumption for the rolling resistance was used, setting $C_{rr} = 0.01$, a value typical for wet tires on concrete.

$$F_{res} = 1/2\rho C_{d,f} A_f v^2 + C_{rr} F_{mag} \quad (10)$$

Combined, each drive motor was thus sized for 3.0 Nm at 94 RPM, and hence a continuous power draw of 33 W. Higher torques are available for short periods of time, depending on motor thermal parameters, and hence the continuous torque requirement was the driving consideration. The higher torques are needed for climbing the side of the vessel against gravity, necessitating a minimum torque of 16 Nm, and more to provide margin beyond the desired factor of safety. A brushless motor, the BLE33-02 manufactured by Lin Engineering, was chosen for its high power density, ready availability, and its packaging within a NEMA 23 form factor. The latter attribute enabled the usage of a commercially available planetary gearbox, the PLM23-G20-D8, by the same manufacturer to reduce the motor output by 20:1. These motors were used together with a DC inverter manufactured by the same supplier, as further discussed in **Section 6.**

The gearbox output shaft on most servo gearboxes is not capable of reacting the 220 Nm moment from the wheel and ski, and thus a strain isolation bearing was needed. Based on a crawler lifetime of 2 years, a 3205-A2RS1 double-row angular-contact bearing from SKF was found to be capable, and was thus integrated within the motor-gearbox assembly. Two retaining rings provide axial retention of the bearing, each rated in excess of 15 kN, far beyond the expected 1.3 kN of axial bearing load. The margins of safety for the bearing, taken dynamically (the cycle count is within an order of magnitude of 10 million) is seen in **Equation 12,** where the normal reaction force on each bearing race from the contact patch loads is found in **Equation 11**. Note the dependence on both the position of the bearing relative to the contact patch, y_{con}, and effective length between the bearing pressure points, L_{bear}. Other variable definitions can be found in **Appendix 11.1**.

$$F_{react} = 4,961\ N = \frac{1}{NL_{bear}}(y_{con} F_N + y_{ski} F_{mag} + \frac{D}{2} F_{drag} + \frac{1}{2} F_N) \quad (11)$$

$$MoS_{bearing} = 0.34 = \frac{NC_{10}}{FoS \cdot F_{react}} - 1 \quad (12)$$

Likewise, the margin of safety for the retaining ring is shown in **Equation 13**, based on the rating of the ring and the frictional load reacted by each wheel.

$$MoS_{ring} = 18.4 = \frac{NF_{rating}}{FoS \cdot F_{drag}} - 1 \quad (13)$$

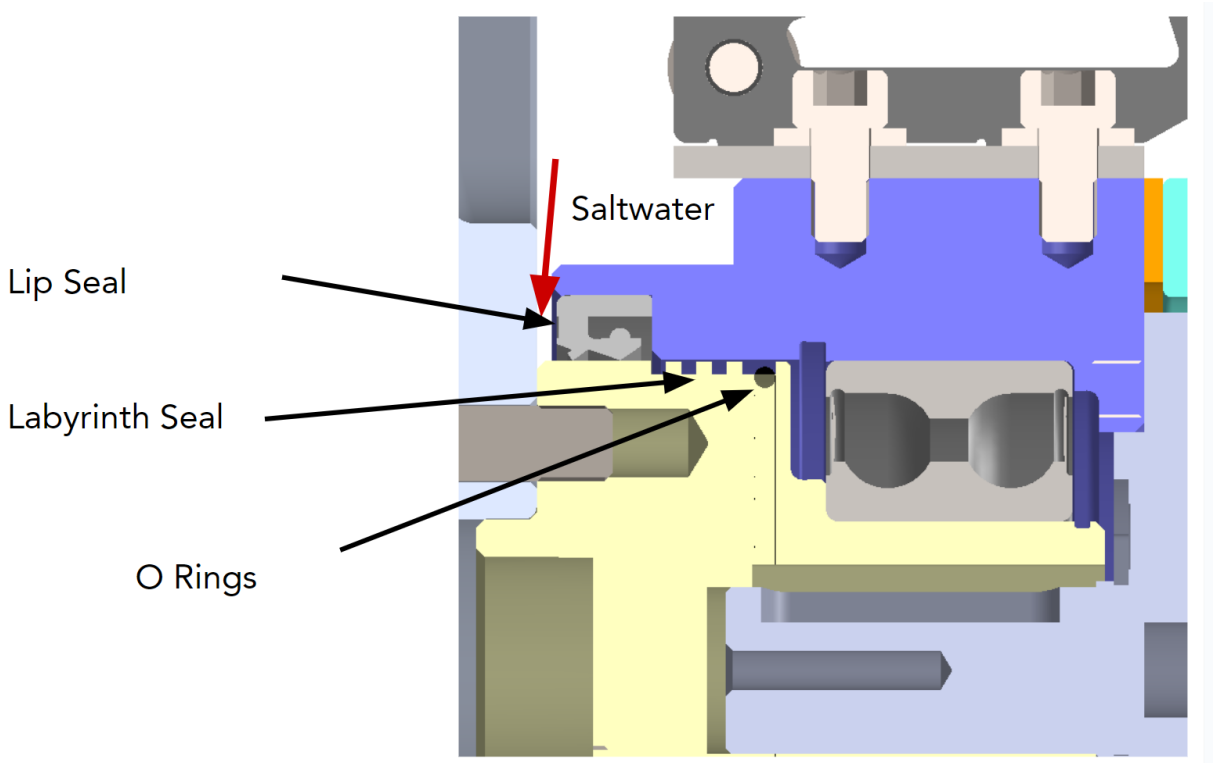

Figure 27. Cross section of the motor assembly outer seal. Note the teeth of the labyrinth seal, together with the o-ring groove are integrated into the wheel hub to form a rotating seal. Additionally, the two races of the double-row angular contact bearing used can be clearly seen. The enclosed volume, shown here as the region to the right of the o-ring is filled with oil for electrical insulation.

To seal the motor and bearing from saltwater, and thus prevent their rapid destruction via corrosion, the motor and gearbox are placed within a static sealed housing, assembled directly to the bearing housing, as shown in **Figure 27**. This housing will be filled with a transformer oil, providing both lubrication and electrical insulation against potential seawater-induced short circuits. The wheel hub is integrated with the seals via a monolithic component, with a 5mm stainless steel key providing torque transfer from the gearbox. The bearing housing, doubling as the upright, contains a step-down near the wheel hub for mass savings. The final challenge of the motor assembly is the creation of a rotating contact joint, a problem exacerbated by the highly corrodible nature of commercial motors. The foremost defense to seawater ingress is a lip seal, followed by a contacting O-ring on the inner end, and between which a straight labyrinth seal arrangement is constructed to increase the fluid mean path. For the gap size chosen, and ignoring the teeth of the labyrinth, a flow no higher than 3 g/hr is expected. Combined with the O-rings and the lip seal, a functional but low friction rotating seal has been accomplished.

3.3 Fabricated Prototype

3.3.1 Overview

Fabrication of the prototype was accomplished almost entirely through outsourcing to external vendors, and then assembly done through MIT campus resources. The specified fits and tolerances worked well, and the prototype is ready for further testing.

3.3.2 Sourcing

Most of the wheel assembly machined components were fabricated by a local Massachusetts machine shop in the hopes of easing production communication. While the quality of parts produced was high, the vendor slipped repeatedly on the timeline, and care should be taken in future to ensure sufficient time is available for local sourcing.

The sheet metal parts for the suspension joint mounts were fabricated overseas by Xometry, with overal decent quality but with the fixturin tabs left on, requiring post processing and grinding work to complete. Nevertheless, they came in on time and only required grinding and reaming to size.

Bearing and bushing sourcing was more problematic - while the angular contact bearings were easy to source, multiple vendors failed to ship the suspension bushings, and the needle bearings for the skis have yet to arrive as of the writing of this paper.

3.3.3 Learnings

Key conclusions from the fabrication and assembly process are to order components as early as possible, to avoid dangerous schedule slippage, and to re-use components wherever possible. In particular, it was noticed during assembly that the upper and lower control arms could have been made identical, reducing component count.The poka-yoke tabs, where tab patterns were slightly offset on one end to prevent incorrect assembly worked well, avoiding assembly errors during fixturing prior to welding.

4. Chassis Subsystem

To assemble all of these subsystems into a complete system, a chassis was designed. The chassis serves as a structural frame to mount the cleaning, suspension/drivetrain, and hydropackage subsystems. As on board navigation and electronics were de-scoped for this semester, the chassis was not designed to house electronics. The current chassis design is by no means an optimized design but rather serves as the first prototype build. The purpose of this design is to form the structural frame onto which all the other subsystems (cleaning, hydrodynamic shell and drive train) could be mounted onto and resist the predicted loading conditions experienced during system level testing in the future.

4.1 Functional Requirements

Table 9 lists the functional requirements for the chassis subsystem. The system's main goal is to link all of the subsystems together and to provide the strength needed to maintain the crawler's structural integrity.

Table 8. Chassis subsystem functional requirements

Functional Requirement	Target Value	Source	Verification
Brush Normal Force	75 N	Cleaning	Brush Testing
Brush Frictional Force	22.5 N	Cleaning	Brush Testing
Drag Force	4,230 N	HydroPackage	CFD/Drag Calculations
Chassis Size	750 mm X 750 mm X 254 mm	Design Criteria	N/A
Chassis Weight Support	80 kg	Design Criteria	N/A
Hydrostatic Pressure	1-2.6 atm	Design Criteria	N/A
Brush Drag Torsion Loads	105.3 Nm	Drag Forces	Analysis/Testing
Moment Couple (Rocker/Lower Control Arm/Push Rod	215 Nm	Suspension	Analysis/Testing
Shock Force (Suspension)	400 N	Suspension	Analysis/Testing
Suspension Upper Arm Force	-1724 N	Suspension	Analysis/Testing
Suspension Lower Arm Force	1484 N	Suspension	Analysis/Testing
Deflection/Stiffness Brush Joints	0.39 kN/mm	Cleaning	Analysis/Testing
Temperature Variance	4-30 C	Design Criteria	N/A
Ground Clearance	50 mm	Design Criteria	N/A

4.2 Chassis Design

4.2.1 Overview

The final design of the chassis component is shown below in Figure 28

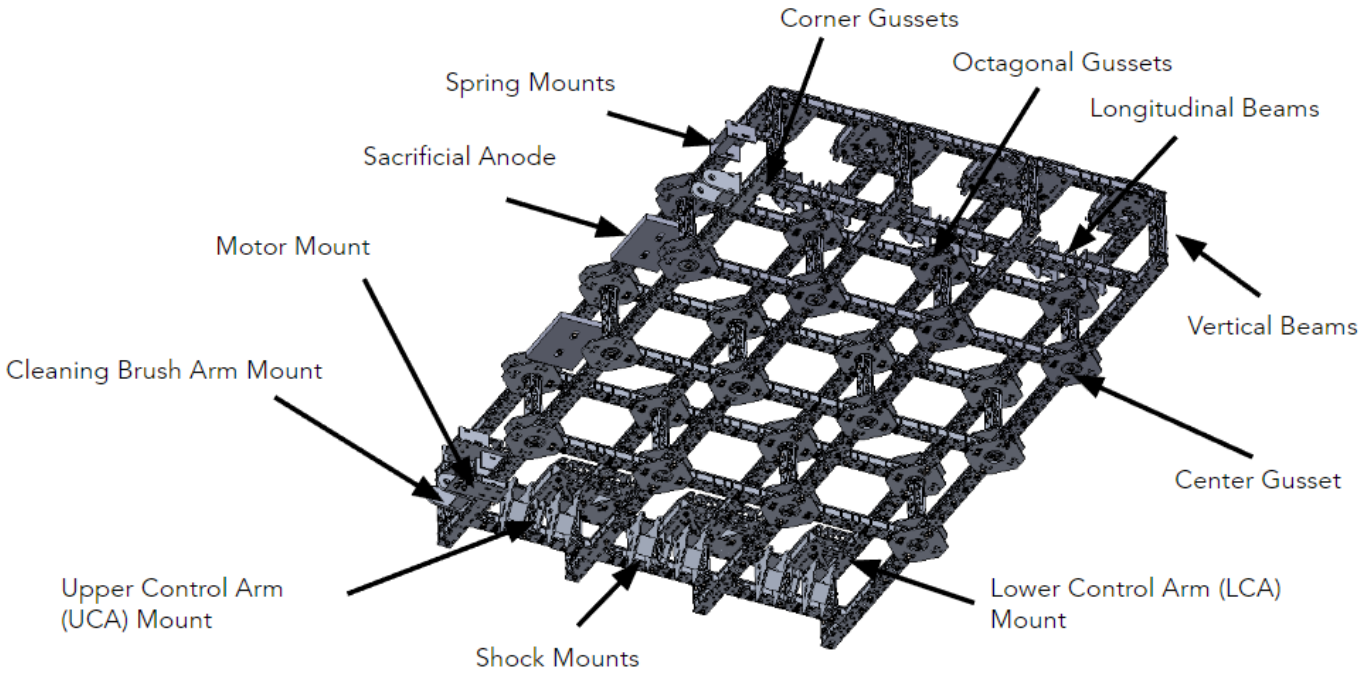

Figure 28 Overview of Final Chassis Design

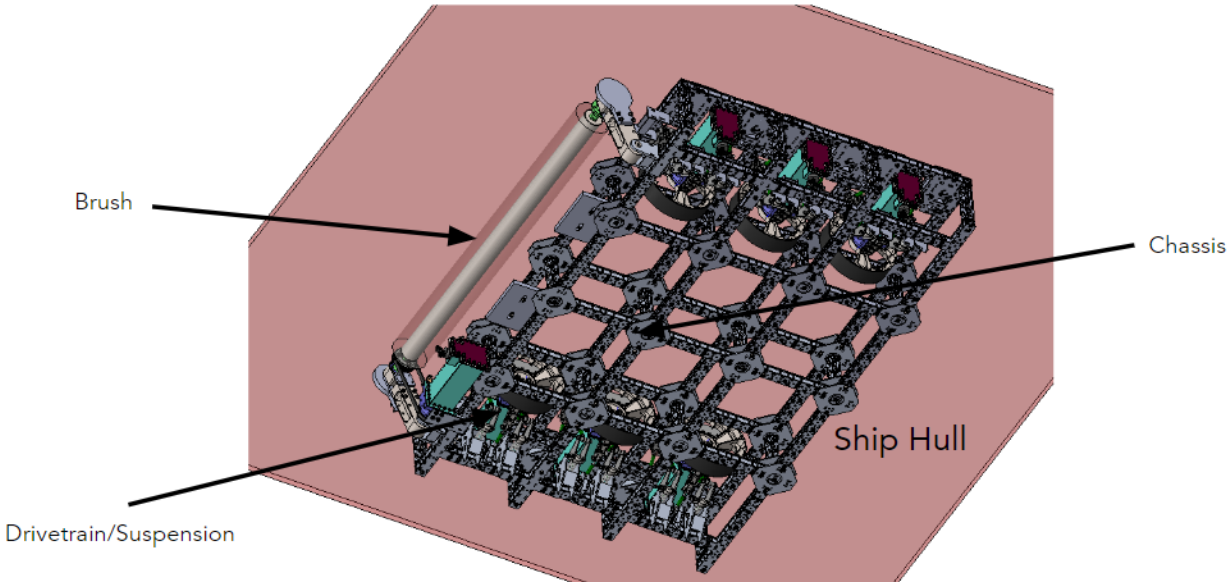

Figure 29. Chassis Integrated with other Subsystems

The final design arrived at this point after multiple iterations. The process started with first principles methodology of construction of free body diagrams of the primary loads imparted on the chassis. This is summarized in figure 30.

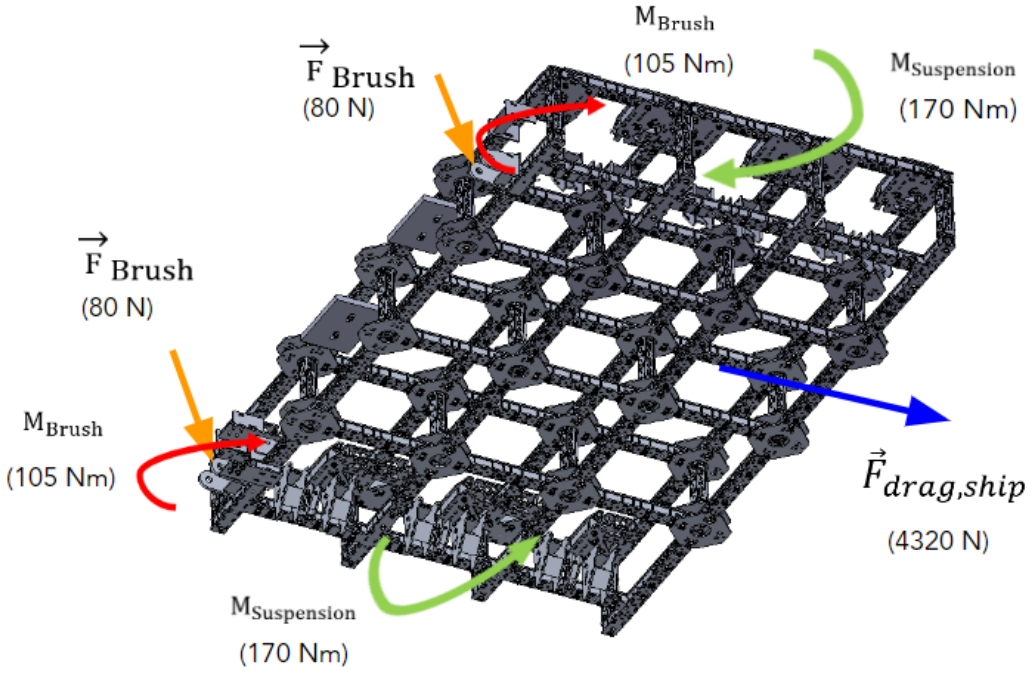

Figure 30. Chassis Free Body Diagram

Due to the non-linear nature of the structure, a finite element study (modal study) was conducted on the longitudinal beam structure (using bonded connections) to obtain eigenvalue frequencies that will serve as basis for future work on vibration analysis.

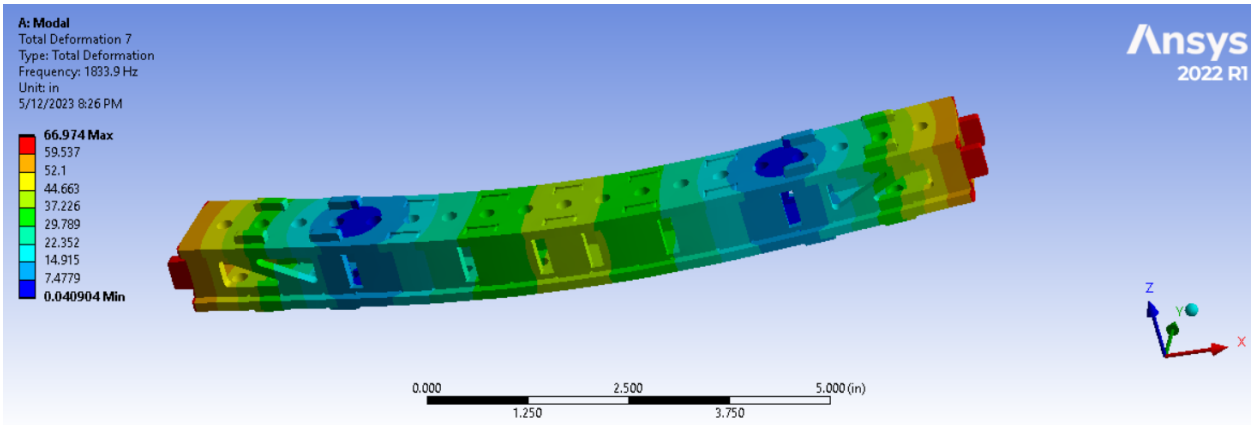

Figure 31. Modal Shape of Longitudinal Beam Kit (1833.9 Hz)

	Mode	Frequency [Hz]
1	1.	0.
2	2.	0.
3	3.	9.9974e-003
4	4.	2.576e-002
5	5.	58.79
6	6.	294.12
7	7.	1833.9
8	8.	1849.5
9	9.	3164.9
10	10.	4125.
11	11.	4520.2
12	12.	6207.3
13	13.	6963.6
14	14.	7586.1
15	15.	7885.7
16	16.	7929.1
17	17.	8097.9
18	18.	8851.7
19	19.	8904.9
20	20.	9831.2

Figure 32. Modal Frequencies of Longitudinal Beam Kit (First 20 modes)

The chassis beam kits are primarily made up of box tubes, whcih have been bolted together from 2D top and side plates that are 0.125” thick. The reasoning behind the box tube structure is the high strength to weight ratio it provides due to high second moment of inertia. The close loop (as opposed to an I-beam) also allows the box tube beams to provide great torsional stiffness. The second moment of inertia of the box tubes were calculated as shown below,

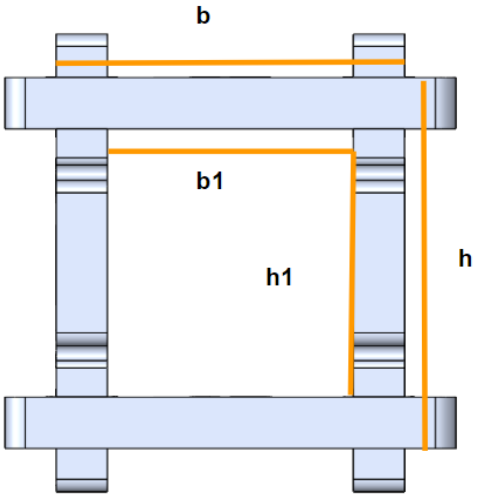

Figure 33. Longitudinal Beam Box Tube Cross Section

$$I_x = \frac{bh^3 - b_1 h_1^3}{12} \tag{14}$$

Using **Equation 14,** $I_x = 0.031\ in^4$ value can be utilized to define beam element stiffness for full scale structural analysis in the future.

4.2.2 Tab/Slot Construction Design

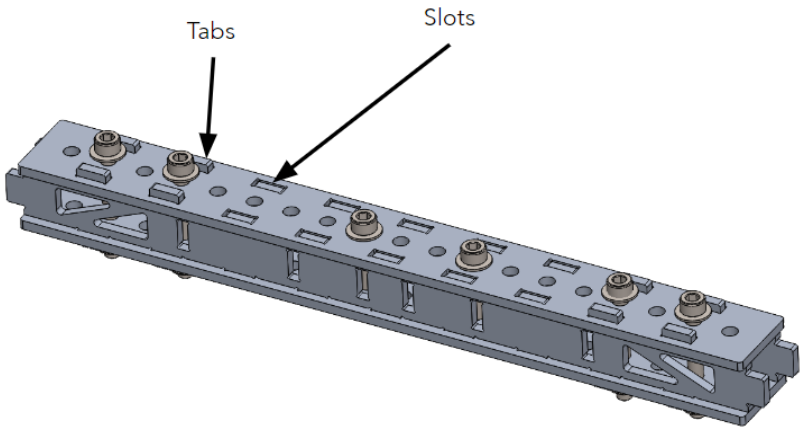

Figure 34. Longitudinal Beam Kit

The adoption of tab/slot connection method was adopted early in the design cycle as it was determined to be the best construction method given our limited resources and timeline. Tab and slots are great load carrying and locating features. Furthermore, it allows 0.125” thick flat sheet metal to be used to construct entire structural elements. In addition, this design allows the use of Omax water jetting, which is capable of producing a part to part profile tolerance of ±0.001” (0.0254 mm). Such precise tolerances at the piece part level minimizes the tolerance stackup during assembly, eliminates need for any complicated CNC machining/fixturing and enables quick manufacturing in batches that can be easily assembled using preloaded bolts, washers and nuts.

One of the concerns regarding slot/tab construction is the failure mode of the side plates due to preloading of the 10-32 bolts. This failure mode is predicted to be a combination of compressive yielding and buckling. If the cross section of one of the beam kits (longitudinal beam kit was utilized in this analysis) is taken, the following figure shows the breakdown of the main components.

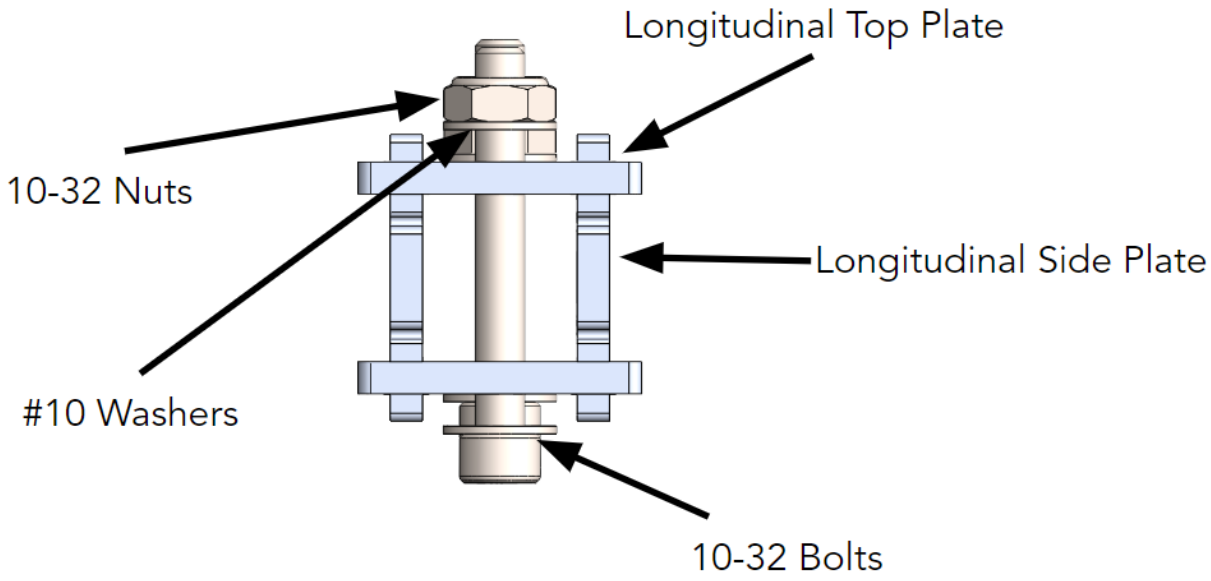

Figure 35. Longitudinal Beam Kit Cross Section (10-32 Preloaded Bolt)

Under bolt preloaded condition, the free body diagram of the longitudinal side plates can be represented by the following figure,

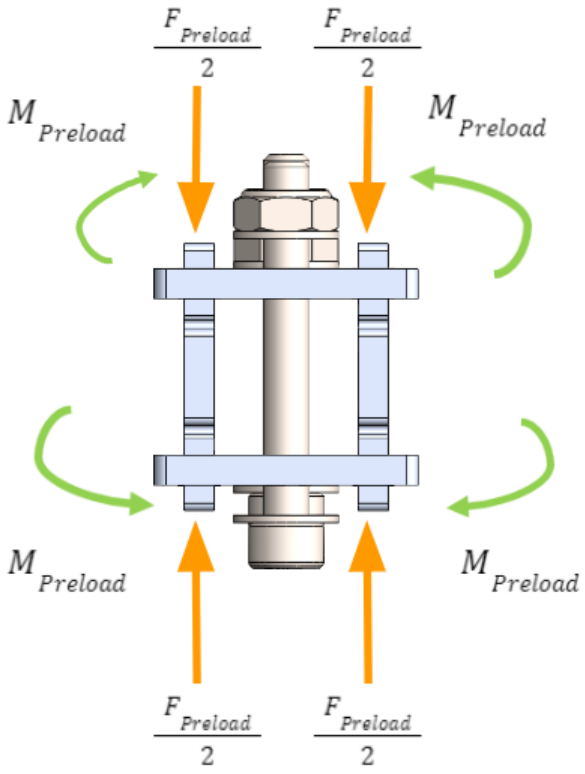

Figure 36. Longitudinal Beam Kit Free Body Diagram (Preloaded Bolt)

One of the dimensionless parameters utilized in buckling analysis is the slenderness ratio (r/L) which indicates the degree to which the Euler buckling model is valid. Since the calculated slenderness ratio for the beams is 14.6, it is a significant indication that the primary failure mode due to pre-loaded bolt force is due to compressive yield relative to buckling. Nevertheless, high level first order analysis was conducted using the Johnson buckling model which is shown in **Equation 15**.

$$\sigma_{Johnson\ CR} = \frac{P_{cr}}{A} = S_y - \left(\frac{S_y KL}{2\pi r}\right)^2 \left(\frac{1}{E}\right) \quad (15)$$

Secant Buckling (Eccentric Buckling) is another failure mode present due to the eccentric nature of the preloaded force on the beam side plate, leading to a bending moment couple in addition to the preload force. This results in the maximum stress in the inner fiber of the side beam plate that is a combination of bending and compression as shown by Equation **16**.

$$\sigma_{c,max} = \frac{P_{cr}}{A}\left(1 + \frac{ec}{r^2} sec\left(\frac{KL}{2r}\sqrt{\frac{P}{AE}}\right)\right) \quad (16)$$

Using 85% of yield strength of 316 Stainless Steel 10-32 Bolt, a maximum of 1693 N can be applied as the preload force.

Table 9. Johnson and Eccentric Buckling Margin of Safety (M.O.S)

Parameter	Value
Yield Allowable (Sy) of 5052-H32	193 MPa
Slenderness Ratio	14.6
Max Preload Force (10-32 Bolt)	1693 N
Eccentricity Offset (e)	13.97 mm (0.55″)
Johnson Critical Load (derived from $\sigma_{Johnson\ CR}$)	17904 N
M.O.S Johnson Buckling	6
Eccentric Critical Compressive Critical Load (derived from $\sigma_{c,max}$)	2337 N
M.O.S Eccentric Loading	-0.03

The conclusion from the analysis is the margin of safety for Johnson buckling is well above 1, and as predicted initially from a slenderness ratio of 14.6, buckling failure mode is not a concern. On the other hand, there are chances of failure due to yielding due to compressive and bending loads due to the eccentric nature of the preloaded bolt force as the margin of safety is near 0. There are two options that could improve margin of safety, one of which is to lessen the preload form 85%. On the other hand, further detailed analysis and testing is needed to confirm or reject this as a valid concern.

4.2.3 Material Selection

The primary material for chassis construction was initially chosen to be 316 Stainless Steel mainly due to high allowables (Yield and Ultimate Tensile Strength) and due to the presence of 2-3% Molybdenum which results in great corrosion resistant properties in salt water.

But as the chassis was further developed and loading conditions from other subsystems had been finalized, the strength requirements especially in constraining moments, shear and parallelogram ing resulted in addition of gussets, vertical columns and bolted joints. Welded joints have been minimized in this prototype to close the gap on schedule slips. This resulted in more than 3X the target weight of 10 kg that had been specified in the functional requirements. As a result, the Aluminum 5052-H32 was chosen as the final material as the strength to weight ratio is nearly 1.5 times as much. This resulted in weight reduction from ## kg to ## kg. Although this didn't quite meet the weight target specified in table 9, this change in material resulted in a much lighter chassis that could be optimized for mass in future design iterations. Furthermore, 5052-H32 also has a combination of desirable properties for our use case such as great weldability, high corrosion resistance and relatively high yield and ultimate strengths at annealed conditions post welding. Changing the chassis from 316 SS to Al 5052 H32 introduced concerns regarding galvanic corrosion, pitting corrosion and stress corrosion cracking especially near 316 SS and Al 5052 interfaces (bolted joints). For this prototype, the primary focus was on tackling the galvanic corrosion issue by using Magnesium sacrificial anodes. As Magnesium is much more electronegative relative to Aluminum alloys as depicted in figure 37. Magnesium was chosen as the sacrificial anode.

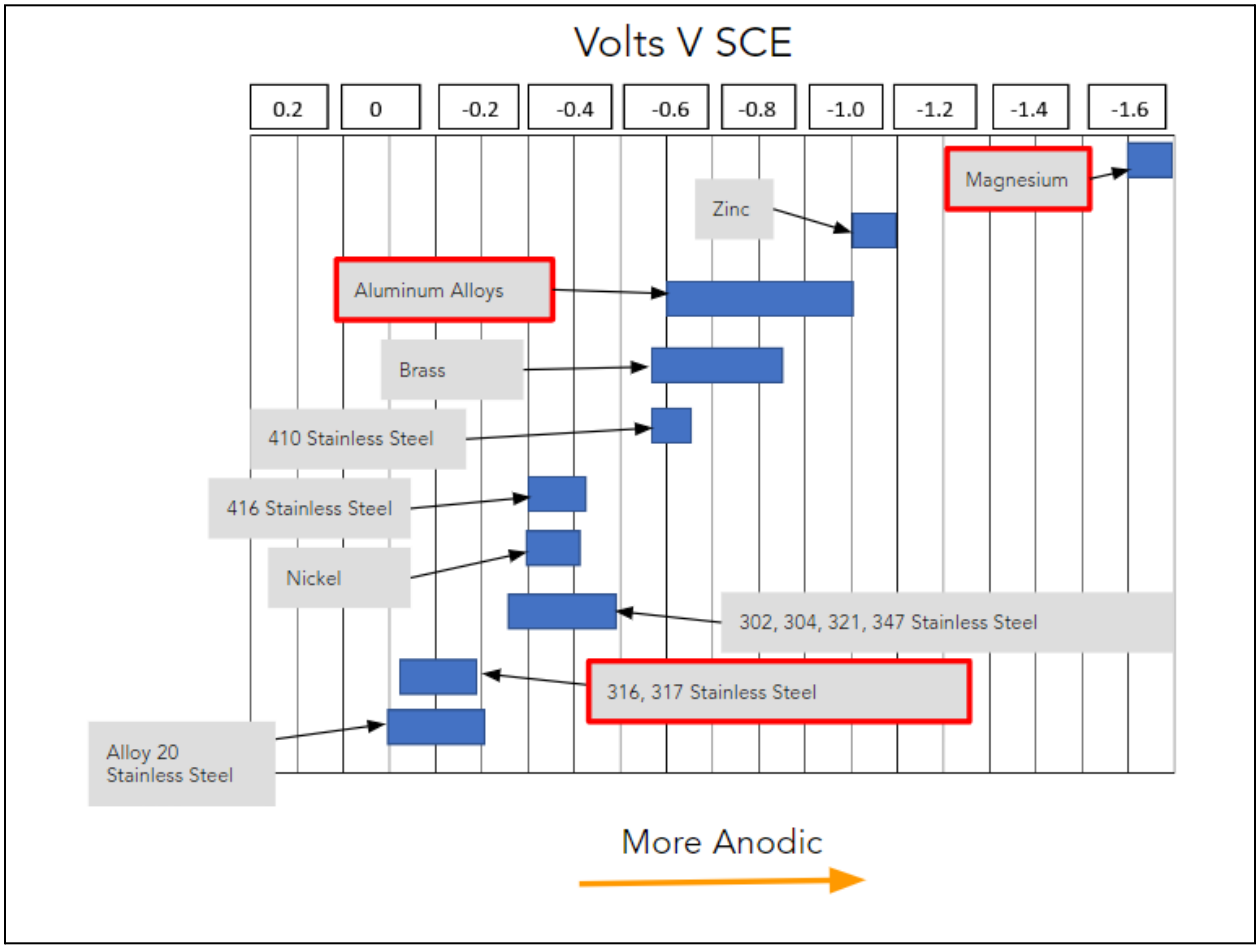

Figure 37. Electronegativity Chart

Even though magnesium is not the optimum sacrificial anode for salt water applications as it will very quickly react, it was determined that the initial prototype was sensitive to this since the primary function of this prototype is to test key novel systems (drivetrain and cleaning subsystems).

4.2.4 Suspension and Shock Mounts

The suspension mounts are needed to mount the Upper Control Arms (UCA) and Lower Control Arms (LCA) and the shock mounts are needed to mount the shock absorbers and rocker plates.

The mounts were designed to act as two force members with minimal moment carrying capability. This is because the suspension and shock mounts interfaces with the UCA, LCA, shocks and the rocker plates which are mostly two force members and impart minimal moment in out of plane direction. The mounts are connected to the longitudinal beam kits using TIG (Tungsten Intern Gas) welding. The weld locations and sizes are summarized in the following figure.

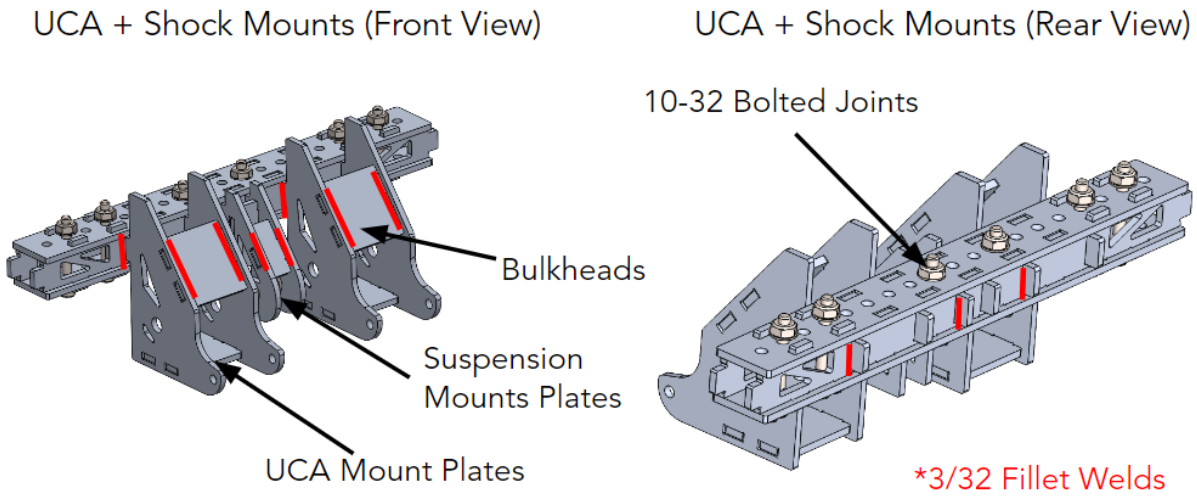

Figure 38. Upper Control Arm and Shock Suspension Welds

To minimize the number of analyses needed in order to size the welds, the component with the highest two force loads (UCA Mounts) was chosen as subject of the analysis. The force imparted on the UCA from the push rods are shown below.

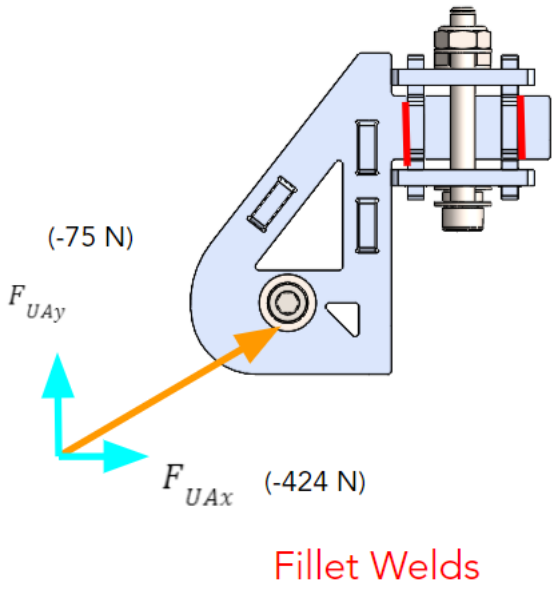

Figure 39. Upper Control Arm and Shock Suspension Welds Free Body Diagram

The suspension mount can be modeled as a cantilever beam.

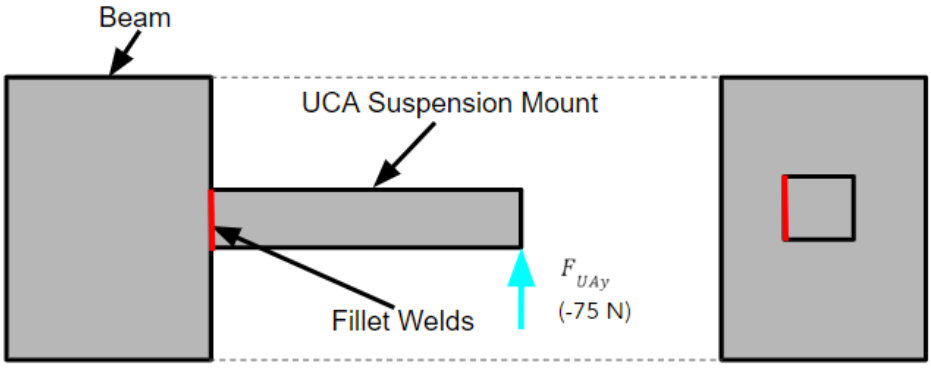

Figure 40. Upper Control Arm Weld Line Representation (Y-forces)

As a result, the forces from the pushrods result in two primary types of stress experienced by the fillet welds. The first type of stress is the primary shear (F_{UAy}) which can be modeled as shown in **Equation 17**.

$$\tau_{primary} = \frac{V}{A_{Throat}} \quad (17)$$

The second type of stress is bending (tension/compression) caused due to the moment that is resulting from eccentric nature of the force vectors (F_{UAy} and F_{UAx}) that can be shown using **Equation 18** and **Equation 19**.

$$\tau_{nominal\ throat} = \frac{Mc}{I} \quad (18)$$

$$\tau_{total} = \left(\tau_{primary}^{2} + \tau_{nominal\ throat}^{2}\right)^{0.5} \quad (19)$$

Alternatively, the weld can also be modeled as the lap joint experiencing axial loading (primarily from F_{UAx}.

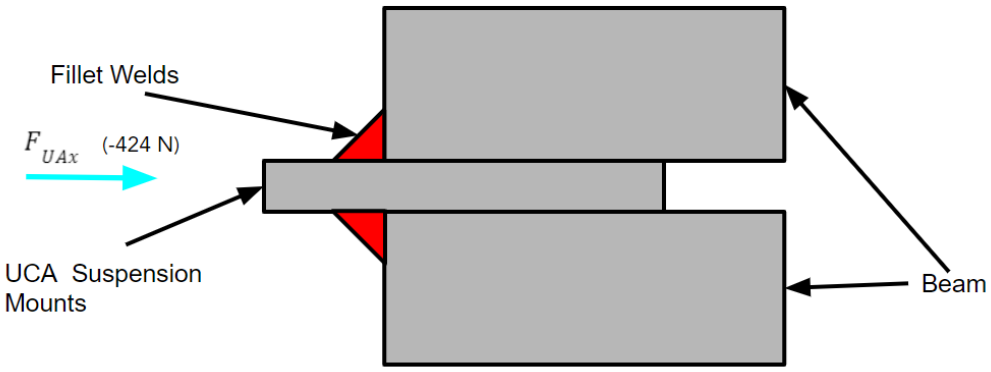

Figure 41. Upper Control Arm Weld Line Representation (X-forces)

The stress experienced by the throat area of the fillet welds are a combination of tensile and shear stresses that can most usefully be represented by the Von Mises Stress as shown in **Equation 20**.

$$\sigma_{VM} = (\sigma^2 + 3\tau^2)^{\frac{1}{2}} = \frac{F}{hl}\left((cos^2(\theta) + sin(\theta)cos(\theta))^2 + 3(sin^2(\theta) + sin(\theta)cos(\theta))^2\right)^{\frac{1}{2}} \quad (20)$$

It can be shown that the largest σ_{VM} occurs at $\theta = 62.5^{\circ}$, and therefore, σ_{VM} can be simplified as shown in **Equation 21**.

$$\sigma_{VM} = 2.16\frac{F}{hl} \quad (21)$$

Von Mises is an accurate representation of the deviatoric stresses that result in yielding and therefore resulting in ultimately cracking of the weld. The margin of safety (MOS) for each of the models are summarized below for 3/32 fillet weld.

Table 10. Upper Control Arm (UCA) Suspension Weld Sizing

Parameter	Value
Yield Allowable (Sy) of 5052-O	90 MPa
Shear Strength Allowable (Syy) of 5052-O	45 MPa
Primary Shear	2.9 MPa
Nominal Throat Shear	26.8 MPa
Von Mises Stress	12.6 MPa
M.O.S Total Shear Yield (at Annealed condition) - τ_{total}	0.33
M.O.S VM Yield (at Annealed condition) -	4.68

4.2.5 Brush Cleaning Mounts

The primary function of the brush cleaning mounts is to provide a mechanical interface to mount the cleaning brush arm and to provide sufficient stiffness so the cleaning mechanism will not bind due to excessive compliance.

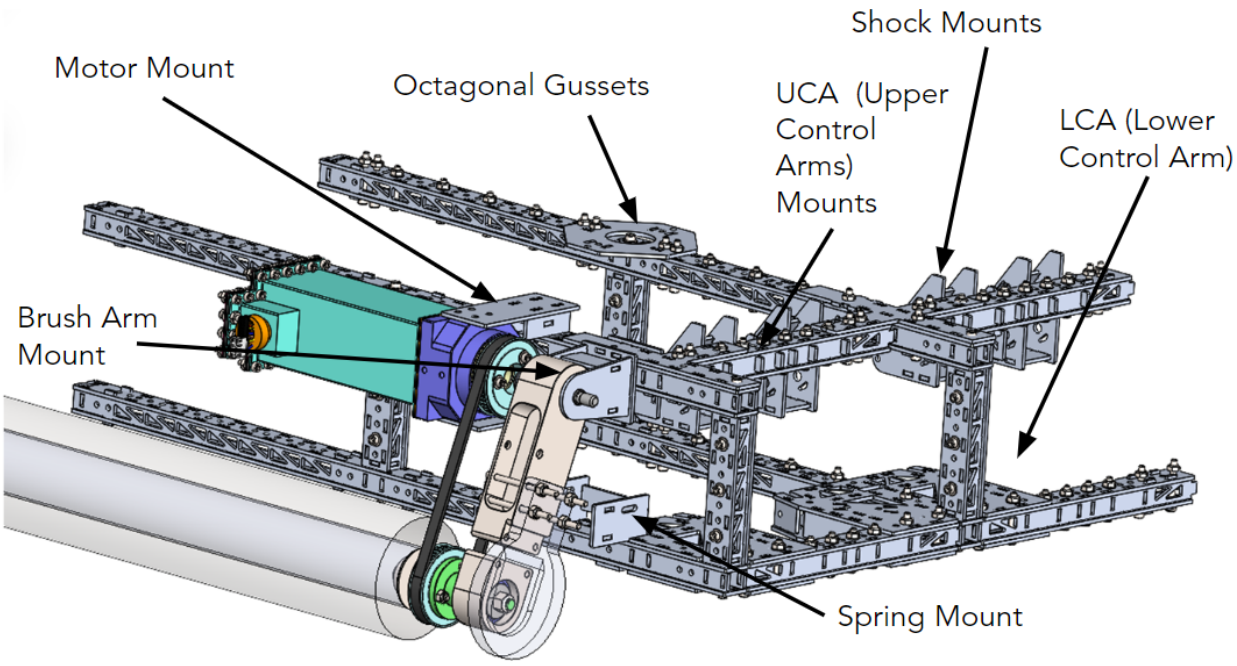

Figure 42. Brush Mount Design

A finite element study was run on the brush arm mount to determine the order of the stiffness and if there is any potential to yield due to primarily the moment caused on the brush arm due to the drag forces.

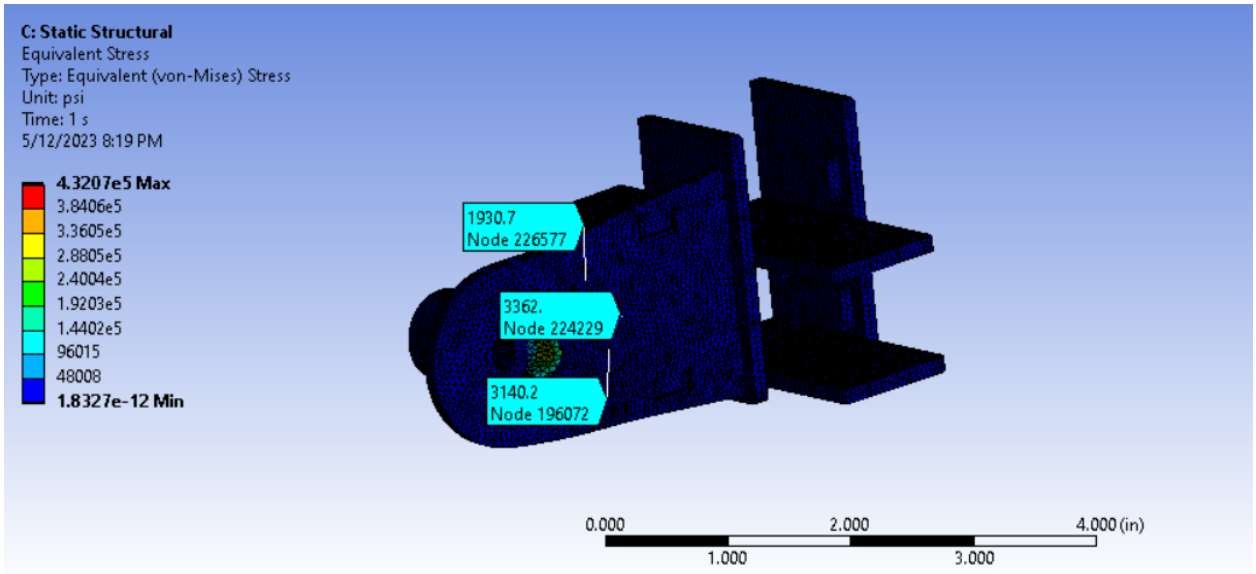

Figure 43. Brush Mount Von Mises Stress

Even though the maximum Von Mises stress is near 43 ksi, this is not accurate since the contact regions between the spacers and the brush arm mounting plate were simplified to be bonded. The excessive restriction on the deformation is not representative of reality and therefore led to artificial high stresses in that region. Nevertheless due to Saint Vernants principles, the stresses on the other regions of the brush mount are well below the allowable yield stress of 5052-H30 (28 ksi). The margin of safety for those regions is near 4.9. For future studies, contact regions between spacers and the various parts of the brush mounts must be setup accurately (with proper coefficient of friction) to represent accurate stresses near those areas. Figure 44 shows the maximum deformation of 0.005" (which in actuality maybe a little higher since the contact points are set as bonded). Nevertheless, an order of Margin of Safety can be obtained (using functional requirement of stiffness of 0.39 kN/mm; see Table 8) from the maximum deformation of 0.005" (0.12 mm). The margin is near 3.32 which provides sufficient evidence that the stiffness functional requirement from the brush arm has been satisfied, which allows the brush arms to clean efficiently without any binding.

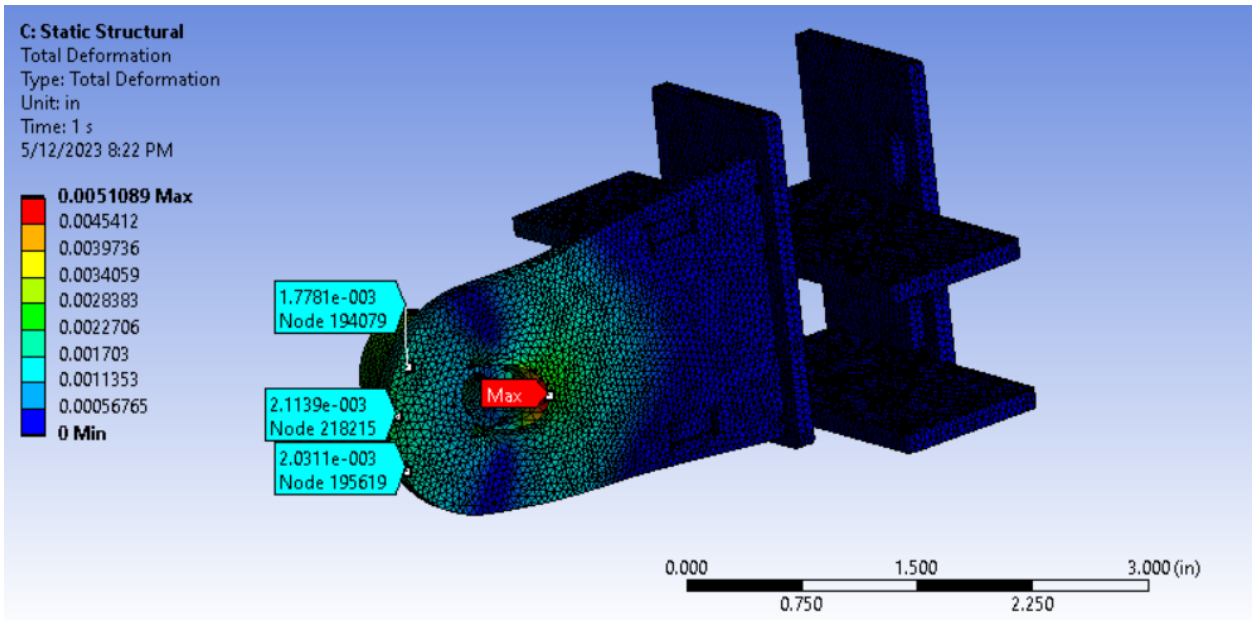

Figure 44. Total Deformation

4.2.6 Lower Control Arm Mounts

The Lower Control Arm (LCA) have been designed using primarily bolted joints. The main purpose of the LCA mounts is to mount the lower control arm rods to the chassis. Since welding has been removed from this mount, any major analysis was de-scoped for this sub-component.

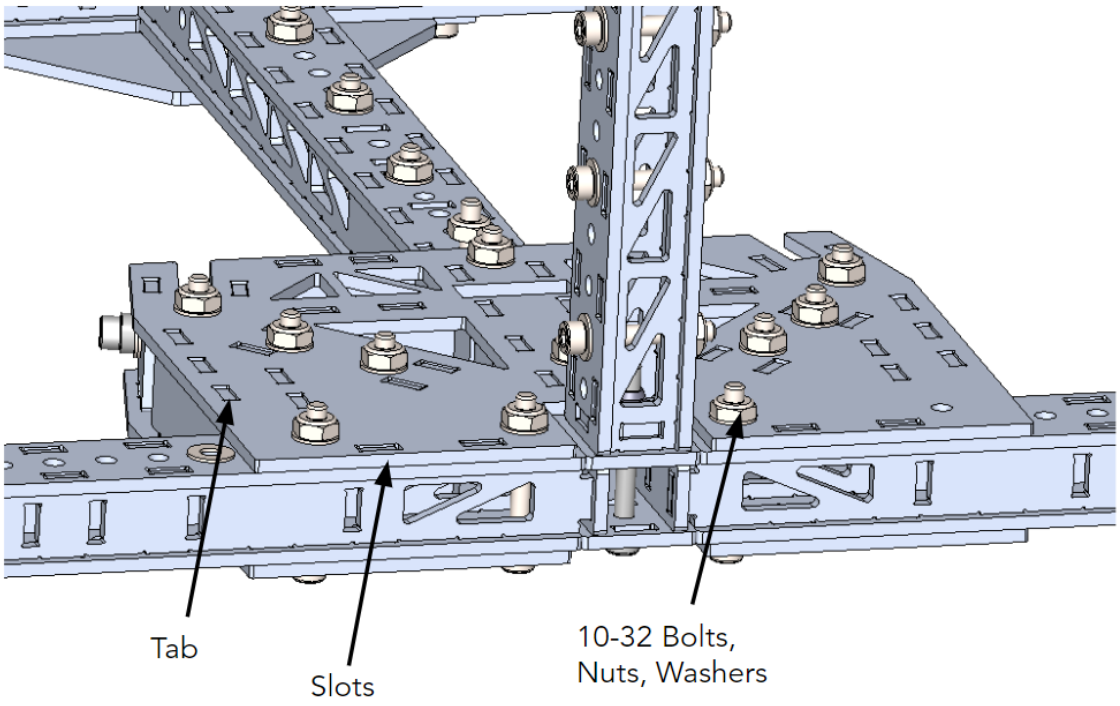

Figure 45. Lower Control Arm (LCA) Mounts

4.3 Fabricated Prototype

4.3.1 Overview

There are a total of 798 individual components that have been manufactured just for the chassis. Out of 798, 222 components had been manufactured in house (using waterjet and metal laser cutting techniques). The reasoning behind this strategy was to bring in the schedule associated with welding and also keep manufacturing costs low. The final prototype of the chassis integrated with the rest of the subteams are shown below,

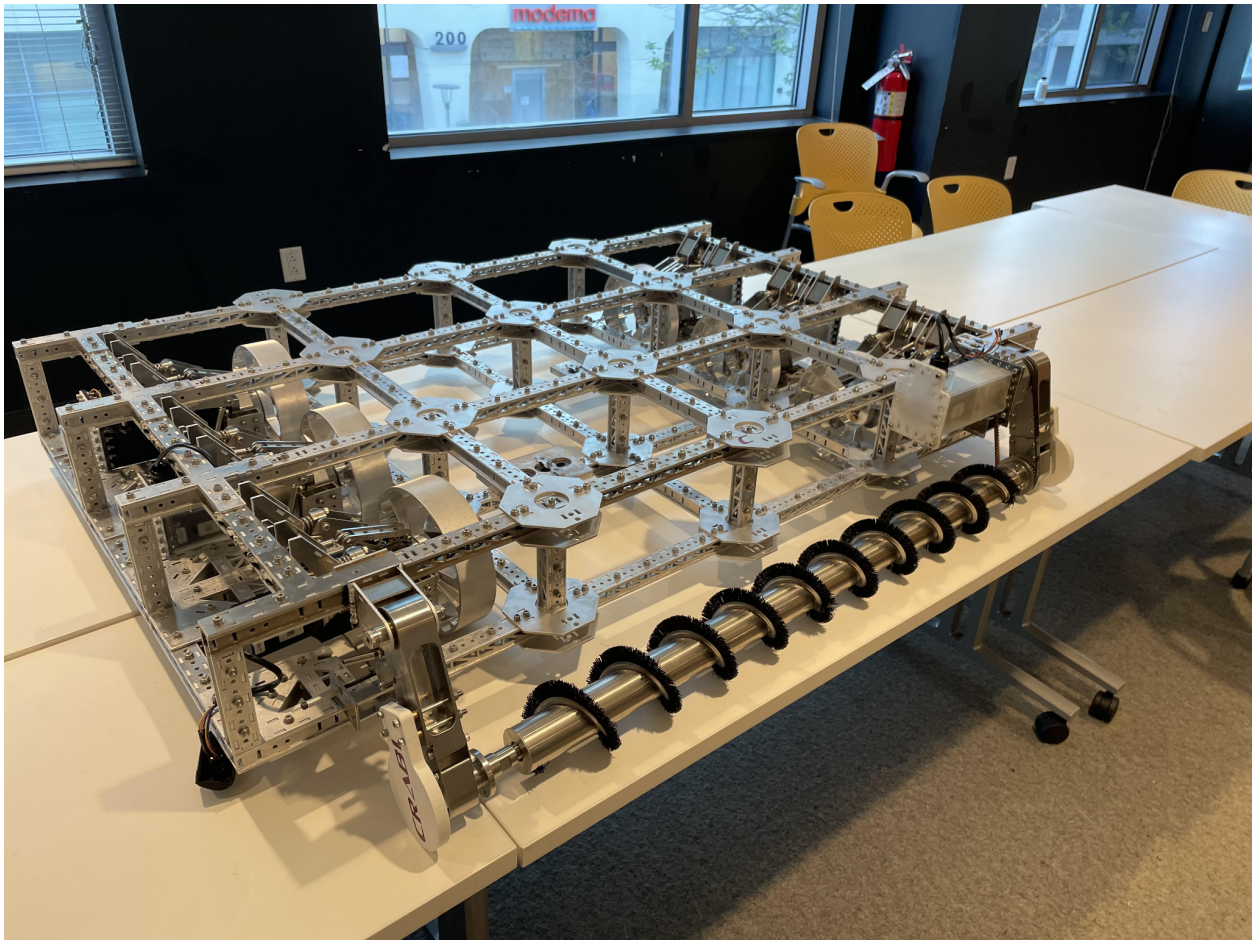

Figure 46. Fabricated Chassis Prototype (Integrated with other subsystems)

4.3.2 Sourcing

Out of 798 components, 576 components had been manufactured in China by Xometry. While there were some challenges in getting the parts through the U.S.borders and customs, these were quickly resolved with the help of Xometry and the parts had been delivered in time for final assembly.

4.3.3 Learnings

The main challenges in fabricating chassis has been schedule slips due to redesigning needed due to deficiencies of Solidworks in handling large assemblies. Symmetry, layout structures and configurations were heavily used in the second iteration of the chassis as it made Solidworks performance much better. In addition, there has been some communication gap as well between the chassis engineer and the team lead, in terms of how modeling should be done in Solidworks from the get go. Design schedule slip resulted in slips in schedule in fabrication of

the chassis and subsequent processes. Due to limited resources on campus, that is a lot of non-functional waterjet machines, it took about a week to manufacture 222 components. Since only about 1.5 weeks remained for welding, a lot of external vendors “no quoted” this job. As a result, the last ditch effort was to do the 5052 Aluminum welding in house during the last week.

5. Hydropackage Subsystem

The hydropackage shell is a rigid envelope designed to encompass all other subsystems. Its main goal is to streamline the crawler and reduce the drag from the flow of water induced by the motion of the parent vessel. Due to the need for the shell to generate minimal lift, the team used flow simulations to go through a series of design iterations discussed in section 5.2. Scale model tests were then performed on two of the designs to validate the predictions of CFD. Ultimately none of the designs were found to meet the functional requirements laid out for the subsystem, so no final design was selected. Section 5.4 includes recommendations for future work, including a description of a hydrofoil design with the potential to produce the necessary downforce.

5.1 Functional Requirements

Table 8 lists the functional requirements for the hydropackage subsystem. As mentioned in its introduction, the hydropackage’s main goal is to minimize the drag that the crawler will undergo to prevent any slippage, while covering enough volume to fit all of the subsystems underneath. The hydropackage should also avoid generating lift since additional lift would increase the downforce requirement of the attachment subsystem.

Table 11. Hydropackage subsystem functional requirements

Functional Requirement	Target Value	Source
Maximum CdA [Product of Drag coefficient (Cd) and Frontal area (A)]	0.07 m^2	System Global Requirements
Minimum Volume Covered	34” x 50” x 11”	System Global Requirements
Minimum ground clearance	50 mm	Suspension Parameters
Generate downforce	$\geq$ 0 N	Design Requirements

Symmetry	True	Driving Path
Maximum Flow Velocity	20 kn	System Global Requirements

5.2 Prototype Design Iterations

The first step of designing the hydropackage subsystem is to find a shape that meets our requirements. Given the uncommon conditions CRABI has to work under, conventional underwater systems design wouldn't fit, and conceptualization of designs that would perform well for CRABI has been realized. In this context, MIT Sea Grant specialist Dr. Andrew Bennett has been consulted to gather different ideas of what would work well in that environment and multiple concepts that could be used in the shell's designs.

In this part, the different hydropackage shell designs made will be presented, along with their respective advantages and disadvantages. Furthermore Computational Fluid Dynamics analysis (which will be referred to as CFD) that simulates the conditions CRABI would evolve in has been performed. This analysis allowed for quantitative analysis of these designs and a better understanding of the flow around the shell.

5.2.1 Crab Design

The first design made takes its roots in crab shells: their particularity is that they create downforce no matter what side the flow comes from, preventing crabs from being tossed around by underwater currents. Using this idea, a 'crab-like' shell would help the shell create the downforce sought for in the very turbulent environment there is on the side of a ship. Therefore, different crabs' shell shapes have been used and adapted into a hydropackage that would fit around CRABI, resulting in the following design:

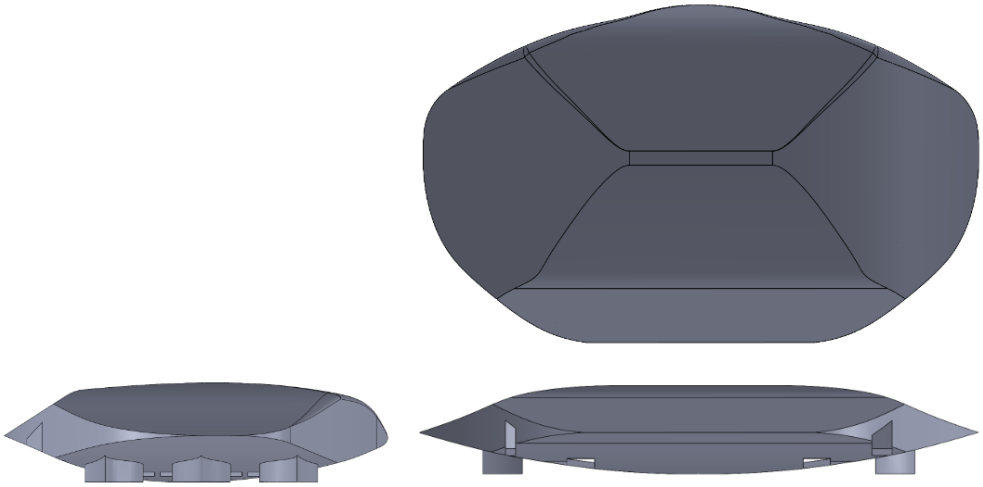

Figure 47: Orthographic Projection of the Crab Model. Gross structure is based on the curvature seen on crab species, adapted for the applicable CRABI geometry.

As it can be seen, cutouts have been made for the cleaning subsystem arms and the attachment and propulsion subsystem. Fenders have also been made next to each drive wheel to orient the flow around them, in order to optimize undercarriage flow. Indeed, one of the goals of this design is to direct part of the flow under CRABI to create a downforce through the Venturi effect. This idea is taken from racing vehicles that call it ground effect, where the airflow is used to pull the vehicle closer to the ground, whereas this design uses the sideway water flow to draw the crawler closer to the hull.

5.2.2 Expanded Flow Design

The expanded flow model attempts to iterate on the previous hydrodynamic package design by increasing the wheel distance, overall width of the shell and altering the shape and dimensions of the fenders. The goal of this design was to address the flow blockage problems encountered by the previous model (and explained in *part 5.2.4*) by providing larger channels for the water to flow through and hopefully inducing a greater downforce through the Venturi effect.

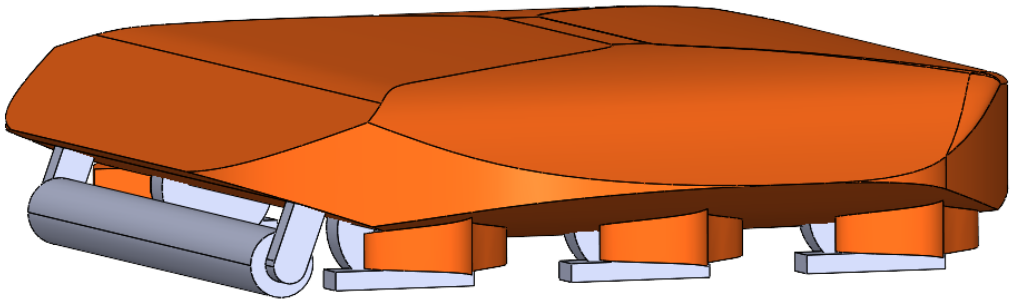

Figure 48: Simplified Model of the Expanded Flow Design used for CFD Simulation.

Although making CRABI longer, this solution wouldn't affect too much its performance as it has two main impacts: the larger projected area of the crawler would increase the drag force it experiences, but the increased undercarriage flow creates a higher downforce. As normal forces are directly created by the magnets and tangential forces are created by the wheels' friction on the hull (with a coefficient of friction of ~0.38), 1N of lift force needs 1N of added force from the magnets, whereas 1N of drag force needs 2.63N of added force from the magnets, making lift easier to compensate by increasing magnetic force.

5.2.3 Skirt Design

The following 'skirt model' is a completely redesigned hydropackage model. The design abandons the previous idea of inducing downforce on the vehicle thanks to the Venturi effect, and focuses on fitting a side skirt that extends to the surface of the hull and completely redirects the flow above the vehicle.

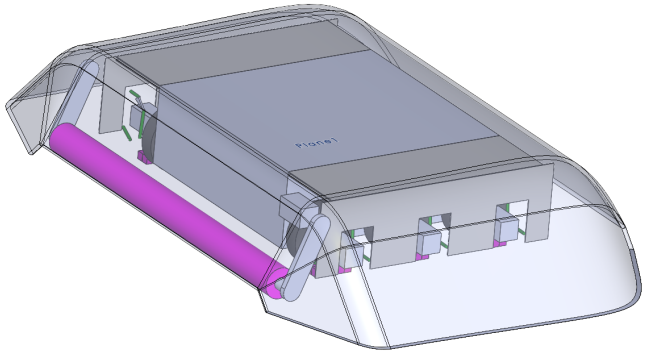

Figure 49: Isometric View of the Skirt Model

This design is a lot less streamlined than the previous ones and would therefore induce a lot more drag. But hopefully, the added downforce this design would create thanks to the flow pushing the crawler downwards will be enough to outweigh the added drag. This balance between added drag and increased downforce needs to be analyzed, keeping in mind that a factor of 0.38 makes downforce more advantageous than reduced drag.

The ground clearance requirement isn't met anymore, but this can be outweighed by different concepts around the skirt design. Making a bendable skirt would allow it to deform enough around bumps, but a balance in the stiffness has to be met to still keep its shape under the flow's pressure and not allow too much flow to go underneath the skirt and create undesired lift (this would correspond to a stiffness of approximately 204 N/cm).

5.3 Computational Fluid Dynamics (CFD) Simulation

Using these different designs made from qualitative analysis, CFD simulations have been carried out to verify if they would meet the functional requirements in lift and drag. To get these quantitative results, the team used *Ansys Fluent*, a common software used for fluid dynamics analysis. Full scale analysis was made to determine what the true performances of the shell would be under the real conditions. After setting up the models with the case parameters (v_{water}=10.3 m/s, $v_{crawler}$=1 m/s, P=222 kPa), the simulations were made to give us the following results under laminar flow (due to simulation limitations).

5.3.1 Crab Design

This design was simulated and analyzed in *Simcenter STAR-CCM+* (the only thing not done in *Ansys Fluent*, hence the different visuals) during the Fall 2022 semester. Furthermore, only the full scale model has been processed as we decided to not test the design given its poor performances.

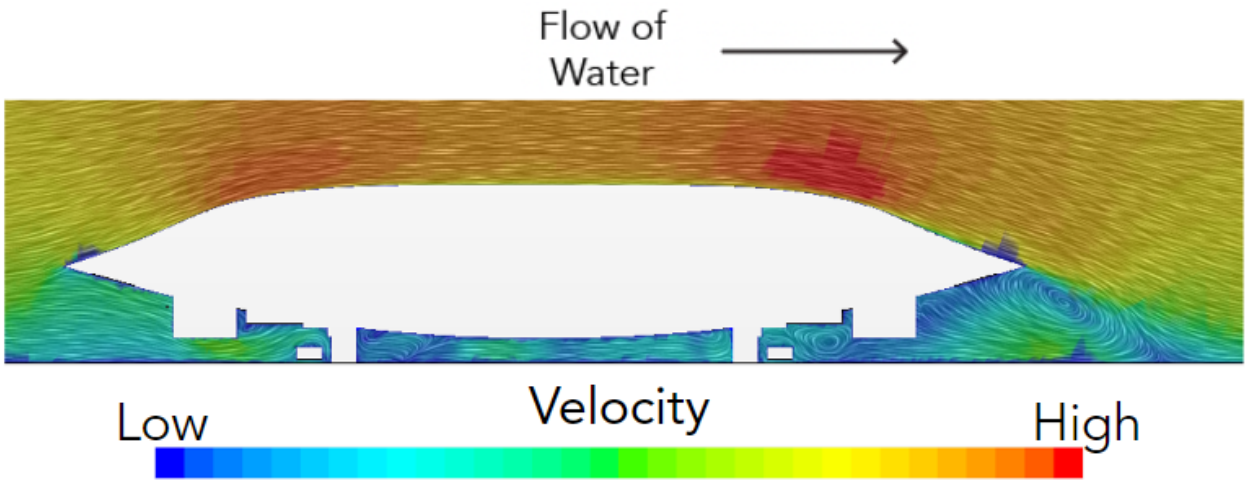

Figure 50. Vector field of the velocity around the integrated system. It can be seen that the flow is largely stopped once it reaches the wheels, an effect that the fenders were intended to mitigate. Without this undercarriage flow, the ground effect is lost, and so no downforce is present.

These results show that the integrated shell does not perform well. Indeed, not only is the CdA higher than our functional requirement, at 0.14 m², but there is also a substantial lift force of 20 kN. This design thus does not meet the requirements.

By analyzing the velocity vector field above, we can see that the wheels block most of the flow, even though some fenders have been implemented to direct the latter around those wheels. This flow blockage causes a pressure build-up under the leading edge of the shell and

pushes CRABI off the hull. Furthermore, the low velocity under the trailing edge of the shell creates a lot of turbulence and tries to make the whole system tip over.

5.3.2 Expanded Flow Design

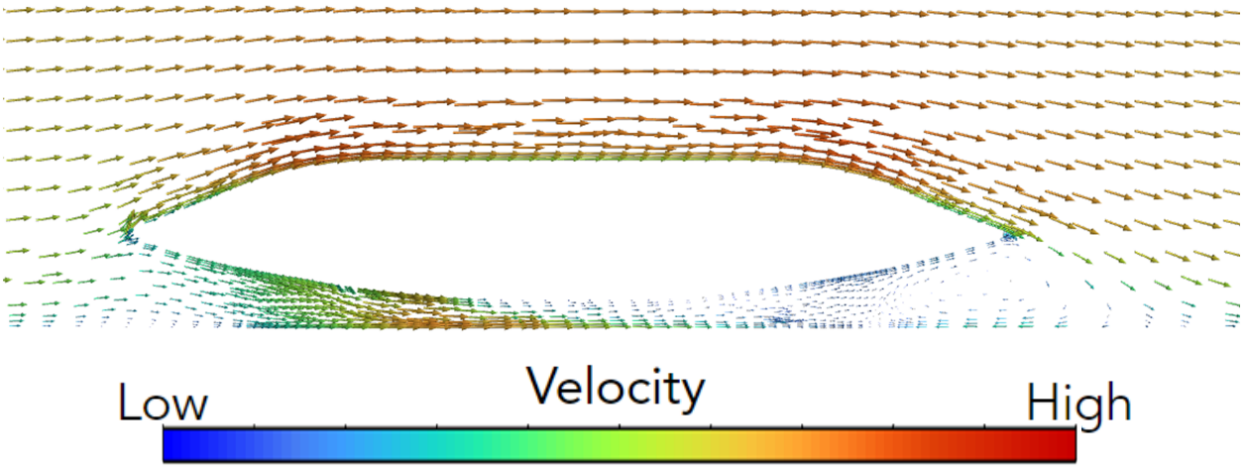

Figure 51. Vector field of the velocity around the expanded flow model. It can be seen that the flow is still largely stopped once it reaches the wheels, although the undercarriage channels have been expanded in order to better redirect the flow. Without this undercarriage flow, the ground effect is lost, and so no downforce is present.

Although the channels have been expanded to help with flow redirection under the shell, CFD shows that it is still stopped by the very low clearance there is under the shell's undercarriage and the hull. Outputting a lift force of 30kN and a CdA of 0.18m², the simulation says that this model still wouldn't work. As the width of the channels wouldn't help to be increased, another approach would be to increase the distance between the shell and the hull, but that would mean lifting all of CRABI up away from the hull, making it more difficult to control the drivetrain and increasing drag by uncovering more of the wheel assemblies.

5.3.3 Skirt Design

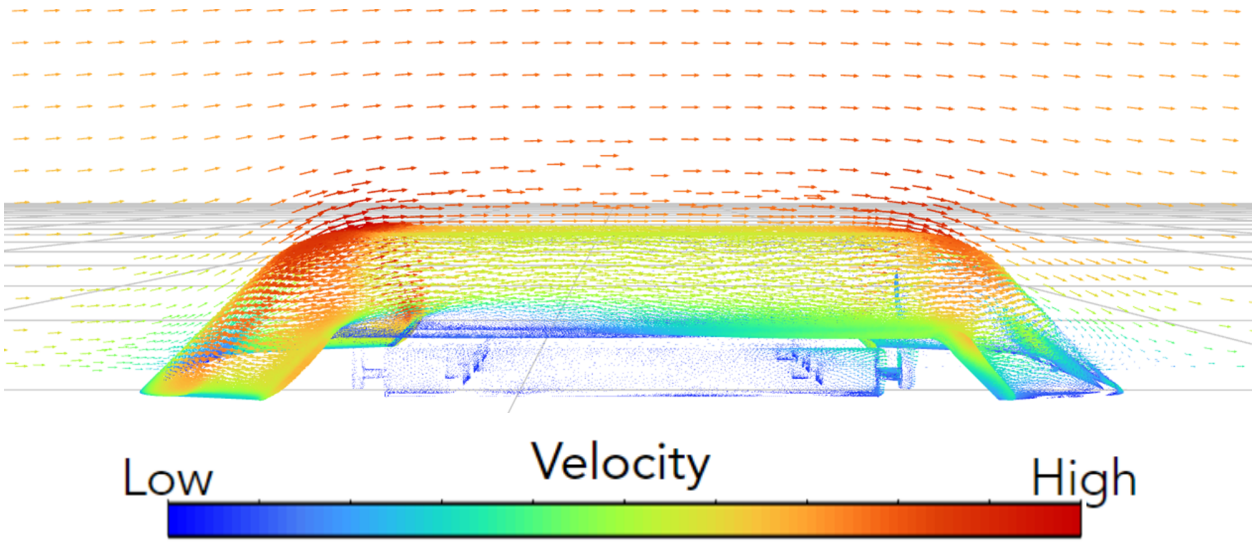

Figure 52. Vector field of the velocity around the skirt model. It can be seen that the flow is indeed redirected above CRABI and is nearly absent underneath. But we can notice the acceleration of the flow around the top corners, resulting in a Venturi effect 'sucking' CRABI off the hull.

With this model, the goal was to abandon the idea of Venturi effect and redirect all of the flow above CRABI. As can be seen in the velocity vector field, this has been achieved, but the reports say that we still have a lift of 3.5 kN and a CdA of 0.065 m². This is a significant improvement compared to the other two previous models, but the absence of lift we expected isn't present. We can assume that this is due to the acceleration of the flow around the corners of the shell due to the Venturi effect which is now 'sucking' CRABI off the hull instead of towards the hull.

5.4 Testing

Flow simulations like those performed on each of the hydropackage designs are a useful design tool for indicating the performance of a model. However, before CFD results could be confidently applied to the selection of a design for the full-size prototype, it was necessary to verify those results with a series of physical tests performed on scale models of each design. 1:3 scale models of both the expanded flow and skirt designs were fabricated, then towed in a tow tank so that lift and drag measurements could be taken. These measurements were then compared with, and found to confirm the results of initial CFD. The skirt model was found to experience **57.5 ± 8.9N** of drag and **30.5 ± 2.9N** of lift in testing. The expanded flow model experienced **67.8 ± 5.6N** of drag and **37.3 ± 1.9N** of lift. CFD for the full sized craft predicted **30 kN** of lift and **11 kN** of drag on the expanded flow model, and **6.5 kN** of lift with **3.5 kN** of drag Our results therefore indicate that initial CFD was accurate in predicting each model would

produce an unacceptable amount of lift, and that further design iteration is required to produce a functioning hydropackage.

5.4.1 Test Objectives and Design

In order to verify the findings of the flow simulations, physical tests were performed on scale models of each of the two designs. The goal of these tests was to take readings of the lift, drag and pressure on physical models in a tow tank and compare them directly to simulation results under the same conditions. In order for the results of physical testing to be as useful as possible, the tests were performed at a Reynolds number as close to that of the target conditions as possible and a fixture was designed to facilitate testing and mimic the hydrodynamic effects of a ship's hull. Furthermore, pressure sensors were placed at important points along the exterior of each model so that the pressure map observed in the CFD simulations could be verified, in addition to the lift and drag estimates. The tests were performed in the intelligent tow tank in MIT Sea Grant's facilities.

For the physical test results to be instantly applicable to a full-size crawler attached to a ship traveling at 20 knots, the Reynolds number of the test environment would need to match that of the full-sized crawler under the target conditions. However, Reynolds number is proportional to both the flow velocity and the characteristic length of the object being tested. This means that if the density and dynamic viscosity of the test fluid cannot be varied, a reduction in size from the full crawler would require an increase in velocity by the same factor to maintain a constant Reynolds number. For perfect similitude, a 1:3 scale model of the craft would need to be towed at 60 knots, which was not possible in the tank where testing occurred. Instead, tests were performed at the highest Reynolds number possible on the equipment available, in order to match the behavior of a full-size shell as much as possible. A scale factor of 1:3 was selected as it would result in the largest model for which the tow tank would be able to accommodate the test fixture, and the models were towed at 2 knots, the maximum speed possible on the Sea Grant tank. These decisions resulted in a test environment with a Reynolds number of $7*10^5$, while that associated with target conditions for the full-sized shell is $2*10^7$. The gap between the two values is large, but crucially both represent highly turbulent flow, so the situations are analogous. Initial test plans called for additional flow simulations to be carried out at the testing Reynolds number to allow direct comparison between CFD predictions and physical test results. Unfortunately, those simulations had to be de-scoped due to time constraints, but future test results should be compared to the predictions of CFD at the testing Reynolds number.

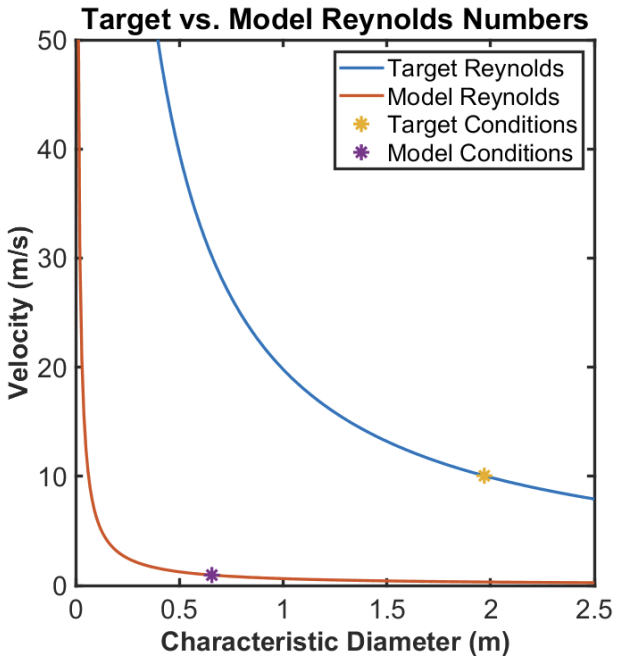

Figure 53. Plot of velocity vs. diameter comparing the Reynolds number at target flow conditions and the Reynolds number achievable in testing. The target and test Reynolds numbers are represented by the blue and orange lines respectively. The target and test conditions are represented by the yellow and purple points respectively. The test conditions are far from the target Reynolds number, but crucially both flows are turbulent

A test fixture was designed to carry each model through the tow tank and imitate the conditions of the crawler's use. Because each of the designs is intended to function when pressed against the exterior of a container ship, the fixture includes a large, flat plate made of 0.25" thick plywood and connected at the wheels to the model being tested, and intended to mimic the geometry of a ship's hull. The plate was designed to be 72" long and 36", so that it would be roughly double the length and width of the largest model, reducing the influence of the edges of the plate on the flow around the models. Boundary layer calculations assuming turbulent flow over a flat plate suggest that the flow is fully developed after 28.3", so each model was mounted with its leading edge 30" behind the leading edge of the plate. Each model was bolted onto the underside of the plate so that tests were run with each model upside down and in constant contact with a large, flat surface. Above the plate, a 12" section of 2cm x 2cm aluminum extrusion extends upwards, where it connects to a mounting plate that then connects to the carriage of the tow tank. Because force readings were taken at the point where the tank carriage is attached to the fixture, drag and lift generated by the fixture itself was included in the data collected. Therefore, a series of tests were performed on just the fixture without any model attached to provide baseline readings of drag and lift that could then be subtracted from future data.

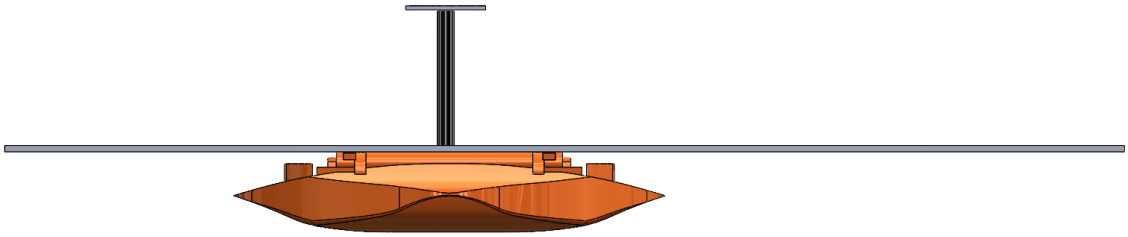

Figure 54. CAD Image of the structure of the test fixture with a scale model of the expanded flow design attached underneath. Fixture consists of a large, flat plate to imitate a ship's hull and an 8 in vertical support attached to the mounting plate for the load cell. The plate is 36 in wide and 72 in long.

Validating the lift and drag estimated from CFD simulations was the primary goal of scale testing, but it was decided that validating the pressure map generated during the simulation would be useful as well. To this end, small pressure sensors were placed at 4 locations on the outside of each model to measure the pressure of fluid on important sections of the crawler. Simulations performed on the original crab design suggested the flow blocked by the wheels would result in a very high pressure in the region under the leading edge of the craft, generating lift. For this reason, one pressure sensor was placed under both the leading and trailing edge of each shell design. Additionally, one sensor was centered on the top of each model and one on the bottom to measure flow traveling over and under the shell. The pressure sensors chosen were small, water-resistant force sensitive resistors rated for forces up to 4.4N. Each has a sensing area with diameter 0.375", meaning the sensors are capable of measuring pressures up to 9.96Pa. In order to fully waterproof the sensors, the edge of each one was sealed using an electronics-grade silicone sealant recommended by the sensors' manufacturer. The leads of each sensor were also sealed using solder-seal wire connections and more of the silicone sealant. After waterproofing, the sensors were connected to a simple voltage divider to measure their resistance, and then calibrated with a series of objects of known weight. During testing, the output of the sensors was measured by an arduino mounted above the water on the carriage of the tow tank.

Due to the support of lab staff and the logistical challenges associated with other potential locations, testing occurred in the intelligent tow tank at Sea Grant MIT. The tank has a test area 1m square and 10m long, with a maximum speed of 1m/s. This limited the Reynolds number achieved during testing, but the data taken at relatively low speeds was still helpful in checking the accuracy of the flow simulations. The tank also has a built-in, 6 axis load cell which simplified the test design. Lift and drag forces experienced by the models were measured by the load cell built into the carriage of the tank. To eliminate the effects of gravity and buoyancy on the final lift reading, the vertical force was measured while the fixture/model assembly was stationary in the tank to provide a baseline that could be subtracted from the test data.

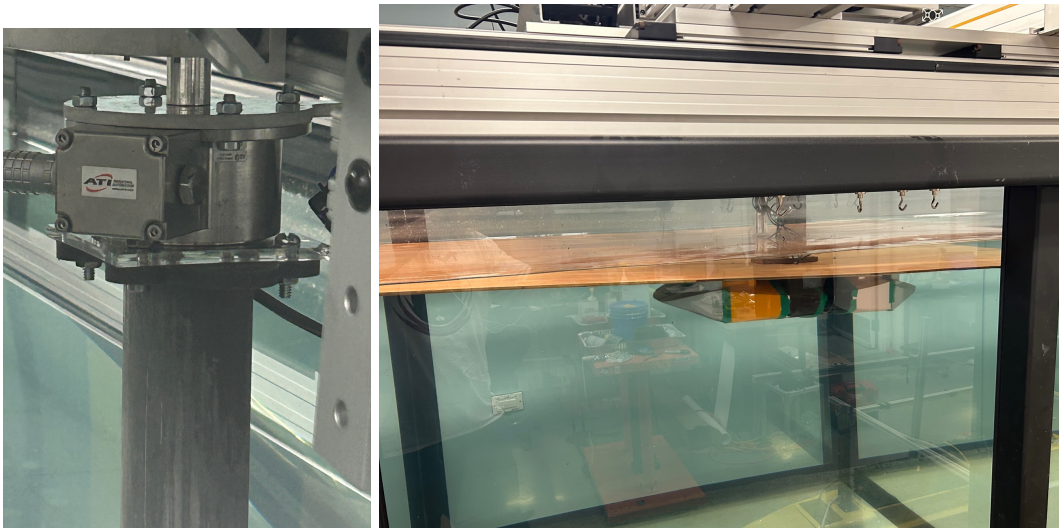

Figure 55. Images of the intelligent tow tank at Sea Grant MIT where hydropackage testing occurred. Pictures depicting first the tank's load cell where the test fixture would attach and also the scale expanded flow model being pulled by the tank during testing.

5.4.2 Scale Model Fabrication

Fused filament fabrication (FFF) 3D printing was the selected manufacturing method to fabricate the scaled models of the two designs. FFF 3D printing was selected because it allowed the team to quickly and accurately fabricate the intricate shapes of the various models. Despite allowing the team to fabricate the desired models to an accuracy of ±0.1mm the surface finish of the final models were still a concern as the striations on the surface of the model produced by FFF printing could affect our testing results as these striations could induce unwanted vortices as the flow passes over the model. To mitigate against the potential effect of these vortices the prints were subsequently coated with a thin layer of protective coating to fill in the gaps in between the striations and create a smooth surface.

The final dimensions of the scale models were still much bigger than the build volume of the 3D printers available to the team. The models thus needed to be divided into several pieces with connecting dowels to assemble the model together after printing. Marine epoxy was then used to glue the components together and to fill in any gaps in between two connecting pieces. In addition to the epoxy, thin strips of electrical tape were also placed along the connecting faces of the parts to ensure the shape of the model was consistent without any abrupt ridges.

Table 12: FFF 3D Printer Settings

Printer	Ultimaker S5
Layer height [mm]	0.2

Wall thickness [mm]	0.8
Wall line count	2
Horizontal expansion	-0.02
Top/bottom thickness [mm]	0.8
Top layers	4
Bottom thickness [mm]	0.8
Bottom layers	4
Infill density [%]	15
Printing temperature [°C]	205
Build plate temperature [°C]	60
Print speed [mm/s]	70
Generate supports	*When necessary*
Support overhang angle [°]	60

5.4.3 Test Results

Physical test results from the tow tank confirmed the conclusion reached during CFD that both the expanded flow and flexible skirt models fail to meet the functional requirements for the hydropackage system. Specifically, both models experienced a strong lift force that would tear CRABI off the ship's hull during actual use. The expanded flow model was found to undergo **37.3 ± 1.9N** of lift and **67.8 ± 5.6N** of drag while towed at 1 m/s. The flexible skirt model experienced **30.5 ± 2.9N** of lift and **57.5 ± 8.9N** of drag. Pressure readings taken during testing were also reasonably similar to those predicted during CFD, so the simulation's prediction that each design would fail at full size is considered verified.

During each test run performed in the tow tank, the model would remain stationary for just over 10 seconds, then it would be dragged down the tank at the specified speed of 1 m/s, and finally it would be slowly dragged backwards to the start position so the next test could begin. Force, moment and pressure data was taken during the entirety of each test, but only data from when the model is moving forward can be used to confirm the findings of CFD. Once these sections of each run had been isolated, the lift and drag forces measured had to be adjusted based on the hydrodynamic properties of the fixture itself. Tests on the fixture ahead of time revealed that the average drag produced was 51.38 N. This value was therefore subtracted from the drag

readings on each model during testing, so that the drag on the models could be isolated. Similarly, the lift readings had to be adjusted to account for the effects of gravity and buoyancy on the model and the fixture. Because air was observed escaping the model after it was placed underwater, its buoyancy likely changed over the course of testing, so picking one value with which to scale results from every test would be improper. Thankfully, each test included the stationary period described above, and the vertical forces measured by the load cell during this period for each test were averaged and subtracted from the related lift readings. Once the lift and drag measurements on the model had been isolated, the final step was to calculate the mean and standard deviation of each dataset, and use them to calculate confidence intervals for the lift and drag experienced by each model.

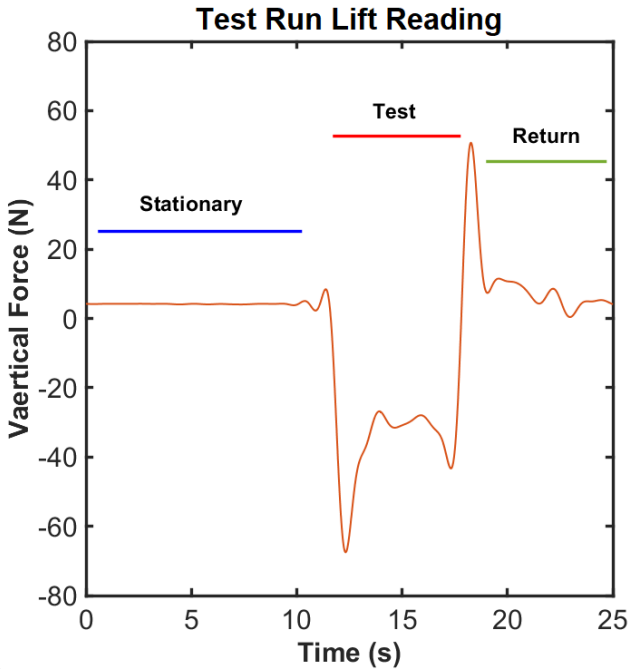

Figure 56. Example lift reading from one test run with the expanded flow model. The plot depicts the periods representing when the model is stationary, when the test is occurring and the return trip.

Data from the pressure sensors placed on the models was similarly processed to isolate the effects of the motion of the models. Pressure data taken during the stationary period at the start of each test was used to estimate the static water pressure experienced by each sensor before motion began. During motion, sensor outputs were averaged to provide an estimate for the pressure at each location on the model. Because the sensors chosen were force sensitive resistors, the output from each was a resistance value rather than a pressure reading. Each estimate therefore had to be converted using the sensor's associated conversion function, which was determined during sensor calibration prior to testing. Once the readings were converted, the

stationary pressure readings were subtracted from those taken during motion, and the resulting pressure estimates were ready for comparison with the CFD results.

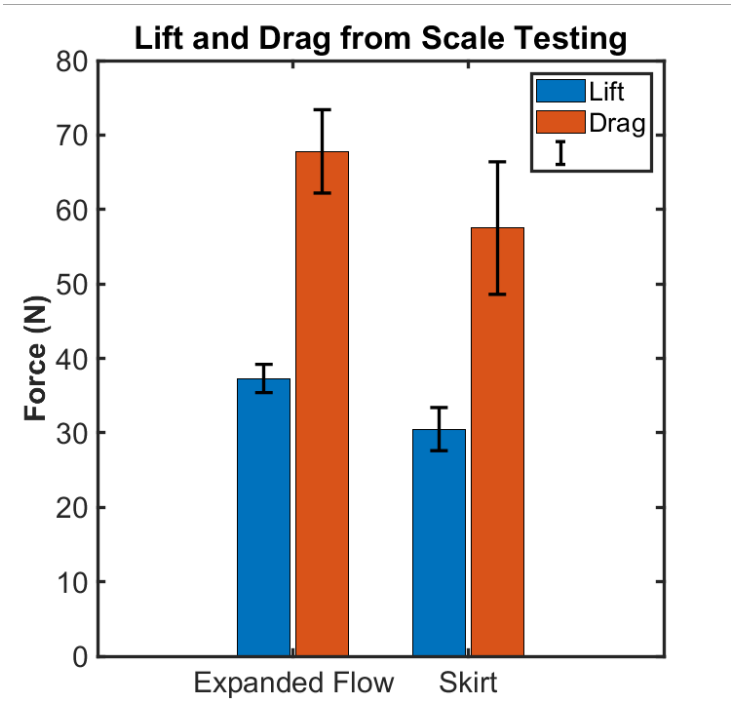

Figure 57. Bar graph depicting the physical lift and drag measured during testing on both the expanded flow and skirt models. From left to right, the chart depicts the lift acting on the expanded flow model (**37.3 ± 1.9N**), the drag on the expanded flow model (**67.8 ± 5.6N**), the lift on the skirt model (**30.5 ± 2.9N**), and the drag on the skirt model (**57.5 ± 8.9N**).

The expanded flow model was found to experience lift of **37.3 ± 1.9N** and drag of **67.8 ± 5.6N** while towed at 1 m/s. The flexible skirt model experienced a similar lift of **30.5 ± 2.9N** and slightly lower drag of **57.5 ± 8.9N**. Each value is included with a 95% confidence interval. It is immediately apparent that a significant lift force was generated when either model was subjected to flow, meaning that likely neither design would function as intended, but further evaluation requires comparison to the results of scale simulations on each model. Pressure data was collected at four points, and then adjusted by subtracting the ambient water pressure when the model was stationary. For the expanded flow model, the water pressure during motion was measured to be **4.1 kPa** under the leading wing, **3.2 kPa** under the model, **2.5 kPa** under the trailing edge and **3.0 kPa** on top of the model. By comparison, the skirt model experienced pressures of **2.0 kPa** under the front wing, **2.2 kPa** underneath the chassis, **2.8 kPa** under the trailing wing, and **3.8 kPa** on top. The high pressure reading under the leading wing of the expanded flow model indicates that pressure is building up in front of the wheel assemblies, and this may be the cause of the powerful lift recorded. The skirt model was intended to prevent lift by blocking flow underneath the shell, and the pressures measured on the underside of the model

were significantly lower than those underneath the expanded flow model. However, the pressure appears to increase as water passes underneath, suggesting that flow may become trapped underneath the trailing wing, creating lift.

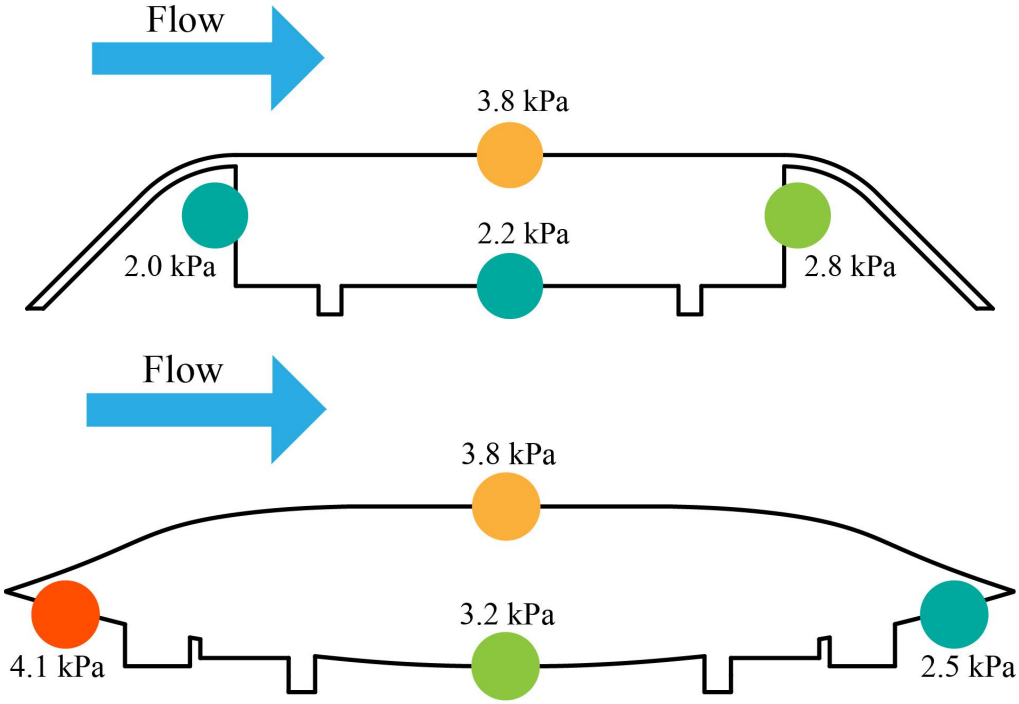

Figure 58. Two simple pressure maps depicting the average pressure measured at each sensor location on first the skirt model and then the expanded flow model. The color of each circle represents the level of pressure measured, with red representing the highest pressures and blue representing the lowest.

Although the difference in Reynolds number discussed above would make direct comparison between the test results and CFD inaccurate, the team was still able to use physical force and pressure readings to evaluate the predictions of the simulations. In general, the results of the physical tow tank testing agreed with those reached by the CFD simulation, but with a few key differences. Although the scale simulations initially planned were not completed, the full size simulations predicted that both models would exceed the lift and drag requirements for a functional hydropackage, which was echoed by the physical data. Furthermore, the pressure increase underneath the leading edge of the expanded flow model was both predicted in CFD and represented in the data collected from force sensors. However, physical testing did reveal certain behaviors that were not predicted by simulations. CFD predicted lift and drag on the expanded flow model to be 30 kN and 11 kN respectively, and the lift and drag on the skirt model to be 6.5 kN and 3.5 kN respectively. The CFD therefore predicted that each model would experience greater lift forces than drag forces, while the results of scale testing suggest the opposite, with drag measurements on each model roughly double the lift experienced. The reason for this

discrepancy is unknown, but it could have resulted from either imperfections in the surface and assembly of the scale models, or some scaling factor due to the difference in Reynolds number between the two environments. Furthermore, pressure readings on the skirt model indicated that flow was still passing underneath the model, and that flow was causing pressure to build under the back wing of the model. This pressure increase was not predicted by CFD, likely because the skirts on the virtual model used for simulations were fixed relative to the surface underneath, blocking flow very effectively. During physical tests, the skirts and fixture plate were able to separate slightly, allowing flow underneath the model to increase. This shows that the ideal nature of flow simulations may cause them to miss certain aspects of the physical behavior of the crawler

Overall, both the predictions of CFD and the results of physical testing agreed that neither the expanded flow model, nor the skirt model would be able to meet the design requirements for the hydrodynamic shell. Most crucially, both methods of evaluation suggested a significant lift experienced by both designs that would cause CRABI to be sucked off the hull if subjected to a 20 knot flow. However, disagreements between the simulations and physical tests like those discussed above reveal that while CFD is a useful design tool, physical tests should also be performed on any future design, as they may reveal aspects of the model's behavior that were overlooked by the simulations. Future design iterations should therefore look to CFD first to determine in a general sense if a design concept shows potential viability, and then turn to physical testing on scale models to confirm the performance of that concept before design or fabrication of a full-size prototype begins.

A number of potential sources of error exist that may have impacted the accuracy of the test data discussed above. Firstly, due to time constraints the number of tests performed on each model was lower than the team would have liked. Furthermore, the large size of the test fixture and limited length of the tank meant that each individual test was quite short, lasting only 6 or 7 seconds. The limited amount of data generated could lead to inaccuracies in the data, and short runs mean that the stopping and starting effects at the beginning and end of each test are more likely to affect the force and pressure readings collected. The lack of stiffness in the fixture itself may have also influenced the force data. The large, flat plate on the fixture was constructed from plywood, and when submerged the edges of the plate deformed slightly upward, away from the model. This change in geometry may have increased the ground clearance of the model beyond the desired level. Furthermore, during testing the flow of water around the plate induced a visible wobble in the plywood. This unintended motion likely had some effect on the force measurements taken and may have been responsible for unexpected fluctuations in the drag forces measured during testing. For future tests, either choosing a stiffer material for the plate or designing additional reinforcement might improve the quality of the data collected. Finally, the models themselves were imperfect, and may have experienced higher drag forces as a result. The models were assembled from multiple 3D printed parts, and the assembly was not perfect. There

were small gaps in the body covered with epoxy or tape, and the surface of the models, in particular the expanded flow model, was uneven in places. If these imperfections were prevented on future models, the results would be better suited for comparison to CFD results.

5.5 Future Work

5.5.1 Hydrofoil Integration

As we've seen through CFD results and testing, lift was present in all of our models. To solve this problem, a promising approach would be to include hydrofoils on the shell. These 'inverted wings' would help us create an additional downforce and keep CRABI on the hull, although being subject to high velocity and turbulent current.

An important phenomenon to think about is that adding wings on the side of CRABI wouldn't only create the downforce we want, but would also create unwanted drag. Due to the coefficient of friction of the wheels, 1N of lift would be compensated by 1N of magnetic force, but 1N of drag would need a compensation of 2.6N. Luckily, wings are streamlined and the ratio of coefficient of lift and coefficient of drag (Cl/Cd) is almost always higher than that 2.6 ratio.

The first idea is to take a wing that performs well under high Reynold's number flow, such as the Prandtl-D-tip at a pitch of ~-6°. This would allow us to create significant downforce on CRABI and a slight increase in drag. Given the high Cd/Cl coefficient of this wing under important Reynold's number, the added drag could easily be compensated by adding magnetic force and the downforce created would be worth this added drag.

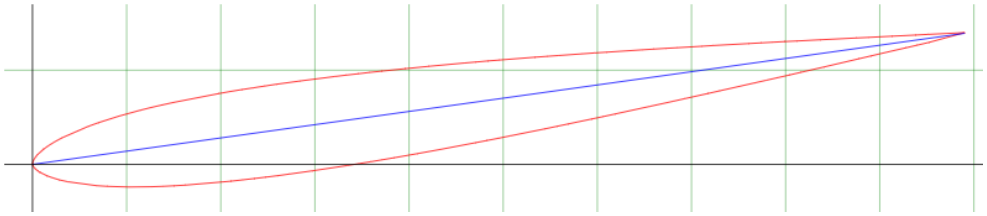

Figure 59. Prandt-D-tip wing section at a pitch of -6°. This wing creates a lot of downforce and little drag.

Although analysis hasn't been performed on this model due to time limitation, adding hydrofoils to the shell would be very promising and might be the solution to our problem of lift. A last issue that needs to be tackled is the inversion of the flow as CRABI turns around. As we need pitch on the wings, they would need to be rotated to face the other side of CRABI when the whole system turns around. This could be solved by adding a wing with a negative camber in order to create downforce without any pitch, therefore not needing to invert it as CRABI turns around.

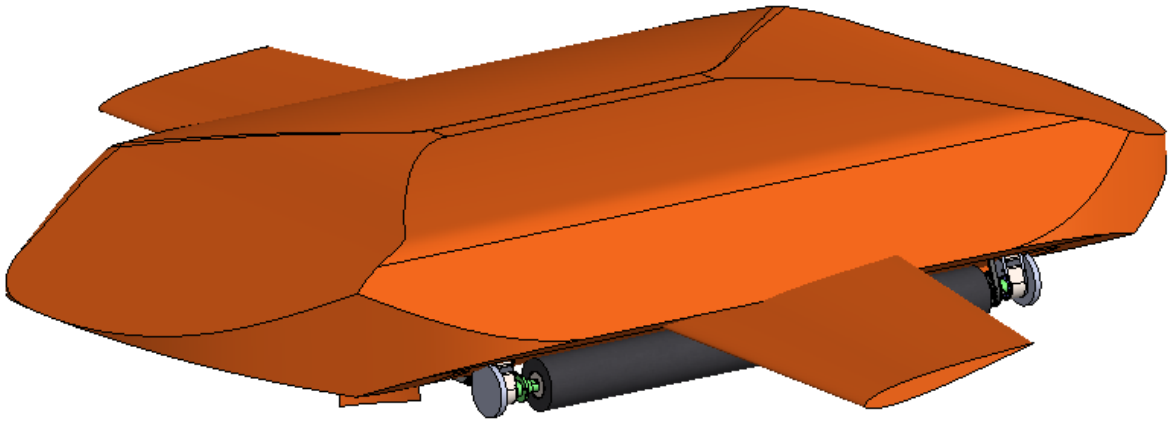

Figure 60. Crab shape model with hydrofoils added on to improve downforce.

5.5.2 Full-Scale Manufacturing

There are three possible options for full scale manufacturing of the final selected design. The key areas of concern for full scale manufacturing are the attachment points to the chassis of the vehicle and the accuracy of the exterior shape. The accuracy of the exterior shape is especially critical as this will drastically affect the hydrodynamic performance of CRABI and potentially cause large deviations from the expected lift and drag forces calculated through CFD and verified from physical testing.

Table 13: Pros and cons comparison between possible manufacturing processes for the full scale manufacturing of CRABI's selected hydrodynamic shell

Manufacturing Process	Pros	Cons
Thermoforming	• Smooth surface finish • Can achieve fairly accurate profiles	• Difficult to achieve the features required to allow for attachment to the chassis
Sheet metal bending	• Smooth surface finish • Would produce the most robust shell out of the three processes	• Difficult to achieve an accurate profile for the extended flow model design • Difficult to achieve the features required to allow for attachment to the chassis
Big Area Additive	• Can achieve very	• Rough surface finish

Manufacturing (BAAM) 3D printing	accurate profiles ● Easy to achieve the features required to allow for attachment to the chassis	with consistent striations ● Would require the use of a BAAM 3D printer, which is not easily accessible but Big Rep 3D is a possible option in the Boston area

The full scale manufacturing of the shell has been descoped from this project due to time constraints and various delays throughout the project timeline. Future work for the manufacturing of the hydrodynamic shell would include selecting the most suitable manufacturing process from the above options suggested or any other option determined to be better than the proposed, contacting manufacturers, fabricating the design and assembling it to the chassis of the vehicle.

6. Electronics

Though internal electronics and navigation were descoped due to the program time constraints, an electrical system was still required to test CRABI. To perform the needed tests, the crawler had to be powered and capable of a reasonable tethered operation range and ergonomic manual control. **Section 6.1** will discuss the exact requirements needed for the electrical system, **Section 6.2** the overall architecture created, **Section 6.3** the high-voltage (HV) circuit, and then **Section 6.4** the low-voltage (LV) circuit. Finally, **Section 6.5** describes the realized assembly and performance.

6.1 Functional Requirements

In order to enable the required testing regime, the following functional requirements were compiled in **Table 11** for the electronics system. These requirements are driven by the Lin Engineering BL23E33-02 motors selected and discussed in the prior sections.

Table 14: Electronics System Requirements

Functional Requirement	Target Value	Source	Verification
Power Supply Voltage	48 V	Motor Requirements	Power Supply Testing
Power Supply Current	20 A	Motor Requirements	Power Supply Testing

Controller Power Rating	84 W	Motor Requirements	Controller Testing
Controller Voltage	48 V	Motor Requirements	Controller Testing
Transmitter Channels	3 Channels	Design Criteria	N/A
Power Tether Length	3 m	Operational Test Range	Measurement

6.2 Electrical Architecture

The overall architecture created consists of two circuits supplying power and signals to drive the motors. The critical component required to interface with the motors are the motor controllers, so careful consideration was given to the controller selection. Potential controllers were evaluated based on their energy requirements, ability to perform BLDC control, and compatibility with the motors. The resulting controller was the Lin Engineering BLDC 50 Driver and Controller module, chosen for its ease of use and flexibility in signal input. The combined driver and controller reduced complexity in the electrical harnessing.

The bulk of the harnessing is situated on CRABI itself, with the power supply being the main dissenter. A tether connects the electronics on CRABI to power and yields the operating range. Onboard CRABI, two circuits were devised in order to operate the controllers: a high-voltage (HV) circuit to supply power and a low voltage (LV) circuit to provide the control signal.

A major consequence of the program's time constraints was the elimination of the battery concept from the 2.013 design. Rather than tackling the battery, which is a solved problem but difficult to incorporate, the decision was made to showcase the novel technologies of CRABI instead. To simplify the power subsystem, CRABI will function on tethered power from an external power source. In contrast to a battery, a power tether is much simpler to implement, less tedious to perform test trials with, and more cost effective for our minimum viable product. This tether serves two purposes: the delivery of power and the delineation of the operational range of CRABI.

6.3 High Voltage Circuition

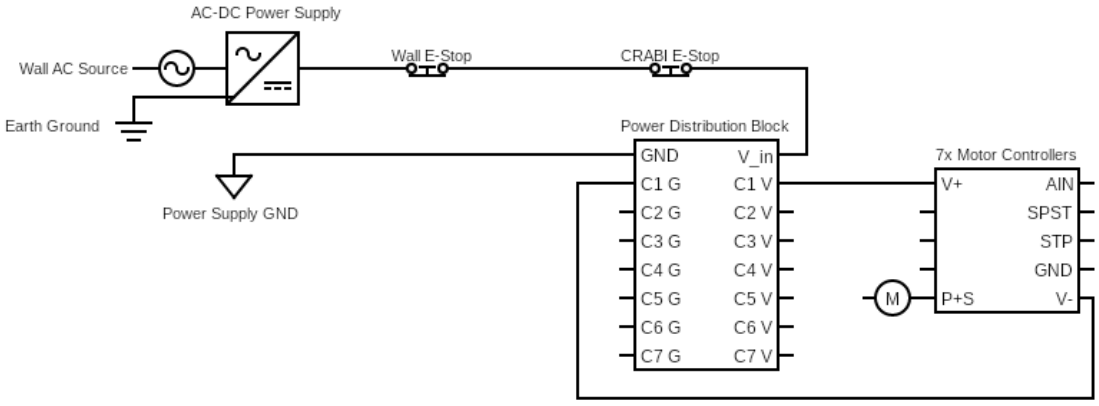

Figure 61: The HV circuit for power delivery to the motors. Two emergency stop buttons are implemented, one at the power supply and one on CRABI. A singular terminal block distributes power to all seven controllers and motors.

The main components of the HV circuit are the power supply and power distribution blocks. There are seven motors, each rated for 48V and 3A. The brush motor is not expected to draw maximum current; its load is lighter than the drivetrain motors. To streamline circuitry, only one power supply will be used, so the singular supply must be able to output 48V and ~20A. Accordingly, CRABI uses a switching power supply capable of drawing AC power from the wall and rated for 48VDC and 20A. The output current is directly connected to the power distribution blocks to power the motors. Since the power distribution occurs onboard CRABI while the power supply lies stationary at the wall, proper cabling is required to bridge the gap safely.

The connection is made using 10ft (3m) long, 14 gauge insulated wire with a current load carrying capacity of 20A, suitable for the motor loads and desired testing range of CRABI. Due to its prototypical nature, safety measures are required to properly test CRABI. Two directly accessible emergency stop buttons are implemented along the power supply to distribution block line: one directly following the supply terminals and one directly preceding the block. These emergency stops have normally closed (NC) switch contacts, so the current flow is interrupted when the buttons are depressed. In the case where a malfunction such as a circuit disconnection or a conduction failure occurs, the NC circuit structure prevents current flow after activation even when the button is reset, providing a safe failure of CRABI. These emergency stops allow for increased safety during testing as operators can stop all CRABI motion by pressing either the onboard stop button or the static button in the case of a situation where it is dangerous to approach CRABI. From the onboard button onward, the remaining HV circuitry lies within CRABI itself.

Since the seven motors require concurrent power, they must be wired in parallel, leading to the issue of insufficient output terminals on the power supply. The purpose of our power distribution blocks is to split the single input line from the supply into seven identical output lines for the controllers. A 2x10 terminal distribution block with high current capacity was thus chosen to split the power supply current to the controllers and collect the returning ground wires before connecting to the supply ground. The current supplied to the individual controllers does not exceed 3A, so lower-capacity 18-gauge wire is used to connect the distribution block and the controllers, thereby completing the HV circuit.

6.4 Low Voltage Circuit

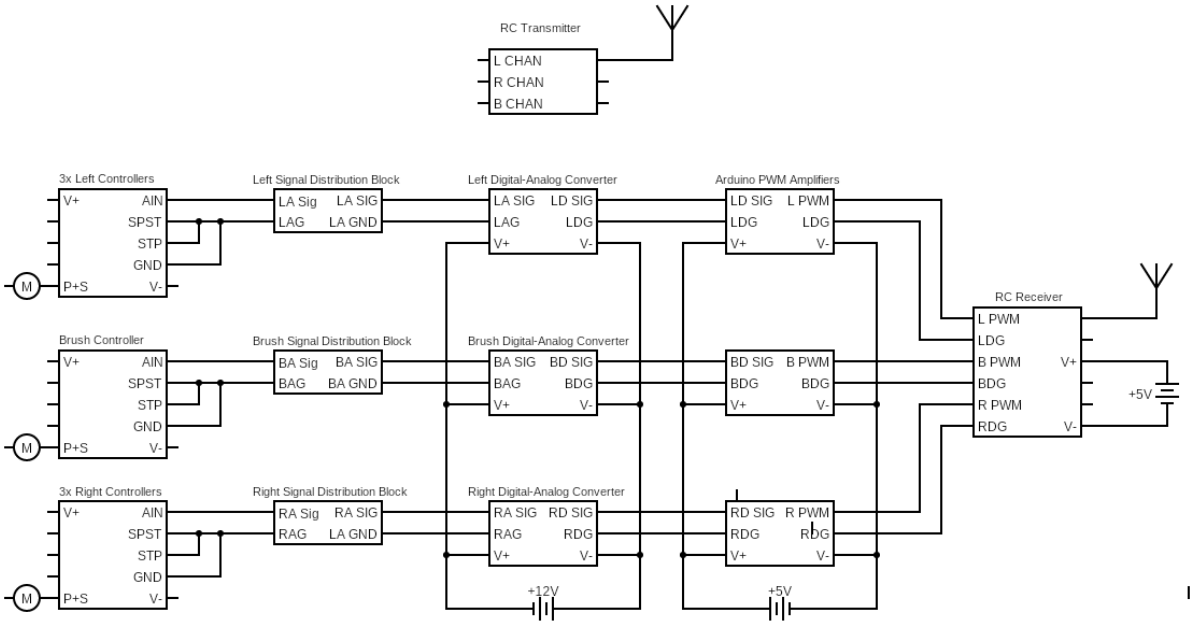

Figure 62: The LV circuit provides speed control of the motors. Arduinos and DACs respectively amplify and convert the receiver PWM signal to an analog voltage, which is then distributed by terminal blocks to the controllers.

In order to control the motors, we will be using a low-voltage (LV) signal circuit with a radio transmitter and receiver. CRABI is operated with three sets of identical motors: the left motors, the right motors, and the brush motor. For brevity, the motors and control signals will be denoted by the set they refer to: L for left, R for right, and B for brush.

For full planar motion and brush speed control, the transmitter must be capable of sending distinct L, R, and B signals to the respective sets of motors. This necessitates a transmitter and receiver with three distinct input and output channels for the controllers, as well as a minimum range of 3m. The range requirement is fortunately very low; essentially all radio

control systems are able to meet it. For the channel requirement, we are choosing to use the Element-6 Radio Control System from goBILDA, which has four channels of gimbal proportional control, one three-stage switch channel, and one proportional knob channel. The gimbals, or joysticks, provide intuitive movement control mechanisms for the user, and the knob allows them to dial into and stay at a particular brush speed. The transmitter sends these inputs to the receiver at 2.401–2.479 GHz with a maximum range of 800 meters. Both the transmitter and receiver are powered by AA batteries, using an internal 6V battery tray and an external 6V battery holder, respectively.

There are a couple of key limitations in using this radio control system, both stemming from its original purpose of servo control. Since servos are most commonly controlled through digital 5-10% duty cycle range PWM signals, the goBilda system only outputs low duty PWM. The motor controllers only accept a 0-5V analog input. This problem is rectified in two steps. Firstly, in order to amplify the receiver's PWM signals, Arduino Unos read the receiver's output, one for each signal, and then scale and output a 0-60% duty cycle range PWM. These Arduinos are powered in parallel with a 5V battery. Next, in order to transform the digital signal to an analog one, we use digital-to-analog converters (DAC). These DACs take in a PWM signal and then output the duty cycle's equivalent voltage in a 0-10V range. To step down the output voltage, the DAC's are fed 12V in parallel, 80% of their nominal voltage, which the output voltage range is directly proportional to. The Arduinos' 0-60% duty cycle output further reduces the maximum output voltage to 50% at 5V. The connections between the receiver, Arduinos, and converters are all made using jumper wires, capable of carrying the low signal current and ideal for prototyping and testing with the Arduino Uno microcontroller.

For analog input, the controllers require specific connections. The analog input signal must be connected to the AIN pin, and the SPEED-SET, STOP, and GND pins must be grounded. As such, each controller requires four connections in the LV circuit. Accordingly, the L and R signals must be split three ways and the grounds nine ways to accommodate the motor count on each side. To accomplish this, three thirteen channel output distribution terminal blocks are utilized, one per signal. The blocks take in the analog signals from the converters and their outputs direct to the controllers as specified, allowing control of multiple motors from one signal. Again, due to the low current load, gauge 18 wire will be used for the converter-distribution blocks and distribution blocks-controller connections; the latter will be soldered due to the different gauge of the controller pin inputs.

The entirety of the LV circuit, sans the transmitter, is situated on CRABI. To avoid obstruction of the radio signal, the receiver is fastened to the top of the shell. The converter and the signal distribution blocks are moored on the same plastic sheets as the HV circuit components, leading to the same controllers and motors. Thus, the LV circuit is secured and completed.

6.5 Performance

Testing of the drivetrain was de-scoped due to time limitations.

7. Future Work

Design work done this semester was focused on identifying and addressing major risks for this technology that also aligned with team members' areas of expertise. Based on the progress from the semester, the team recommends that initial prototyping and testing work focuses on cleaning, attachment/propulsion, and sealing.

Subsystems that are currently least developed are the hydropackage, chassis, navigation, and power subsystems. Meanwhile, additional detailed design work and DFM remains for all subsystems.

7.1 Remaining Risks

Design and test work on CRABI so far has centered around addressing the most concerning risks identified when design began. As a result, serious risks in the cleaning, attachment and propulsion, chassis, and hydropackage subsystems have been addressed. However, potential risks remain in subsystems at various stages in the design process. Included below is a table of the most serious remaining risks, and potential mitigation strategies to be explored in the future.

Table 15. Remaining Risks and Mitigation

Risk	Severity	Mitigation
At high speeds, drag exceeds friction	*Low*	*Radio terminals to position craft as it exits water in case of slipping. Continued hydropackage iteration could either reduce drag or create downforce to boost friction.*
High flow rates break adhesion with hull	*Medium*	*Creating additional downforce by either adjusting hydropackage or attachment systems. Bringing multiple crafts to replace those lost to current.*
Power system fails during use	*Medium*	*Charging the craft before and after relatively short use cycles. Designing onboard systems for monitoring battery levels and temperature during use.*

Risk	Severity	Mitigation
At high speeds, drag exceeds friction	*Low*	*Radio terminals to position craft as it exits water in case of slipping. Continued hydropackage iteration could either reduce drag or create downforce to boost friction.*
High flow rates break adhesion with hull	*Medium*	*Creating additional downforce by either adjusting hydropackage or attachment systems. Bringing multiple crafts to replace those lost to current.*
Craft loses its position underwater	*Low*	*Relocating the crawler whenever it leaves the water with transmitters on the ship. Testing the onboard odometry system under use conditions to improve performance.*
Detached crawler hits propeller	*High*	*Designing chassis to break apart on detachment to reduce damage. Focusing cleaning efforts on other parts of the hull to reduce risk of contact*

7.2 Prototype Testing Regime

7.2.1 Existing Prototype Testing

The CRABI Prototype as it exists now consists of the Cleaning, Attachment & Propulsion, and Chassis subsystems powered by a temporary power system. Because the prototype is missing several subsystems that would be included in the final design, several aspects of the design cannot yet be tested. However, several tests could be conducted to evaluate the existing functions of the vehicle.

1. ***Cleaning*** - The existing prototype could be made to run back and forth over biofouled steel samples in order to evaluate the cleaning capabilities of the vehicle. Tests would be similar to the cleaning testing that occurred on the brush alone, but now it would be powered by its motor and held in place by both the chassis and attachment subsystems. Quantitative data from these tests could include measurements of the amount of biofouling removed during each pass, or the number of passes required to clean a sample. Testing would allow validation of the cleaning abilities of CRABI, and could be used to fine-tune cleaning parameters like the brush rotation speed.
2. ***Attachment*** - The strength of the attachment subsystem should be tested to ensure that the crawler can function as intended. Generating sufficient downforce is extremely important, and while the individual magnetic skis have been tested, it may be useful to test the normal force generated by the assembled prototype. Data could be generated by

placing load cells under each wheel, although the powerful magnets involved might interfere with the sensors.

3. ***Movement*** - The mobility of the crawler can also be evaluated using the attachment, propulsion and chassis prototypes. The craft could be manually operated along paths similar to those the crawler would take during cleaning, and over curved surfaces mimicking the geometry of a ship's hull. Testing the suspension system to ensure that the vehicle can traverse surfaces of the necessary curvature while maintaining the required adhesion force. This test could prove difficult to design, but would involve sourcing a magnetic sample with the desired geometry, and some kind of force sensor to evaluate the downforce generated by the magnetic skis.

7.2.2 Additional Subsystem Testing

Several of the subsystems intended to be fitted to the final crawler have not yet been designed, and these subsystems will require additional testing before they can be integrated into the final prototype. In particular, a final design for the hydropackage has not been selected and additional tow tank testing will be required as design iteration continues. These tests would likely look similar to those discussed in **section 5.4**, and would be used to verify CFD results on each design tested. Once a design is selected, a full sized prototype of the shell can be fabricated and subjected to additional testing to verify the findings of CFD at full scale and speed. Other subsystems were de-scoped for the project so far, so significant design work would be required before testing could occur. Once a power subsystem is designed and built, it could be tested by measuring the power output and capacity of the system, as well as its ability to recognize when it starts to fail. The navigation subsystem could be tested by directly comparing odometry to physical location, and evaluating the system's ability to communicate with the transmitters used to verify the crawler's location.

7.3 Subsystem Revisions

7.3.1 Cleaning

The cleaning arms and brush shaft could benefit from cost reduction DFM, as discussed in section 2.3.3. With additional calculations, more material could be removed from the arms to reduce total subsystem weight. Further iterations of the brush shaft should be redesigned to press fit directly into the stock. If the tolerances on the cylindrical stock are too loose, laser cutting the ends of the tube could be explored. The inner diameter of the brush bearing block should be increased, which removes the need for post-machining to prevent binding of the spherical bearing.

7.3.2 Attachment and Propulsion

The drivetrain has largely been validated this semester, but a few key issues remain, as well as recommendations for future design revisions. Foremost, the suspension lacks toe/tie rods, and is under-constrained - this must be resolved before it can operate successfully. Additionally, the shock springs are likely too compliant. The O-ring discussed here caused excessive friction, and testing must be conducted to determine its nescestity. Remaining design work to be pursued includes structural analysis of the suspension mounts, lifetime analysis of the wheel, a better tire adhesion mechanism. Future revisions should replace the excessively large NEMA 23 packaged motor and gearbox with a higher torque motor, and a custom gearbox, as this will save significant mass, potentially cost, and ease the severe packaging issues present with the suspension.

7.3.3 Chassis

The chassis had been prototyped this semester, aligning with the program objectives of building a minimal viable product in an accelerated timeline with limited resources. As a result, much of the chassis design could be improved in terms of decreasing mass and cost by implementing more critical design for manufacturing/design for assembly practices. The initial path to mass optimizing the chassis would be to build a full finite element model (FEA) of the structure. Due to the non-linear nature of the tab slot box tube structure (which is highly dependent on the bolt preload), the stiffness of a single box tube/beam kit could be derived using a finite element model using solid elements. The entire chassis structure could then be modeled using a beam element with a defined stiffness. Obtaining accurate stiffness from the FEA model is crucial to reducing the mass while making sure to maintain positive yield allowable margins. Bolt preload, which would be dependent on beam kit stiffness needed, need to be determined. If the bolt preload is too low, the stiffness requirements from cleaning and suspension subsystems would not be met which would affect functionality. Bolt preload also poses the risk of yielding the beam side plates (if too high) due to the eccentric loading nature of the bolt preload. Therefore, bolt preload must be determined keeping these tradeoffs in mind. The chassis could also be improved redesigning some components to incorporate poka yoke methodology would be error proof the assembly which would be helpful in successive iterations of the prototype on the path to commercialization and mass manufacturing. Furthermore, many components could either be deleted (by reusing existing components in its place) or simplified by using symmetry (such as the cleaning mounts) which would allow for easier assembly and less components to keep track of. These changes would have the potential of further reducing the manufacturing cost of the chassis.

7.3.4 Hydropackage

Despite design iteration by the team over the past year, an acceptable version of the hydropackage has not yet been found. All designs proposed thus far have failed to meet the lift and drag requirements for the subsystem that would allow CRABI to adhere to the ship. Therefore, subsystem revisions would center around continued iteration to find an acceptable design. Currently the concept of attaching hydrofoils to the shell shows promise (**section 5.5.1**), but both CFD and physical testing would have to occur before the concept can be verified. Future work should begin with the search for a functional shell design, as failure to find one may necessitate significant redesign of other subsystems. Additionally, no decision has been made on how a full-sized version of any shell design would be fabricated. Potential methods are discussed in **section 5.5.2**, but additional research should be performed before a selection is made.

7.4 Remaining System Designs

7.3.1 Power Subsystem

To power the other systems, a power supply is needed. The proposed system employs a rechargeable lithium-ion battery that is large enough to support a cleaning cycle of the entire hull. Detailed design of this subsystem was de-scoped, but proposed functional requirements for the system are included here.

Table 16. Power subsystem design requirements

Design Requirement	Target Value	Source
Supplies enough power for driving, cleaning, and sensing	450 W *0.60 hp*	Design Requirements
Stores enough energy for a full cleaning cycle	4.6 hrs (~2000 Wh)	Design Parameters
Minimizes risk of battery fire	N/A	N/A
Tolerates operating temperature and pressure ranges	4º -30ºC 1 -2.6 atm	Design Requirements
Resists salt water environment *Ingress and corrosion*	N/A	Design Requirements
Mass allocation	20 kg	Design Requirements

The power subsystem would consist of a rechargeable battery that connects to the propulsion and cleaning motor controllers and motors. The expected power budget for the

crawler is 440 W. The majority of the power requirement is attributed to propulsion power required to overcome rolling resistance and drive against gravity while moving up the side of the hull. The final battery should be selected to meet the overall energy storage requirement as well as motor and motor controller voltage and current requirements. Preliminary research suggests that EV modules may be good candidates to match the energy requirements of the crawler. When using high energy density batteries, the team should pay special attention to proper battery management for safe operation.

Beyond the battery, motor controllers and converters to support charging and powering of low-voltage electronics must be selected. The motor controllers will interface with the battery and motors to direct power flow and with the computer and motors for data flow. Hardware for battery charging must be compatible with the power generation infrastructure of the parent vessel. Initial research shows that power is commonly generated at 440 V, 60 Hz, but is also stepped down for lighting and other domestic supplies.

7.3.2 Navigation Subsystem

The navigation subsystem will be made up of sensing and controls that direct the crawler along a standard driving path. Detailed design of this subsystem (i.e. component selection, packaging, and writing the navigation algorithm) was de-scoped for this semester, but preliminary functional requirements for the system are included here.

Table 17. Power subsystem design requirements

Design Requirement	Target Value	Source
Navigates sections of the hull to be cleaned autonomously	*N/A*	N/A
Avoids non-traversable regions	N/A	N/A
Senses emergency events that require path deviations	N/A	N/A
Tolerates operating temperature and pressure ranges	4º - 30ºC 1 - 2.6 atm	Design Requirements
Resists salt water environment *Ingress and corrosion*	N/A	Design Requirements

To navigate along a standard driving path, the crawler should have sensing capabilities for absolute position, orientation, and odometry (distance traveled). Additionally, the crawler

should have backup sensing capabilities to inform emergency deviations from the standard driving path. This secondary navigation suite should include information about the battery status (e.g. temperature, state of charge) and immediate obstacles in the crawler's path. This navigation information would feed into an on-board computer that controls the propulsion and cleaning motors. Due to communications limitations underwater, the navigation subsystem should be designed for communications capabilities above water. After a strip of the hull is cleaned and the crawler surfaces to reorient for cleaning the next section of hull, it should be able to communicate its location and battery status to a controller on deck.

For ***absolute position***, it is suggested that radio triangulation be used each time the robot pops up above the waterline. By keeping communications hardware above water, the ship would not need to be dry-docked to install the system. A next step for this system would be to identify location requirements for receiver stations. For ***orientation***, an IMU can be used to identify the direction of gravity and another sensor should be selected or developed to measure the direction of the flow of water past the crawler. The purpose of this second sensor would be to orient the robot relative to the direction of motion of the ship while on the bottom section of the hull. For ***odometry***, a 2D sensing system is proposed, independent of wheel encoders to help track both distance in the direction of robot travel and slippage in the perpendicular direction. This system would operate similarly to a computer mouse and may be either mechanical or optical. The next step for evaluating feasibility of either mechanical or optical odometry could be to waterproof computer mice with this technology and test their performance in turbid underwater conditions.

8. Acknowledgements

This project would not have been possible without the generous aid of numerous people, whom the authors attempt to enumerate here, but do not assert that the list is complete. Foremost, they would like to thank the project sponsors, Scott Van Broekhoven and Tony Tau, for both funding the work and providing extensive consults. Likewise, Professors Jeffrey Lang and David Trumper gave invaluable aid in designing the magnetic skis, together with Dr. Andrew Bennett and his lab group who among many other suggested improvements, helped design the motor labyrinth seals. They are grateful for Pierce Hayward providing access to and instruction on the Instron machine used for the magnetic testing, to Joseph Gaken for his deft handling of purchasing logistics, and to Joel Grimm for his logistical aid and management of the machine shop used. To Jack Whipple, they are profoundly grateful for his aid in welding the prototype. Additionally, they would like to thank Mathew Sullivan for granting the team access to his personal boat to test cleaning techniques. Finally, the authors are grateful for the instruction and guidance provided by the course staff, Douglas Hart, Alfonso Perez, Maaya Prasad, Michael Wardlaw, Michael Trice, and Juergen Schoenstein.

10. References

[1] Perkins, S., 2011, “A Warming World Could Add Billions to Shipping Costs | Science | AAAS” [Online]. Available: https://www.science.org/content/article/warming-world-could-add-billions-shipping-costs. [Accessed: 21-Sep-2022].

[2] Orszag, P. R., 2021, “Huge Container Ships’ Biggest Problem Is Emissions,” Bloomberg [Online]. Available: https://www.bloomberg.com/opinion/articles/2021-03-30/huge-container-ships-biggest-problem-is-emissions. [Accessed: 14-Dec-2022].

[3] Rodrigue, J.-P., 2017, “Fuel Consumption by Containership Size and Speed | The Geography of Transport Systems.”

[4] Hanssens, O., “Shipshave ITCH – In Transit Cleaning of Hulls,” Shipshave [Online]. Available: https://shipshave.no/. [Accessed: 14-Dec-2022].

[5] “Biofouling - an Overview | ScienceDirect Topics” [Online]. Available: https://www.sciencedirect.com/topics/earth-and-planetary-sciences/biofouling. [Accessed: 06-Oct-2022].

[6] Oliveira, D. R., Lagerström, M., Granhag, L., Werner, S., Larsson, A. I., and Ytreberg, E., 2022, “A Novel Tool for Cost and Emission Reduction Related to Ship Underwater Hull Maintenance,” Journal of Cleaner Production, **356**, p. 131882.

[7] Nishizaki, M. T., and Carrington, E., 2015, “The Effect of Water Temperature and Velocity on Barnacle Growth: Quantifying the Impact of Multiple Environmental Stressors,” J Therm Biol, **54**, pp. 37–46.

[8] 2006, “Waterborne Underwater Hull Cleaning of Navy Ships,” *Naval Ships’ Technical Manual*, Naval Sea Systems Command.

[9] Oliveira, D., and Granhag, L., 2016, “Matching Forces Applied in Underwater Hull Cleaning with Adhesion Strength of Marine Organisms,” Journal of Marine Science and Engineering, **4**(4), p. 66.

[10] “Barnacle / Hull Growth Prevention,” Florida Sportsman [Online]. Available: https://forums.floridasportsman.com/discussion/187296/barnacle-hull-growth-prevention. [Accessed: 27-Sep-2022].

[11] “How Long before Barnacles Grow?,” The Hull Truth - Boating and Fishing Forum [Online]. Available: https://www.thehulltruth.com/boating-forum/136953-how-long-before-barnacles-grow.html. [Accessed: 27-Sep-2022].

[12] 2014, “Fouling, Marine Growth, Algae and Barnacle | Scrubbis.”

[13] Song, C., and Cui, W., 2020, “Review of Underwater Ship Hull Cleaning Technologies,” J. Marine. Sci. Appl., **19**(3), pp. 415–429.

[14] Conners, D., “Call with Boston Ship Repair.”

[15] 2022, “Thermocline,” Wikipedia.

[16] Webb, P., *Ocean Temperature*, Roger Williams University.

[17] 2019, “Container-Ship Size: What Dimensions Can We Expect to See?,” PierNext.

[18] Schreurs, M., and de Haan, F., 2012, “Keep Moving, Towards Sustainable Mobility.”

[19] “State of the Ocean” [Online]. Available: https://podaac-tools.jpl.nasa.gov/soto/#b=BlueMarble_ShadedRelief_Bathymetry&l=GHRSST_L4_MUR_Sea_Surface_Temperature(la=true,lpr=4.20_30.75)&ve=126.22328965805062,-43.75566242629637,399.735717589587,84.26334898054773&pl=false&pb=false&d

=2022-02-04&ao=false&as=2022-09-24&ae=2022-10-01&asz=1/day&afr=500&tlr=days. [Accessed: 06-Oct-2022].
[20] Alfred M. Kracht, “Design of Bulbous Bows.”
[21] Davidson, I., Cahill, P., Hinz, A., Kluza, D., Scianni, C., and Georgiades, E., 2021, “A Review of Biofouling of Ships’ Internal Seawater Systems,” Frontiers in Marine Science, **8**.
[22] “UTILIZATION RATE OF CONTAINER SHIPS INCREASES: PIERS | JOC.Com” [Online]. Available: https://www.joc.com/maritime-news/utilization-rate-container-ships-increases-piers_19990811.html. [Accessed: 21-Sep-2022].
[23] Institute for Trade and Transportation Studies, 2009, “Comparison between Panamax and Post-Panamax Container Vessels.”
[24] “Ship Fuel Spikes to Historic $1,000/Ton Mark as War Fallout Worsens” [Online]. Available: https://www.freightwaves.com/news/russian-invasion-propels-price-of-ship-fuel-to-historic-high. [Accessed: 21-Sep-2022].
[25] Uzun, D., Demirel, Y. K., Coraddu, A., and Turan, O., 2019, “Time-Dependent Biofouling Growth Model for Predicting the Effects of Biofouling on Ship Resistance and Powering,” Ocean Engineering, **191**, p. 106432.
[26] Hampus Tober, 2020, “Evaluation of Drag Estimation Methods for Ship Hulls,” Royal Institute of Technology in Stockholm.
[27] Mulligan, R. F., and Lombardo, G. A., 2016, “Panama Canal Expansion: Fuel Economy and Logistical Risk,” WMU J Marit Affairs, **15**(1), pp. 5–15.
[28] Read, D., “A Drag Estimate for Concept-Stage Ship Design Optimization,” p. 172.
[29] 2011, “Underwater Ship Husbandry Discharges,” United States Environmental Protection Agency: Office of Wastewater Management, p. 27.
[30] Industries, M. for P., “Biofouling Management” [Online]. Available: https://www.mpi.govt.nz/import/border-clearance/ships-and-boats-border-clearance/biofouling/biofouling-management/. [Accessed: 21-Sep-2022].
[31] 2011, *2011 Guidelines for the Control and Management of Ships’ Biofouling to Minimize the Transfer of Invasive Aquatic Species*, Annex 26, The Marine Environmental Protection Committee.
[32] “Biofouling: Countries Getting Tough on Clean Hull Requirements” [Online]. Available: https://www.nepia.com/articles/biofouling-countries-getting-tough-on-clean-hull-requirements/. [Accessed: 21-Sep-2022].
[33] “Anti-Fouling and in-Water Cleaning Guidelines” [Online]. Available: https://www.agriculture.gov.au/biosecurity-trade/aircraft-vessels-military/vessels/marine-pest-biosecurity/biofouling/anti-fouling-and-inwater-cleaning-guidelines. [Accessed: 21-Sep-2022].
[34] Zabin, C. McClay, T. Davidson, I. Young, R. Elam, D., 2015, *Vessel Biofouling Prevention and Management Options Report*, CG-D-15-15, Acquisition Directorate: Research & Development Center.
[35] “Design an Open Wound Coil Brush,” Precision Brush [Online]. Available: https://precisionbrush.com/design-a-open-wound-coil-brush. [Accessed: 3-Mar-2023].
[36] “Cylindrical Conveyor Brush,” McMaster-Carr [Online]. Available: https://www.mcmaster.com/. [Accessed: 14-Dec-2022].
[37] “Timing Belt Drive Selection Procedure.”

[38] Levi Gershon, 2022, *Permanent Magnets for Hull Attachment*.
[39] Budynas, R. G., and Nisbett, J. K., 2016, *Shigley's Mechanical Engineering Design*, McGraw Hill Education.
[40] "Attenuation and Skin Depth — Electromagnetic Geophysics" [Online]. Available: https://em.geosci.xyz/content/maxwell1_fundamentals/harmonic_planewaves_homogeneous/skindepth.html. [Accessed: 01-Nov-2022].
[41] "Fathom ROV Tether (ROV-Ready)," Blue Robotics.
[42] "Radio Direction Finding Techniques | Details | Hackaday.Io" [Online]. Available: https://hackaday.io/project/project/25995-bloodhound-autonomous-radiolocation-drone/log/63866-radio-direction-finding-techniques. [Accessed: 26-Oct-2022].
[43] Lauv, J., Macedo, M., Mellor, M., Poler, C., and Winter-Fox, T., 2017, "Hull Crawler."
[44] "Water Direction Sensor," Automation & Control Engineering Forum [Online]. Available: https://control.com/forums/threads/water-direction-sensor.16212/. [Accessed: 26-Oct-2022].
[45] 2000, "How Computer Mice Work," HowStuffWorks [Online]. Available: https://computer.howstuffworks.com/mouse.htm. [Accessed: 26-Oct-2022].
[46] "How Does a Mouse Know When You Move It? || How Does a Computer Mouse Work? - YouTube" [Online]. Available: https://www.youtube.com/watch?v=SAaESb4wTCM&ab_channel=BranchEducation. [Accessed: 26-Oct-2022].
[47] Corke, P., Detweiler, C., Dunbabin, M., Hamilton, M., Rus, D., and Vasilescu, I., 2007, "Experiments with Underwater Robot Localization and Tracking," *Proceedings 2007 IEEE International Conference on Robotics and Automation*, IEEE, Rome, Italy, pp. 4556–4561.
[48] Ferrera, M., Moras, J., Trouvé-Peloux, P., and Creuze, V., 2020, "Real-Time Monocular Visual Odometry for Turbid and Dynamic Underwater Environments."
[49] Tunawattana, N., Norman, R., and Roskilly, A. P., 2010, "Design of an Underwater Positioning Sensor for Crawling Ship Hull Maintenance Robots," Proceedings of the Institution of Mechanical Engineers, Part M: Journal of Engineering for the Maritime Environment, **224**(2), pp. 115–125.
[50] 2021, "Blueye X3 Technical Specifications."
[51] "Fig 3: Optimal Operating Temperature of Li-Ion Battery [26]," ResearchGate [Online]. Available: https://www.researchgate.net/figure/Optimal-operating-temperature-of-Li-ion-battery-26_fig3_327966044. [Accessed: 03-Nov-2022].
[52] "Power Supply on Different Types of Ships," ElectroTechnical Officer [Online]. Available: https://electrotechnical-officer.com/power-supply-on-different-types-of-ships/. [Accessed: 14-Dec-2022].

11. Appendices

11.1 Variable Names

A: Cross-sectional area (m^2)

C_d,f: Frontal area of the crawler (N/A)

C_f: Coefficient of fit (Nm^2)
C_rr: Coefficient of rolling resistance (N/A)
C_10: Nominal radial load rating of bearing 10 million cycles (N)
D_brush: Brush diameter
E_316: Young's Modulus of 316 stainless steel (Pa)
F_drag,crawler: Drag on the crawler due to the motion of the crawler (N)
F_drag,ship: Drag on the crawler due to the motion of the parent vessel (N)
F_fr: Total frictional force generated by the crawler (N)
F_mag: Total magnetic adhesion force (N)
F_N: Total normal force (N)
F_react: Reaction force on single bearing raceway (N)
FoS: Factor of Safety, globally set to 1.33 (N/A)
I: Second moment of area (m^4)
ID: Inner diameter, brush (m)
k: Array wavenumber (1/m)
L: Brush length (m)
L_bear: Bearing pressure point separation (m)
L_contact,f: desired contact length between brush and hull
L_contact,i: stationary contact length between brush and hull
M_0: Magnetization strength, (A/m)
MoS_i: Margin of Safety (N/A)
μ: Coefficient of friction (N/A)
μ_0: Permeability of free space (mkg/s^2A^2)
N: Number of wheels (N/A)
OD: Outer diameter, brush (m)
P_sin: Adhesion pressure of a single magnet (Pa)
P_hal: Adhesion pressure of a Halbach array (Pa)
r_0: Fit distance (m)
r_brush: brush radius
ρ: Seawater density (kg/m^3)
σ_ty: Yield stress (Pa)
τ: Brush torque (Nm)
Θ: Angle of inclination (deg)
v: Crawler velocity (m/s)
v_def: Beam deflection (m)
w: Distributed normal load, hull on brush (N/m)
x: Gap distance between magnet and hull (m)
y_con: Lateral offset between bearing center and tire contact patch (m)
y_ski: Lateral offset between bearing center and ski center (m)